TRAPPING, LASER COOLING, AND SPECTROSCOPY OF THORIUM IV

A Thesis
Presented to
The Academic Faculty

by

Corey J. Campbell

In Partial Fulfillment
of the Requirements for the Degree
Doctor of Philosophy in the
School of Physics

Georgia Institute of Technology
August 2011

TRAPPING, LASER COOLING, AND SPECTROSCOPY OF THORIUM IV

Approved by:

Alex Kuzmich, Advisor
School of Physics
Georgia Institute of Technology

Ken Brown
School of Chemistry and Biochemistry
Georgia Institute of Technology

T. A. Brian Kennedy
School of Physics
Georgia Institute of Technology

Phil First
School of Physics
Georgia Institute of Technology

Walt de Heer
School of Physics
Georgia Institute of Technology

Date Approved: 23 June 2011

To my family.

ACKNOWLEDGEMENTS

Nearly every day throughout the past six years of working in the Kuzmich Lab, I've been amazed at the environment in which I'm fortunate enough to work. I am surrounded by so many people of such high caliber and an abundance of state-of-the-art experimental atomic physics. For this opportunity, I thank my advisor, Alex Kuzmich. I also thank him for his patience, allowing me to grow into a competent physicist in this wonderful environment and advising me with clarity when it is often needed.

I would like to thank the extremely talented Thierry Chaneliere and Dzmitry Matsukevich for guiding me in my first year in the lab. They served as ideal examples for me to follow and were happy to show me the way. My introduction to espresso by Thierry and our regular laps in the pool provided a wonderful lab culture as well. In the early part of my graduate career, I also worked on neutral atom experiments with Shau-Yu Lan. He was an absolute pleasure to work with and his amazing work ethic was a challenge to match.

Ran Zhao and I came to Georgia Tech at the same time. We also were both quickly drawn to the Kuzmich Lab. Through the years, we studied, worked, learned, and matured into physicists together. In this course, her friendship and encouragement have been invaluable to me and I thank her very much for this.

Four years ago, I started on the ground floor of the thorium ion trapping project. Shortly after its initiation, Dave Naylor (a.k.a. Upgrade), came on board as an undergraduate freshman. He is a workhorse with an eye for success and ferociously learned tricks of the experimental trade. He is a great colleague and our semi-regular all-nighters in the lab discussing, designing, and building experiments and integrating data are among the most enjoyable times I spent as a graduate student.

During the early stages of the thorium project, I had the pleasure of working with Adam

Finally, I thank my family for all their love and support.

TABLE OF CONTENTS

CHAPTERS

LIST OF TABLES

LIST OF FIGURES

xiii

SUMMARY

This dissertation is a report of the work done by the author to trap, laser cool, and perform spectroscopy on the 229 and 232 isotopes of Thorium IV. The introductory chapter motivates the work on ^{229}Th^{3+}. Chapter 2 describes the theory of ion trapping and reviews the apparatus' used in this research to confine both isotopes. Chapter 3 reviews the theory of laser cooling weakly bound atoms and extends the description to the more complicated Th^{3+} system. Realization of laser cooling of both isotopes is discussed along with experimental details. Chapter 4 discusses laser spectroscopy of both isotopes. Chapter 5 investigates the capabilities of the isomer transition in the ^{229}Th nucleus as an optical clock. The unique features of such a transition are also discussed in terms of their applicability to the search for temporal variation of the fine structure constant.

CHAPTER I

INTRODUCTION

In 1976, Kroger and Reich discovered that the nucleus of ^{229}Th has an extremely low lying first excited state. Nuclear excited states are generally keV to MeV above the ground state, but this level was found to be less than 100 eV above the ground state [1]. In 1990, Reich and Helmer examined higher resolution nuclear data to determine that the nuclear energy splitting is -1 ± 4 eV [2]. This result provided promise that the extraordinarily small splitting would allow for laser excitation of a nuclear system for the first time along with application of precision spectroscopic techniques. In 1994, Helmer and Reich [3], using improved gamma-ray detector technology and calibration methods, determined that the energy splitting was 3.5 ± 1.0 eV.

With the relatively small 1 eV uncertainty, direct observation of the nuclear transition was attempted by various groups [4–7], though no conclusive results were obtained. Further advances in gamma-ray detector technology have allowed for even lower measurement uncertainty. The most recent determination of the nuclear transition energy, by Beck *et al.* in 2007, produced a value of 7.6(5) eV [8]. This result is more than 3 standard deviations away from the long-accepted 3.5 eV value and might explain the previously inconclusive isomer search results.

The low-lying isomer state has a predicted lifetime of $10^3 - 10^4$ s [9, 10]. Due to the relative smallness of nuclear electromagnetic moments and, hence, superb isolation of the nucleus from external electric and magnetic fields, the ^{229}Th nuclear isomer transition might be used as a next generation optical clock [11]. The unique characteristics that a nuclear transition would provide may also allow for extremely enhanced sensitivity to variation of fundamental constants [12]. Particularly, the fine-structure constant which characterized

the strength of electromagnetic coupling might be probed very sensitively for temporal variation due to the immense Coulomb energy of the large thorium nucleus.

To fully utilize the special character of the ^{229}Th nucleus, one would seek ultra-cold temperatures where the nucleus is well localized and isolated from collisions and external field variations. This might also be an ideal system for initial optical excitation of the isomer. The nuclear transition frequency is still only known to ± 240 THz, whereas the transition width is $\ll 1$ Hz. A tightly focused excitation laser beam might provide sufficiently high optical intensity to search the large spectral range for the narrow isomer transition in a reasonable time. This would require a well-localized nucleus.
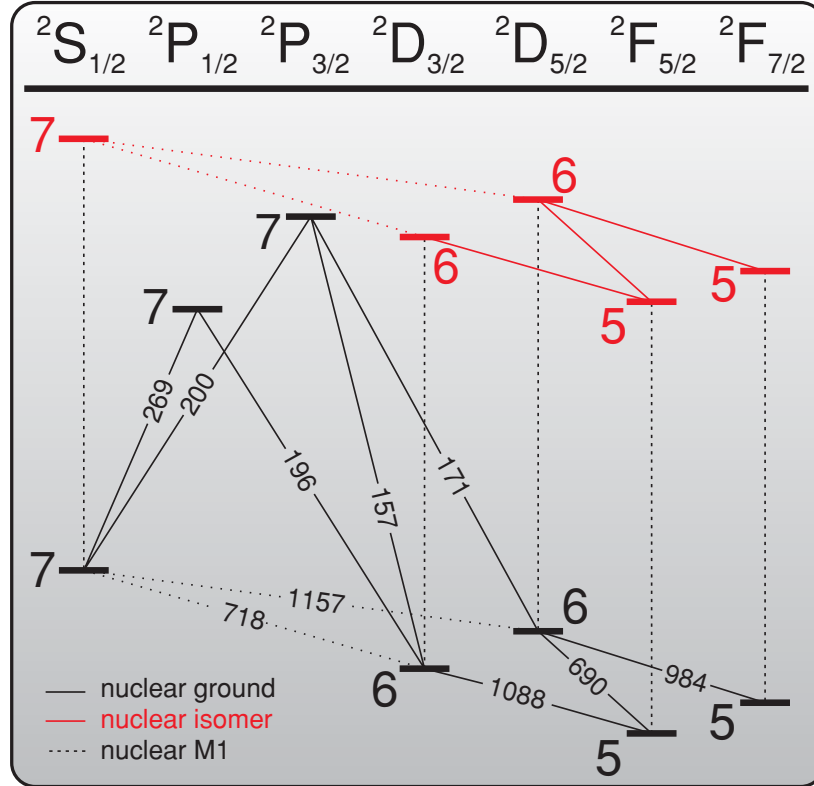
Figure 1: A diagram of electronic energy levels and electric dipole transitions including both nuclear ground and excited isomeric manifolds. Optical transition wavelengths are in nm and the integers near atomic levels indicate principle quantum numbers.

A convenient method for localizing the nucleus would be to laser cool the atom using electronic transitions. Neutral thorium contains four valence electrons, a system too

complex to easily laser cool. The multitude of metastable electronic levels would require a prohibitively large number of lasers. Triply charged thorium, however, has only one valence electron. A monovalent atom is the most convenient system to laser cool due to the simple electronic structure. Laser cooling of many monovalent alkali atoms and alkaline-earth ions has been previously demonstrated. The structure of Th^{3+} is amenable to laser cooling with multiple electric dipole transition wavelengths in the range of available diode lasers [11]. Figure 1 displays the electronic structure of both the nuclear ground and isomer manifolds with electric dipole transitions. The lowest lying transitions at 1088nm, 690 nm, and 984 nm are convenient for laser cooling and ion imaging. In addition to the ability to directly laser cool $^{229}Th^{3+}$, the field of ion trapping is mature, providing straight-forward techniques for confining $^{229}Th^{3+}$ ions.

Though confinement and laser cooling of $^{229}Th^{3+}$ are not fundamentally prohibited, neither experimental task has been realized prior to this work. Due to the extremely high cost of ^{229}Th, the 232 isotope is used here to initially develop the required technologies for effective spectroscopy of the ^{229}Th nucleus, i.e. triple ionization, confinement, long storage times, laser cooling, and ion imaging. Additionally, the lack of nuclear spin in ^{232}Th substantially reduces the complexity of initial laser cooling and spectroscopy. After the necessary experimental techniques are sufficiently mature, $^{229}Th^{3+}$ ions are laser cooled and high precision laser spectroscopy is performed. This result paves the way toward optical excitation of the nuclear isomer.

Particular aspects of the $^{229}Th^{3+}$ system are also examined in order to estimate its effectiveness and utility as a next-generation optical clock and ultra-sensitive probe of temporal variation of fundamental constants.

CHAPTER II

THORIUM IV ION TRAPPING

2.1 Radio-Frequency Trapping Theory

Earnshaw's Theorem states that a charged particle cannot be held in stable equilibrium by electrostatic forces alone [13]. This can be seen by inspection of Laplace's Equation, $\nabla^2 \psi = 0$, where ψ is the electrostatic potential in vacuum. A requirement for stable confinement along a given spatial dimension is that the second derivative of the potential be positive. As can be seen, a stable potential cannot be achieved in all three spatial dimensions at once.

Time-varying potentials may, however, be used to generate ponderomotive forces, enabling one to confine charged particles in all three dimensions. The treatment here of such dynamics is a simplified version of that of Dehmelt [14, 15].

Consider a particle of mass m and charge Q placed in an electric field E_0 which varies sinusoidally in amplitude at frequency Ω. The force on the particle from this field is

$$F(t) = m\ddot{x} = QE_0 \cos \Omega t. \tag{1}$$

For the particle initially at rest at $x = 0$, its velocity $\dot{x}(t)$ and position $x(t)$ are

$$\dot{x}(t) = \frac{QE_0}{m\Omega} \sin \Omega t \tag{2}$$

$$x(t) = -\frac{QE_0}{m\Omega^2} \cos \Omega t + x_0. \tag{3}$$

In this system, the particle oscillates with amplitude $\Delta x = (QE_0)/(m\Omega^2)$ about the position $x_{av} = 0$, but has no net acceleration when averaged over an rf cycle.

For a spatially varying electric field profile, Equation (1) becomes

$$F(x, t) = QE_0(x) \cos \Omega t \tag{4}$$

For sufficiently fast electric field oscillations such that $\Delta x \ll E_0(x_{av}) / [dE_0(x_{av})/dx]$, the *pseudopotential approximation* may be made by expanding the electric field profile to first order about x_{av}. This leads to

$$F(x, t) = QE_0(x_{av}) \cos \Omega t + Q \frac{dE_0(x_{av})}{dx}(x - x_{av}) \cos \Omega t \tag{5}$$

Substituting Equation (3) for $(x - x_{av})$, Equation (5) becomes

$$F(x, t) = QE_0(x_{av}) \cos \Omega t - \frac{Q^2 E_0(x_{av})}{m\Omega^2} \frac{dE_0(x_{av})}{dx} \cos^2 \Omega t \tag{6}$$

and when averaged over one rf cycle, becomes

$$F_{av}(x_{av}) = -\frac{Q^2 E_0(x_{av})}{2m\Omega^2} \frac{dE_0(x_{av})}{dx}. \tag{7}$$

After extending this treatment directly to three dimensions, one may define the *ponderomotive pseudopotential*, $\Psi(x, y, z)$, such that

$$F(\overline{x}, \overline{y}, \overline{z}) = -Q \nabla \Psi(\overline{x}, \overline{y}, \overline{z}) \tag{8}$$

which leads to the result

$$\Psi(\overline{x}, \overline{y}, \overline{z}) = \frac{Q E_0^2(\overline{x}, \overline{y}, \overline{z})}{4m\Omega^2}. \tag{9}$$

Here, the bars over the spatial coordinates denote their average values over one rf cycle of the electric field amplitude.

A convenient and easily understood potential for particle confinement is the harmonic potential. A ponderomotive pseudopotential of this form may be made in two dimensions with an oscillating two-dimensional electric quadrupole potential, $\psi_{rf} \propto (x^2 - y^2) \cos \Omega t$.

Figure 2 shows cross-sections and polarities of the trap rf electrodes (trap rods) used in this work which generate approximate two-dimensional quadrupole potentials near the pseudopotential minimum. The dashed hyperbolic lines represent ideal quadrupole equipotentials and imply ideal electrode surface shapes. By applying a voltage

$$V_\pm = \pm [V_0 \cos \Omega t + U_0] \tag{10}$$

to the corresponding realistic trap rods, the electric potential near the center of the trap may be approximated by

$$\psi_r(x, y, t) \approx \kappa_r \left[V_0 \cos \Omega t + U_0\right] \left(\frac{x^2 - y^2}{r_0^2}\right) \tag{11}$$

where κ_r is a scaling factor introduced to account for the departure from infinite hyperbolic shapes of the trap rods.
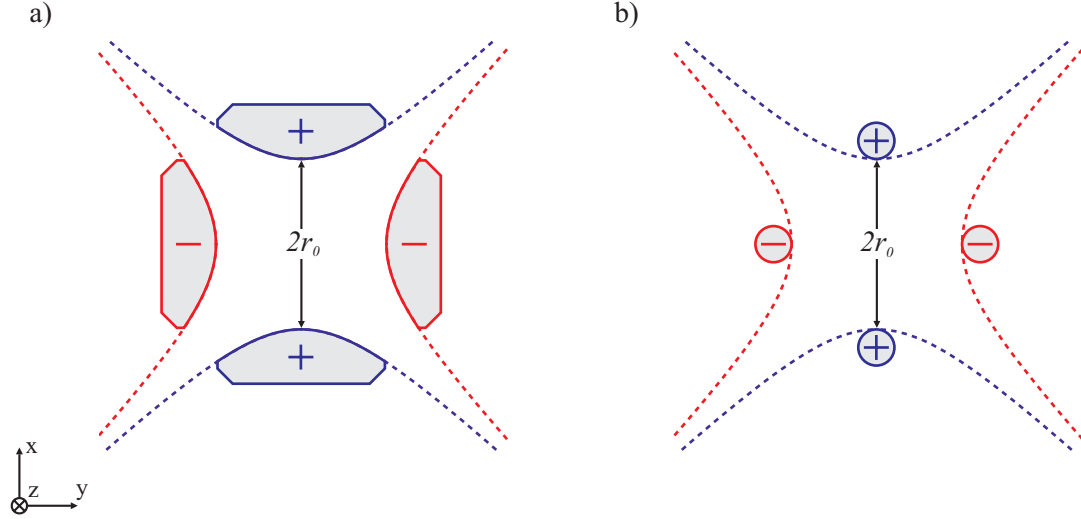
Figure 2: Rod electrode geometries. a) A cross section of truncated hyperbolic trap rods illustrates that the electrode surfaces lie along quadrupolar equipotentials. This surface shape creates a high-quality quadrupole potential from the pseudopotential minimum out to the electrode surfaces. b) The circular rod shape surface deviates significantly from ideal quadrupole equipotentials, introducing higher-order even multipole terms to the potential. This is detrimental when performing mass spectrometry, though is advantageous for laser cooling. The enhanced optical access is important for efficient fluorescence detection.

The truncated hyperbolic electrode shape in Figure 2 has the advantage that it approximates the quadrupole potential very well from the pseudopotential minimum out to the electrode surface, whereas for the circular cylinder rod shape, higher-order fields become significant and complicate ion dynamics at large ion excursions. For trapping and laser cooling, however, this is of little consequence while optical access transverse to the pseudopotential axis (trap axis) can be greatly enhanced over that of the truncated hyperbolic rod shape.

To confine positively charged ions along the trap axis, positively biased endcap electrodes (endcaps) with convenient symmetry about the trap axis may be used. For an endcap separation $2z_0$ along the trap axis and bias voltage U_{ec}, the potential near the trap center may be approximated by

$$\psi_{ec}(x, y, z) \approx \kappa_z U_{ec} \left(\frac{z^2 - \frac{1}{2}(x^2 + y^2)}{z_0^2} \right) \tag{12}$$

Here, κ_z is a scaling factor introduced to account for the endcap geometry. Combining ψ_r and ψ_{ec}, one obtains for the total ion potential near the trap minimum,

$$
\begin{aligned}
\psi(x, y, z, t) &\approx \psi_r + \psi_{ec} \\
&\approx \left(\frac{\kappa_r V_0}{r_0^2} \cos \Omega t + \frac{\kappa_r U_0}{r_0^2} - \frac{1}{2} \frac{\kappa_z U_{ec}}{z_0^2} \right) x^2 \\
&\quad + \left(-\frac{\kappa_r V_0}{r_0^2} \cos \Omega t - \frac{\kappa_r U_0}{r_0^2} - \frac{1}{2} \frac{\kappa_z U_{ec}}{z_0^2} \right) y^2 \\
&\quad + \left(\frac{\kappa_z U_{ec}}{z_0^2} \right) z^2
\end{aligned} \tag{13}
$$

which corresponds to an electric field

$$
\begin{aligned}
\mathbf{E}(\mathbf{x}, \mathbf{y}, \mathbf{z}, t) &= -2 \left(\frac{\kappa_r V_0}{r_0^2} \cos \Omega t + \frac{\kappa_r U_0}{r_0^2} - \frac{1}{2} \frac{\kappa_z U_{ec}}{z_0^2} \right) x \hat{x} \\
&\quad + 2 \left(\frac{\kappa_r V_0}{r_0^2} \cos \Omega t + \frac{\kappa_r U_0}{r_0^2} + \frac{1}{2} \frac{\kappa_z U_{ec}}{z_0^2} \right) y \hat{y} \\
&\quad - 2 \left(\frac{\kappa_z U_{ec}}{z_0^2} \right) z \hat{z}
\end{aligned} \tag{14}
$$

This general combination of rf and dc electric fields is used in this work to confine atomic ions and is known as the linear rf trap or linear Paul trap, after Wolfgang Paul, inventor of the three-dimensional quadrupole trap [16].

Because the electric field gradient is constant in all three spatial dimensions, a trapped ion trajectory obeys the Mathieu equations

$$\ddot{u}_i + [a_i + 2q_i \cos \Omega t] \frac{\Omega^2}{4} u_i = 0 \tag{15}$$

where $\mathbf{u} = u_x \hat{x} + u_y \hat{y} + u_z \hat{z}$ is the ion coordinate in the basis of Figure 2,

$$q_x = -q_y = q = \frac{4 Q \kappa_r V_0}{m r_0^2 \Omega^2}, \quad q_z = 0, \tag{16}$$

and

$$a_x = -\Delta a + a = -\frac{4Q\kappa_z U_{ec}}{mz_0^2\Omega^2} + \frac{8Q\kappa_r U_0}{mr_0^2\Omega^2} \tag{17}$$

$$a_y = -\Delta a - a = -\frac{4Q\kappa_z U_{ec}}{mz_0^2\Omega^2} - \frac{8Q\kappa_r U_0}{mr_0^2\Omega^2} \tag{18}$$

$$a_z = 2\Delta a = \frac{8Q\kappa_z U_{ec}}{mz_0^2\Omega^2}. \tag{19}$$

In this system, ion motion and stability can be solved within and well outside of the pseudopotential approximation. Specifically, the fundamental ion secular frequencies are

$$\omega_i = \frac{\beta_i}{2}\Omega \tag{20}$$

where β_i is defined by the continued fraction [18]

$$\beta_i^2 = a_i + \cfrac{q_i^2}{(\beta_i + 2)^2 - a_i - \cfrac{q_i^2}{(\beta_i + 4)^2 - a_i - \cfrac{q_i^2}{(\beta_i + 6)^2 - a_i - \cdots}}} \\ + \cfrac{q_i^2}{(\beta_i - 2)^2 - a_i - \cfrac{q_i^2}{(\beta_i - 4)^2 - a_i - \cfrac{q_i^2}{(\beta_i - 6)^2 - a_i - \cdots}}} \tag{21}$$

In the operating regime of the traps in this work and in almost all linear rf traps, stable ion trajectories occur when $0 < \beta_{x,y} < 1$ and $\beta_z > 0$. For $a_{x,y} = 0$, this corresponds to a maximum q of 0.908, also known as the low-mass cutoff. For particles with mass-to-charge ratio (m/Q) less than that corresponding to $q = 0.908$ have a larger q and are unstable. Figure 3 shows simulated radial motion of a ^{229}Th^{3+} ion in the extended trap of Section 2.4 for various q values ($\Omega = 2\pi\times6.0$ MHz) and negligibly small $a_{x,y}$ values. The driven oscillatory motion of the ion at Ω (drive frequency) is referred to as micromotion and the lower frequency ion oscillation is secular motion due to the particle's non-zero temperature within the ponderomotive potential. Micromotion serves as the primary heating mechanism of ions which are not at the rf potential minimum and should be minimized for efficient ion cooling. As can be seen in Figure 3, low q is preferable for this.
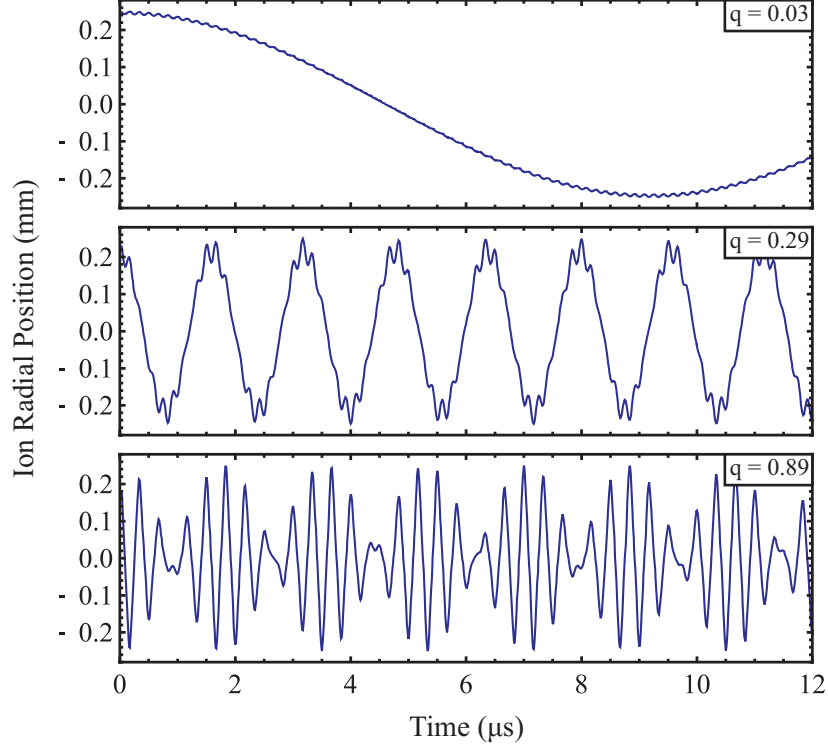
Figure 3: Simulation of radial motion of a single trapped ion in the extended trap using Simion 8.0. At extremely low q, the pseudopotential approximation is clearly justified, as ion micromotion is much more rapid and less significant than the larger secular motion. As V_0 is increased, the trap frequency increases as does the micromotion amplitude. Near the low-mass cutoff, secular oscillations are nearly half as fast as micromotion, leading to a nearly undefined rf potential.

In the regime where $|q_i|, |a_i| \ll 1$, ion motion may be approximated by

$$u_i(t) \approx u_{1i} \cos\left(\omega_i t + \phi_i\right) \left[1 + \frac{q_i}{2} \cos \Omega t\right] \tag{22}$$

and the secular frequencies by

$$\omega_i \cong \tfrac{1}{2}\Omega \sqrt{a_i + \tfrac{1}{2}q_i^2}. \tag{23}$$

From Equations (22) and (23), it is evident that as q is decreased to minimize micromotion heating, Ω must be increased to maintain a given secular frequency. A technical limitation here is the maximum achievable rf voltage amplitude, which in this work is $V_{0(max)} \sim 1500$ V.

Equation (22) may be used to calculated the average kinetic energy of an ion as [17]

$$E_{Ki} = \tfrac{1}{2}m\langle \dot{u}_i^2\rangle \cong \tfrac{1}{4}mu_{1i}^2\left(\omega_i^2 + \tfrac{1}{8}q_i^2\Omega^2\right). \tag{24}$$

From Equations (24) and (23), it can be seen that, due to micromotion, the total kinetic energy is about twice that of the thermal energy along the dimensions of rf trapping. There is no such micromotion contribution in the dimension of static field confinement.

In addition to unavoidable micromotion, an ambient electric field $\vec{E}_{dc}$ may shift the trap potential minimum away from the rf potential minimum. The shift of the ion's average position may be expressed as [17]

$$u_{0i} \cong \frac{4Q\left(\vec{E}_{dc} \cdot \hat{u}_i\right)}{m\left(a_i + \frac{1}{2}q_i^2\right)\Omega^2} \tag{25}$$

This shift from the rf potential minimum creates excess micromotion, resulting in a total kinetic energy along the ith axis of

$$E_{Ki} \cong \frac{1}{4}mu_{1i}^2\left(\omega_i^2 + \frac{1}{8}q_i^2\Omega^2\right) + \frac{4}{m}\left[\frac{Qq_i\left(\vec{E}_{dc} \cdot \hat{u}_i\right)}{\left(2a_i + q_i^2\right)\Omega}\right]^2. \tag{26}$$

For a given ambient field, higher trap drive frequencies reduce the excess micromotion energy. Minimization of this term is important in ion trapping experiments and is done here by compensating ambient electric fields and using relatively high drive frequencies to suppress the heating effect from imperfect field cancellation.

It should be noted that linear rf traps using the rf voltage polarities discussed in this section are said to be running in the balanced mode, as opposed to the unbalanced mode in which rf is applied to only one pair of opposing trap rods while the other pair is held at ground. By removing the rf voltage from one pair of trap rods and keeping V_0 constant, the stability parameter q is simply halved. Both modes of operation offer distinct advantages and are used in this work.

2.2   Triple Ionization and Trapping of Thorium

Because the transition of ultimate interest in ^{229}Th is the 7.6(5) eV nuclear isomer transition, one may select to work with any convenient charge state of the atomic system. Monovalent atomic systems such as neutral alkalies and singly charged alkaline earths have been

shown to be convenient systems for laser cooling and high precision laser spectroscopy due to the relatively simple electronic structure. The number of optical frequencies required for such experiments is at a minimum. From this point of view, monovalent thorium, i.e. Th^{3+}, is an appealing choice. The lower charge states of thorium contain complex electronic structure and, therefore, multiple optical fields would be required to avoid leaving low-lying metastable electronic states dark. Another appealing and possibly critical characteristic of Th^{3+} is its ionization potential, 28.8 eV, which is well above the isomeric energy. This large energy difference suppresses the likelihood of internal conversion during isomer excitation and decay. Th^{3+}, therefore, seems to be the optimal candidate for high precision spectroscopy of the nuclear isomer transition. The advantages stated above are countered by the initial difficulty in producing and trapping significant amounts of ions in this charge state for spectroscopy as well as the relatively short lifetime of a trapped ion with such high electron affinity.

Laser ablation of a thorium sample is chosen as the method for triple ionization because traditional single ionization methods such as electron bombardment ionization and photo-ionization within an atomic beam are not viable. An appreciable vapor pressure of neutral thorium for such an atomic beam is found to require temperatures which are higher than the melting points of even the most resilient oven materials, i.g. W and Ta. Additionally, electron bombardment ionization becomes substantially less efficient with higher charge states [19] and photo-ionization requires a prohibitively large number of photo-excitations to reach Th^{3+} (38.2 eV).

The light source for ablation is a 5 ns long pulse at the third harmonic (355 nm) of a YAG laser with pulse energy 20-500 μJ. The pulse is focused to a 20(10) μm spot size on a thorium source. Two different types of planar thorium ablation targets are used in this work, a pure thorium metal source and a high-purity aluminum substrate containing a thin film of thorium nitrate salt on its surface. The thorium metal target is made of the 232 isotope and is used for all initial Th^{3+} ionization, trapping, and laser spectroscopy work,

as well as preliminary ion trap testing and laser alignment prior to $^{229}Th^{3+}$ work. The nitrate targets are motivated by the non-metallic form of the ^{229}Th source. Because the 229 isotope is radioactive (7880 yr half-life) and does not occur in nature, it is very rare and expensive (~ \$120,000/mg). This is in contrast to the 232 isotope (1.4×10^{10} yr half-life) which does occur in nature and is relatively inexpensive (~ \$30/g). Consequently, the only available source of ^{229}Th at the time of purchase was in the form of a nitrate salt, $Th(NO_3)_4$ (76% ^{229}Th, 24% ^{232}Th). In order to prepare the ^{229}Th for ablation, the salt is dissolved into a nitric acid solution [20] and 20 μg of ^{229}Th (40 μL of solution) are deposited onto a 2 mm×2 mm area of a 99.99 % pure aluminum substrate (Alfa Aesar 40761). Aluminum is chosen due to its small m/Q's (27 amu/e, 13.5 amu/e, 9 amu/e, etc.) which are substantially different from triply charged thorium ($\approx$77 amu/e) and can easily be made unstable during trap loading. Here, e is the electron charge. Because triple ionization efficiency in ablation is much lower than that of single and double ionization, the high purity of the aluminum substrate is important, keeping the absolute yield of Th^{3+} in the plume higher than that of any singly or doubly ionized contaminating component of similar m/Q. For instance, aluminum 6061 contains a few percent impurities by mass, some of which have m/Q's similar to that of Th^{3+}. These impurities are thought to be the reason for failure to observe trapped Th^{3+} from nitrate targets with such substrates. An overwhelming abundance of the pollutants within the plume preclude efficient loading of the ion of interest.

Before the ^{229}Th nitrate target was employed, a nearly identical ^{232}Th nitrate target was made and tested using the same ionization and trap loading protocols used for the thorium metal target. The only difference between the two nitrate targets is the solvent used for thorium deposition. While nitric acid was used for the 229 isotope to prevent adsorption of the radionuclide molecules to the walls of the solution container [20], distilled water was used for the 232 isotope.

Characterization of the ablation plume dynamics and confirmation of Th^{3+} creation are done via laser spectroscopy in plumes from the thorium metal sample. By passing a laser

beam through the ablation plume at a known distance from the thorium sample and monitoring its transmission on a photodetector, one can confirm creation of a particular charge state and observe its velocity distribution. For these experiments, probe beam waists of 200-300 μm and optical powers of 100-500 μW are used and the ablation plume is directed not toward trap electrodes, but into empty vacuum. Electronic transitions are observed in Th+ and Th^{3+}, giving some insight into the thorium dynamics during ablation. Figure 4 a) illustrates the "Coulomb explosion" dynamic where higher charge states are accelerated more rapidly in the initial electric fields caused by the ejected electrons [21]. Figure 4 b) shows simultaneous absorption of 690 nm and 984 nm light within Th^{3+}. The 690 nm probe field is positioned ~2 mm from the thorium sample while the 984 nm probe is less than two beam diameters further away. This data shows that the Th^{3+} component of the ablation plume has an average velocity of ~10 km/s, suggesting that particular care might be required in trapping these energetic particles in large quantities. With the ratio of probe beam diameter to distance from the sample being $\approx$0.4 and the measured ratio of temporal probe absorption width to delay after the ablation pulse being $\approx$0.3 (Figure 4), one may estimate, assuming linear expansion of the plume, that the ratio of ablated Th^{3+} velocity width to average velocity is 0.4 - 0.3 = 0.1. This narrow velocity distribution may be exploited with trap potential gating to enhance trapping efficiency of Th^{3+} as well as to electrically block some unwanted components of the plume from entering and polluting the trap.

In addition to gaining velocity information regarding Th^{3+} and other ablation components, laser spectroscopy of the plume also serves to confirm spectral location of low-lying electronic transitions in Th^{3+}. By measuring the absorption ratio of 984 nm light to 690 nm light while scanning the frequency of the 984 nm probe fields, a clear spectroscopic signal can be seen (Figure 5). The large Stark and Doppler broadening and shifts, however, preclude the possibility of high-resolution signals. The ratios of absorption signals is taken over absolute absorption depth due to significant fluctuations in ablation plume density from YAG shot to shot. This leads to significant fluctuations in absolute probe absorption.

a) — 984 nm Transmission (Th IV)   250 ns/div
— 688 nm Transmission (Th II)
— Ablation Pulse

b) — 690 nm Transmission (Th IV)   100 ns/div
— 984 nm Transmission (Th IV)
— Ablation Pulse
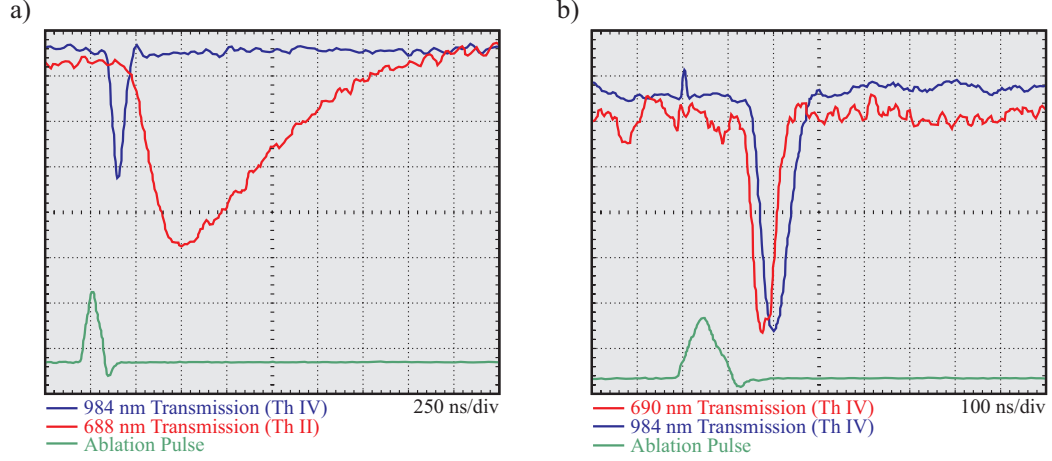
Figure 4: Probe laser absorption through an ablation plume. a) Light at 984 nm is resonant with an electric dipole transition in Th^{3+} and passes through an ablation plume where it is partially absorbed. Similarly, light at 688 nm is resonant with an electric dipole transition in Th^+ and passes though the same ablation plume where it is absorbed. The Coulomb explosion nature of ablation plumes is observed. Here, the smaller m/Q particles are accelerated more rapidly from the ablation target. b) Two probe fields resonant with transitions in Th^{3+} pass through the ablation plume where they are partially absorbed. The plume dynamics for Th^{3+} are measured from the traces in order to enhance ion loading of the energetic particles.

$v_0 = 304619.3$ GHz
FWHM = 18 GHz
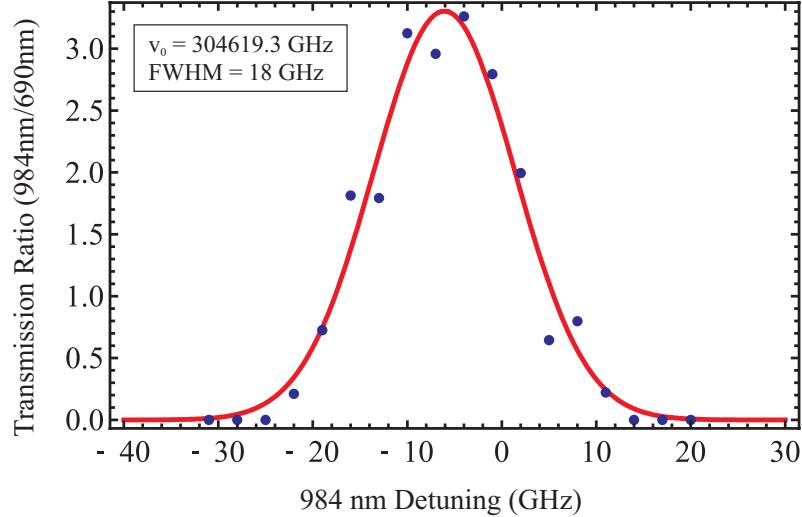
Figure 5: Ratio of 984 nm plume transmission signal to 690 nm transmission signal. By scanning the detuning of the 984 nm frequency, a broad feature is observed, indicating roughly the frequency on the transition. These types of scans serve as confirmation that no drastic errors exist in the spectroscopic data of [22]. Large Stark and Doppler broadening and shifts preclude high resolution spectroscopy. The laser detuning is with respect to the value given in [22].

Due to the high kinetic energy and charge density of ablated Th^{3+}, axial injection of the ions into a linear rf trap is the natural choice for trap loading. For this purpose, as well as axial optical access, the linear rf traps in this work all have clear apertures at both ends of the rf potential. To load ions into a given trap, a thorium sample is placed ~10 mm from a trap endcap and oriented such that a vector normal to the sample surface is directed along the trap axis. With arrival of a YAG ablation pulse onto the sample surface, a plume is ejected and propagates axially through an endcap aperture while $U_{ec} \approx 0$ V. After the Th^{3+} component of the ablation plume has entered the trap, U_{ec} is ramped to an operating voltage between 20-300 V with a 10% - 90% voltage risetime of < 600 ns (see Section 2.6). This dynamic loading aids in trapping efficiency of Th^{3+} while blocking much of the slower moving Th^{2+} and Th^+ from entering the trap volume. A demonstration of ion gating is shown in Figure 6 using fluorescence detection of $^{232}Th^{3+}$ in the extended trap of Section 2.4. Each data point is an average of three loading trials. The data is fit to an error function and gives a 10% - 90% risetime of 0.63 μs, which corresponds closely to the risetime of the endcap switching circuit. The thorium ablation target sits ~10 mm from the endcap entrance and the observed delay time of 9.3 μs is consistent with an ion velocity of ~10 km/s.

To further enhance ion loading when required, and to cool the trapped ions to about room temperature, helium buffer gas is introduced into the vacuum chamber (see Section 2.5) within a pressure range $10^{-7} - 10^{-3}$ Torr. The particular pressure used depends on the experiment. Though statistics are lacking, endcap gating of Th^+ and Th^{2+} during ion loading in a helium environment is observed to be particularly useful, enhancing the average number of Th^{3+} ions trapped by a factor of 2 to 5 over loading with long gate times.

Because the ions entering the trap rely on ponderomotive forces to confine them, efficient loading dictates that one period of the trap drive oscillation should be faster than the time required for an ion to traverse a characteristic distance of the trapping potential while at the loading velocity. For a trap radius of $r_0 \approx 3$ mm and a loading velocity of ~ 10 km/s,
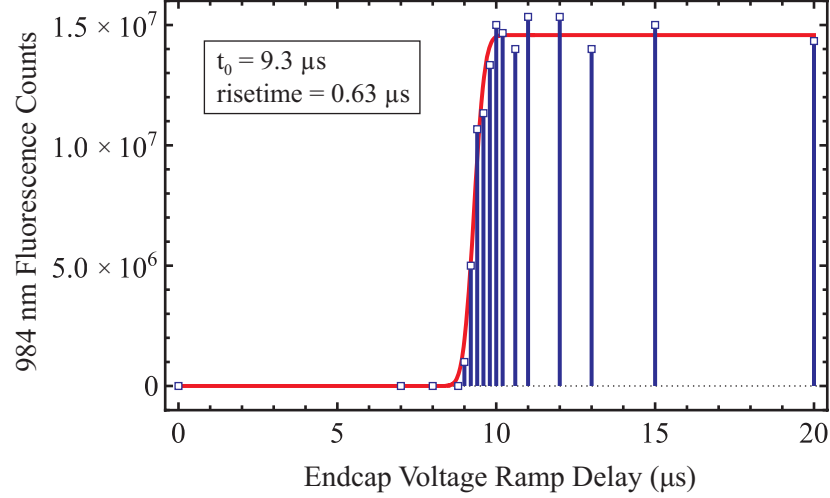
Figure 6: Demonstration of endcap gating. The endcap voltage of the extended trap is ramped from ground to 250 V in < 600 ns with varying ramp trigger delays after ion ablation. As the delay τ_{EC} is varied, the efficiency of transmission of $^{232}Th^{3+}$ through the endcap is varied. Each data point is an average of three trials where 984 nm fluorescence counts are recorded for each load. Saturation of the signal for $\tau_{EC} > 10\,\mu s$ suggests that the trap is saturated with $^{232}Th^{3+}$ ions.

an estimate for the minimum drive frequency required to achieve efficient loading is ~2 MHz. Observations in this work are consistent with this approximation. For example, with drive frequencies below 2 MHz applied to the extended trap of Section 2.4, loading of large Th^{3+} samples ($\gtrsim$ 10,000 ions) is achieved with $\lesssim$ 5% success per loading sequence and requires high buffer gas pressure. As the trap drive frequency is increased above 4 MHz, large sample loading becomes consistent ($\sim$ 80 %/trial), and at 8.5 MHz, large sample loading efficiency is $\gtrsim$ 95 %/trial, even without the aid of buffer gas.

2.3 *Thorium Mass Spectrometry*

For initial demonstration of Th^{3+} confinement, mass spectrometry techniques are used, as opposed to fluorescence detection methods. The mass spectrometry method requires a trapping potential which closely approximates the quadrupole potential throughout the trap volume, but has the advantage that trapped ion detection may be achieved in under 100 ms and without any knowledge of the ion's electronic structure. This circumvents the problem of initially insufficient knowledge of electric dipole transition frequencies for fluorescence

detection as well as the possibly short ion lifetime in the initial trapping environment. A system similar to that of [23] was designed and constructed for this purpose. The basic principle of operation is straight-forward. By adding an ac excitation signal $V_{ex} \cos(\omega_{ex} t)$ to one of the trap rods, trapped ions with radial secular frequency ω_{ex} (ω_{ex} depends on the ion's m/Q) are resonantly excited and ejected radially from the trap. These ions are then detected on a channel electron multiplier (CEM) as individual electrical pulses. To obtain a m/Q spectrum of trapped ions, the rf amplitude V_0 is ramped, sweeping the radial secular frequencies of ions within a given m/Q range through ω_{ex}. As the radial secular frequency of the trapped ions is swept through the value ω_{ex}, the ions are ejected and the CEM counts are correlated with a specific value of V_0, and in turn, a specific m/Q. The frequency chosen for ion ejection corresponds to a q near the low-mass cutoff, implying that V_0 is increased to generate mass scans. This mode of operation generates the highest m/Q scan resolution because the fractional density of m/Q is lowest in this region of stability. The ions are also becoming less stable rather than more stable as their q values are increasing toward the low-mass cutoff. This makes selective ejection of ions from the remaining trapped population more natural. The stability parameter a is set to zero for these experiments.

Because a high quality quadrupole potential is required for this method, the truncated hyperbolic trap rod shape is used. Images of the segmented hyperbolic trap used for mass spectrometry are shown in Figure 7. The trap material is SS304 and the electrical insulators are teflon. The trap radius is 4 mm and the segment lengths are 12 mm, 37 mm, and 12 mm, while the inner hyperbolic surface extends to $3r_0$ (12 mm) from the trap axis. In addition to the radial trapping voltages, a common dc voltage of 5-50 V is applied to all eight end segments, confining the ions to the central region of the trap where rf and ac excitation fringing fields along the trap axis are minimal. The central segment of one of the trap rods has a 0.3 mm×23 mm slit machined along one of the symmetry planes for ion ejection from the trap. A CEM (Photonis MAGNUM Electron Multiplier®) is biased at $\approx$ -2000 V and is placed just outside the ejection slit for ion detection. Circular cylinder electrodes with

17

apertures aligned coaxially with the trap are used as endcaps for dynamic loading.
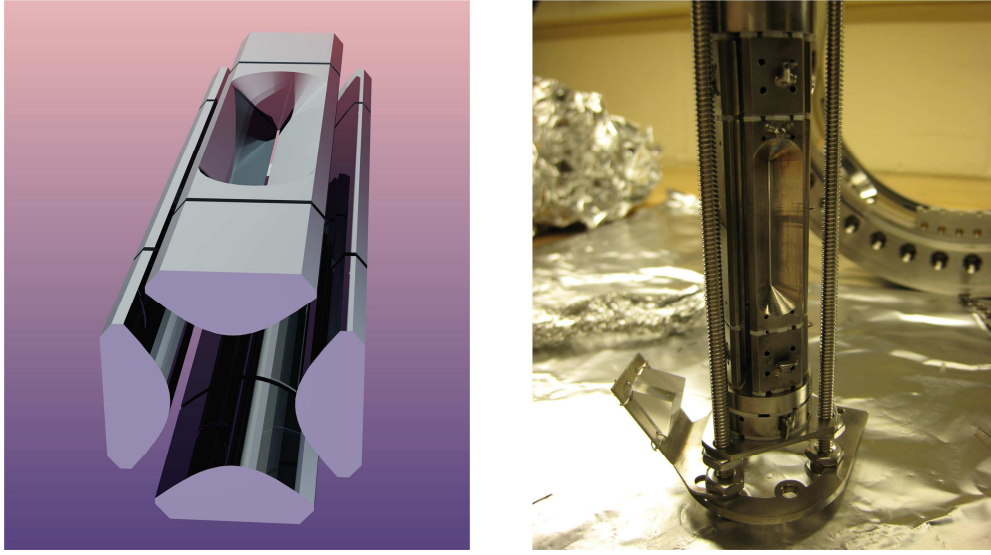
Figure 7: A conceptual drawing of the hyperbolic ion trap used for ion trapping and resonant ejection simulations in Simion 8.0 and a photo of the trap during construction.

The trap is run in the unbalanced mode with the ground trap rods defining the direction of secular excitation and ejection. A trap drive frequency of 1.4 MHz is used and corresponds to $\omega_{ex} \approx$ 550-690 kHz. The low drive frequency is required in order to reach the low-mass cutoff for ^{232}Th$^+$ (232 amu/e) with a maximum rf voltage of $V_0 \approx$ 1500 V. The excitation voltage ($V_{ex} \approx$ 0.1-5 V) is placed on the three segments of the ground trap rod opposite that of the ejection slit. This particular rf and ac configuration is chosen to reduce noise at the drive frequency on the CEM signal. To cool and localize ions to the center of the trap for efficient ion ejection, $\approx$1 mTorr of purified helium buffer gas is used. A typical scan is produced by linearly ramping V_0 across the range of interest in 100 ms - 2 s.

Figure 8 shows one of the first scans observing trapped thorium. The broadening and mass shift are likely due to space-charge effects from a large trapped sample, trapping field defects from the ejection slit, and trap misalignment. These non-ideal characteristics of the signal are, however, of little consequence. Peak identification is unambiguous.

With optimization of mass scan speed and excitation frequency and amplitude, higher resolution and higher signal-to-noise scans are achieved, as shown in Figure 9. ^{232}Th^{2+} and
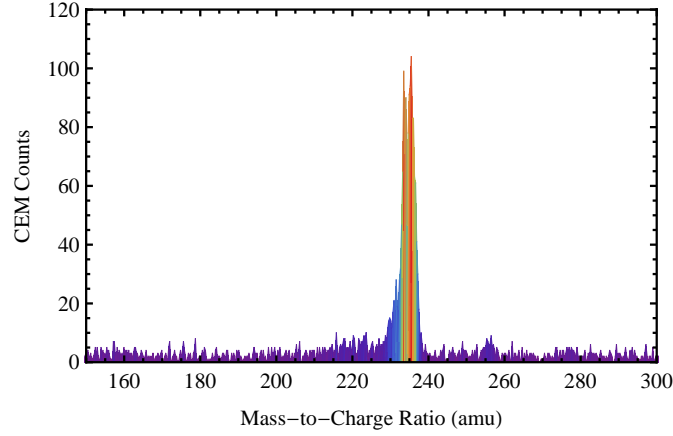
Figure 8: Mass spectrometry scan of ^{232}Th$^+$ at $m/Q \sim 232$ amu/e. The peak shift and broadening are likely due to space-charge effects from a large trapped sample, trapping field defects from the ejection slit, and trap misalignment.

^{232}ThO^{2+} peaks are clearly visible after a several second delay between trap loading and mass readout. This allows for oxidation to occur, likely from helium buffer gas impurities. Smaller peaks corresponding to mass shifts of +14 amu/e and +18 amu/e are also visible.
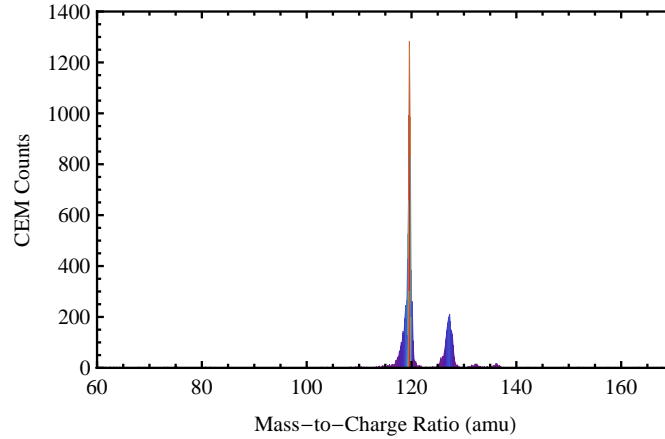
Figure 9: Mass spectrometry scan of ^{232}Th^{2+} and ^{232}ThO^{2+}.

With optimization of the ablation laser power and spot size on the thorium sample, Th^{3+} is generated in sufficient quantities, but can be detected clearly with a mass scan only after the much larger quantities of Th^{2+} and Th$^+$ are removed from the trap. This is done in the trap loading phase with endcap gating and relying on the fact that for stable loading of Th^{3+}, Th$^+$ can have a vitally low q value, making its loading much less efficient. For trapped
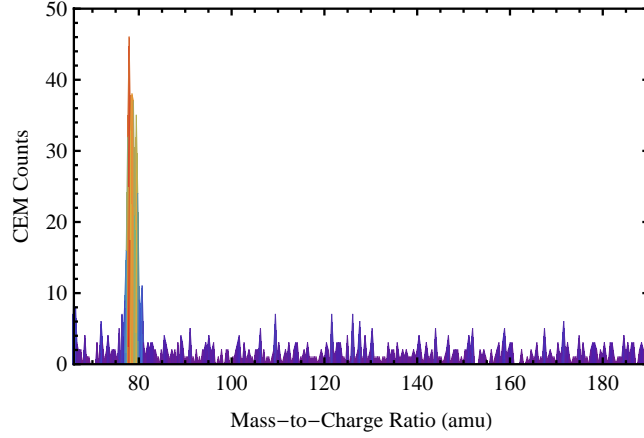
Figure 10: Mass spectrometry scan of ^{232}Th^{3+}.

pollutants, resonant ejection and ion destabilization are employed before the mass scan is executed. Figure 10 shows a representative scan detecting trapped ^{232}Th^{3+}. These scans suggested an initial trap lifetime of 0.1-1 s, though large fluctuations in loading efficiency and the destructive nature of ion detection make an accurate measurement difficult. After a reduction in buffer gas pressure and the impurities introduced by it, the Th^{3+} lifetime estimate was extended to several seconds. With sufficiently long confinement of at least hundreds of ^{232}Th^{3+} ions, the transition to fluorescence detection, spectroscopy, and laser cooling is made.

2.4   Ion Traps for Laser Cooling and Spectroscopy of Thorium

For laser cooling and spectroscopy of trapped ions, circular trap rods suffice, allowing for much simpler electrode machining and providing better transverse optical access than hyperbolic trap rods. Without deviating significantly from the hyperbolic trap in design and dimensions, the "cloverleaf" trap of Figure 11 is used for initial ^{232}Th^{3+} laser cooling and high-resolution spectroscopy. Circular SS304 rods of length 37 mm and diameter 9.5 mm are used to form the quadrupole potential and define the trap radius r_0 to be 4.0 mm. The endcaps are composed of a pair of 9.5 mm thick SS304 plates which have 6.2 mm diameter holes drilled through for axial optical access and ion loading. The endcap thickness is

chosen for enhanced dynamic loading/gating with lower voltages and to remove direct line-of-sight access of ablation materials to the trap rods. This reduces the possibility of contact potential formation on the trap rods. Contact potentials create stray electric fields within the trap, offsetting the trap potential minimum from the rf potential minimum and increasing micromotion heating of the ions (Equation (26)) [17]. The cloverleaf shape of the endcaps is for increased optical access. Alumina rods and washers are used for alignment and electrical isolation between the trap rods and endcaps.
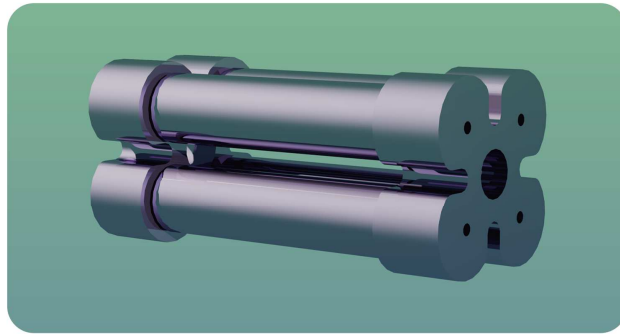
Figure 11: Conceptual drawing of the cloverleaf trap used for ion trajectory simulations in Simion 8.0.

The cloverleaf trap is operated in the balanced mode at a drive frequency of 2-3.1 MHz with endcap voltages of 5-300 V. The balanced mode of operation is observed to offer enhanced ion loading efficiency over that of unbalanced mode loading. Though statistics are lacking, the enhancement factor is estimated from ion fluorescence signals to be 5 - 10 times. This is due to the reduced average rf potential gradient experienced by the ions as they enter the trap along the axis. In addition to rf voltages on the trap rods, small dc voltages in the range ±40 mV are applied to compensate ambient electric fields, ensuring that the trap potential minimum corresponds to that of the rf potential minimum. This minimization of micromotion heating is important for laser cooling Th^{3+}.

Because only small amounts of ^{229}Th (~40 μg) are available for the work done here, further enhancements in Th^{3+} loading efficiency are valuable. Due to the highly energetic plasma nature of ablated Th^{3+}, a linear rf trap of extended length is thought to enhance ion

loading. Relative to the electric potential depth required to simply guide ablated ions along the trap axis, a large radial and axial potential is needed to reflect this axial motion near the endcaps. The high charge density of the initially ablated plume is thought to shield and diminish this required potential depth. By letting the plume propagate and expand longitudinally in the trap before interacting with the far endcap, this effect may be mitigated.
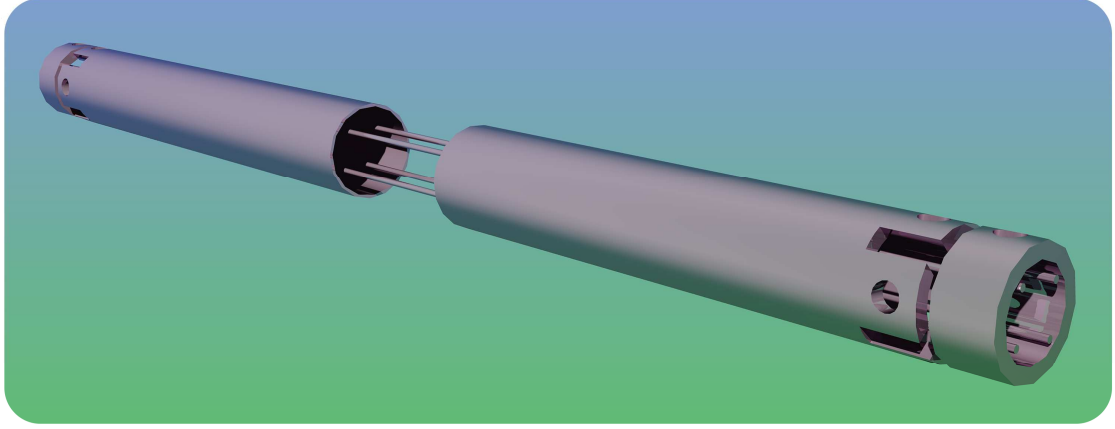
Figure 12: Conceptual drawing of the extended trap used for ion trajectory simulations in Simion 8.0.

To this end, significant departures from the design and dimensions of the cloverleaf trap are made and the extended trap of Figure 12 is used for work with the 229 isotope. Four circular SS304 tubes of length 188 mm and diameter 0.79 mm create the quadrupole potential, defining the trap radius to be 3.31 mm. Endcap electrodes are made from a pair of SS304 circular rings of inner diameter 9.4 mm and length 6 mm which sit flush with the ends of the trap rods and coaxially with the rf potential. To force ions to collect near the center of the trap and to produce sufficiently strong axial confinement with convenient dc voltages, a pair of SS304 tubes of length 82.9 mm and 67.7 mm sit coaxially with the rf potential and are separated by 23 mm. The tube inner diameters are tapered from 9.4 mm near the endcaps up to 11.9 mm near the center of the trap. Electrical isolation and electrode alignment are achieved using machined macor.

The extended trap is operated in the balanced mode at a drive frequency of 4.3 - 8.5 MHz with endcap voltages of 250 V and tube voltages U_{tb} of 3 - 100 V. Figure 13 shows

a numerical solution to Laplace's equation for the electric potential along the trap axis with $V_0 = 0$ V, $U_{ec} = 250$ V, and $U_{tb} = 20$ V. The smooth potential gradient produced by the tube electrodes ensures that small misalignments of the trap do not result in local axial minimums which are not at the trap center. Small dc compensation voltages are also applied to the rf rods in this trap, minimizing ambient electric fields and ion micromotion heating.
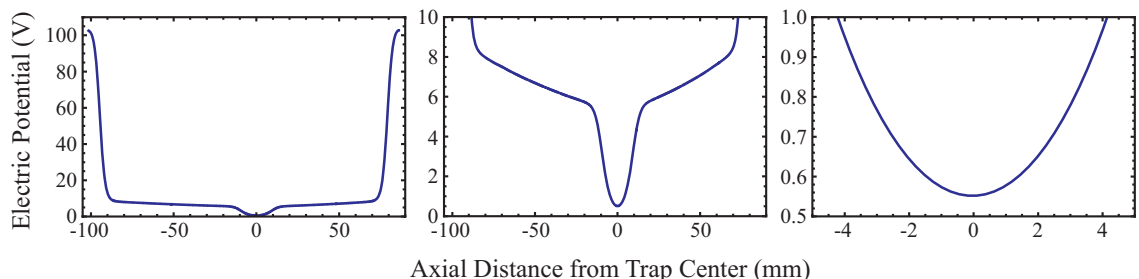
Figure 13: Axial potential within the extended trap. A numerical solution to Laplace's equation for the electric potential created by the extended trap electrodes is done using Simion 8.0. $U_{ec} = 250$ V, $U_{tb} = 20$ V, and $V_0 = 0$ V.

With the small ratio of trap rod diameter to trap radius used in the extended trap, large numeric-aperture lenses may be fully utilized for fluorescence collection and ion imaging transverse to the trap axis. The smaller trap rods also reduce laser scatter into the detector/camera from trap electrodes. Figure 14 shows construction of an earlier version of the extended trap, as well as a demonstration of transverse and axial laser alignment through the trap center.

2.5 Vacuum and Buffer Gas Systems

Because Th^{3+} is a highly charged system, it has an increased electron affinity over other, singly charged ions which are commonly confined in traps for long periods of time. This large affinity leads to increased charge exchange and chemical reaction probabilities with background molecules in the vacuum environment [24], ultimately resulting in a substantially reduced lifetime within the trap. In order to make laser cooling and spectroscopy experiments viable, care must therefore be taken to minimize the vacuum environment
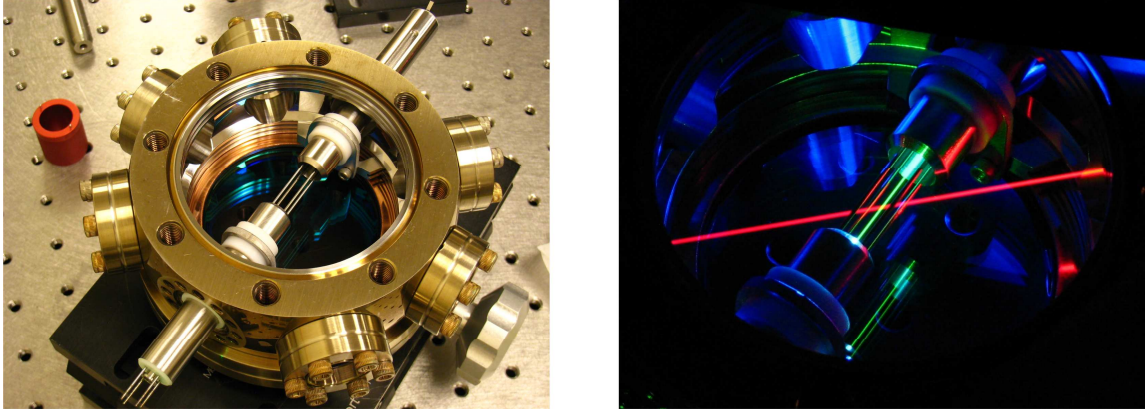
Figure 14: Photos of the first version of the extended trap. A demonstration of laser alignment is shown via visible laser light scattering from particles in the atmosphere.

base pressure and the impurity levels of the introduced helium buffer gas.

The experiments in this work are all done in stainless steel ultra-high vacuum chambers assembled with copper gasket-sealed conflat flanges. Alumina-insulated electrical feedthroughs and stainless steel wire are used for introducing voltages onto trap electrodes and the CEM. Conflat viewports of 7056 glass, which are anti-reflection coated for 984 nm and 690 nm light, are used for introducing optical fields and collecting ion fluorescence. In the chamber housing the extended trap, a linear translation feedthrough is used to place any one of four thorium samples in position for ion loading. An all-metal variable leak valve is used to introduce helium buffer gas and a $\sim$ 50 l/s turbo molecular pump is used to continuously remove the helium. A $\sim$ 50 l/s ion pump and titanium sublimation pump are used in conjunction with the turbo pump to maintain ultra-high vacuum when helium is not introduced into the system. Vacuum pressure is measured using an ionization gauge.

In order to achieve ultra-high vacuum, multiple critical steps are taken. The chamber is pumped to $\sim 10^{-6}$ Torr using the turbo pump backed by a dry scroll pump, after which all titanium sublimation pump filaments are fired in series and the ion pump and ion gauge are then turned on. At a base pressure of $\sim 10^{-7}$ Torr, a residual gas analyzer is used in conjunction with helium to check for leaks in the chamber. With no detectable leaks at a level of $\gtrsim 10^{-9}$ Torr-l/s, the entire chamber is baked at 200 - 350 C for 5 - 10 days.

After the bake, the chamber is cooled back to room temperature in ∼ 12 hrs. The titanium sublimation pump filaments are fired several times over a week-long period, resulting in a base vacuum pressure of $< 10^{-11}$ Torr. The chamber housing the hyperbolic trap did not include a titanium sublimation pump, limiting its base pressure to ∼ 10^{-10} Torr.

The source of helium buffer gas and its transfer line to the ultra-high vacuum chamber have evolved from initial use. The chamber housing the hyperbolic trap used compressed helium of purity > 99.999%, unbaked copper refrigerator tubing as a transfer line, and a brass pressure regulator to control the helium pressure within the line. Figure 15 shows lifetime measurements at various buffer gas pressures using this configuration. The extended lifetime at lower helium pressure indicates a buffer gas-induced lifetime limitation. The cooling rate from helium buffer gas is also observed via fluorescence turn-on as the ion Doppler broadening is reduced and the fluorescence lasers interact with a larger fraction of the velocity distribution.

One may obtain information regarding loss rates due to background vacuum impurities and buffer gas impurities by plotting the measured ion loss rate (inverse of trap lifetime) vs. helium pressure [24]. A maximum trap lifetime (at zero buffer gas pressure) may be extrapolated via a linear fit to such data. Figure 16 shows a plot using the data from Figure 15 and a linear fit, suggesting a minimum loss rate of 0.10 Hz in this temperature regime. It should be noted that at ultra-cold temperatures, the loss rate is expected to be lower for a given vacuum environment due to the reduced ion velocity and collision cross-section.

The ion loss rate due to helium impurities is reduced to a negligible level by making the transition to a helium source of > 99.9999% purity, a stainless steel grease/oil-free pressure regulator designed for ultra-high purity gas use, and a stainless steel ultra-high vacuum bellows for helium transfer which is initially evacuated and baked at ∼ 200 C for 24 hrs to remove contaminants. Figure 17 shows that confinement times in the extended trap are nearly independent of helium pressure with this type of system. The base loss rate

25
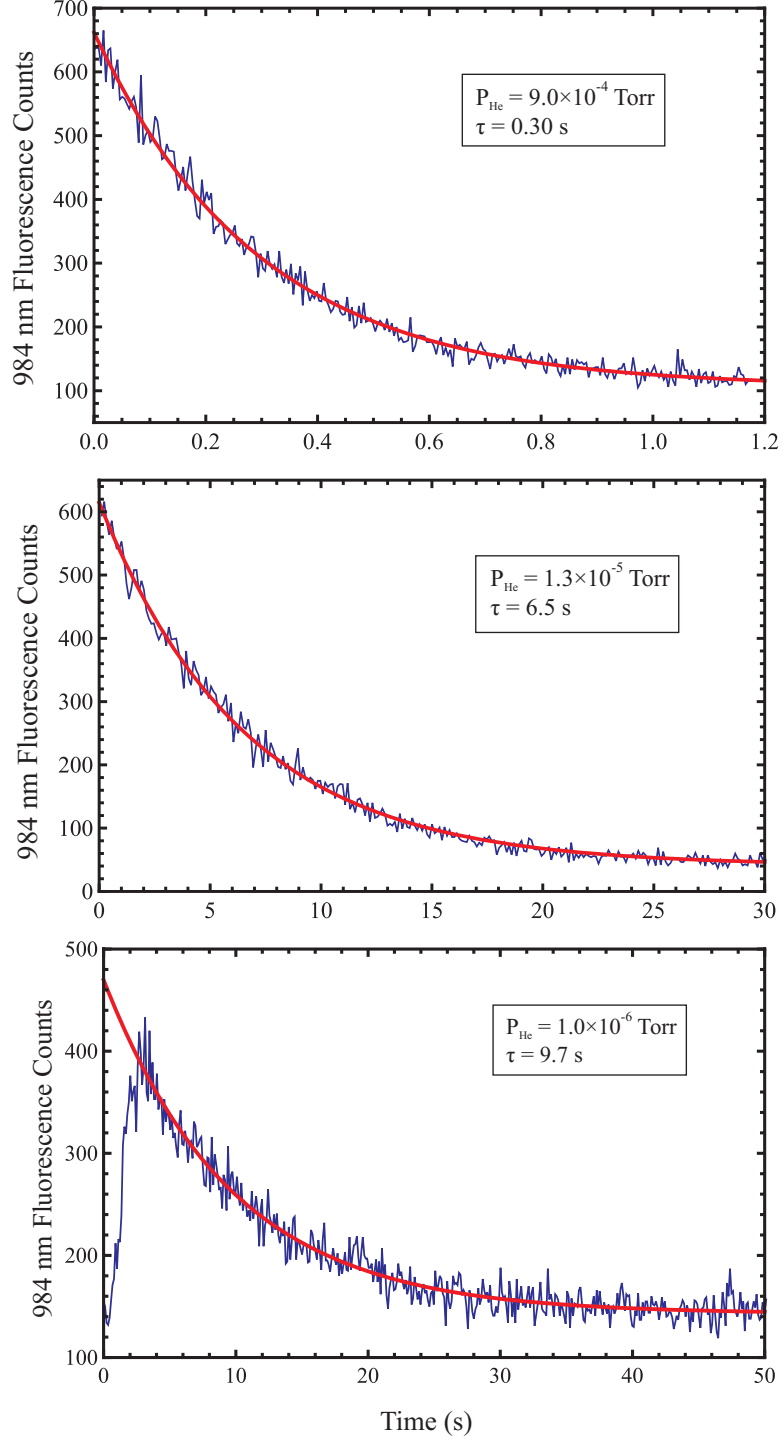
Figure 15: Fluorescence signals measuring confinement lifetimes for ^{232}Th^{3+} at various buffer gas pressures in the cloverleaf trap.

is uncharacteristically high in this data due to a contaminant near the turbo pump flange.

After removal of the contaminant, the confinement time was extended to a couple hundred
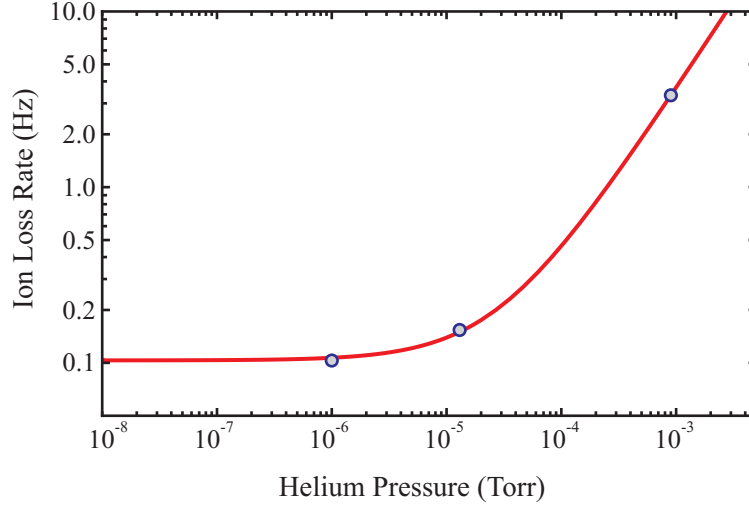
Figure 16: Ion loss rate from confinement lifetime data of Figure 15 and a linear fit. The extrapolated background loss rate is 0.10 Hz.

seconds.
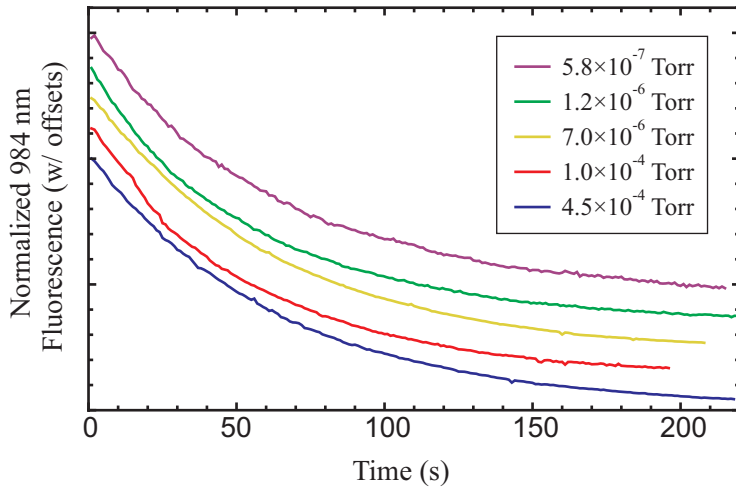
Figure 17: Ion confinement lifetimes in the extended trap after minimization of helium buffer gas impurities. Confinement lifetimes are observed to be nearly independent of helium pressure.

In the case where ions are laser cooled and buffer gas is not present, the low ion velocities reduce the collision cross-section which is thought to be the cause for extended ion lifetimes. Figure 18 shows the lifetime of an initially large ($\sim$ 3000 ions) laser cooled crystal in the cloverleaf trap. Ion lifetimes are further extended to a large fraction of an hour with few-ion linear crystals. The linear crystal lies along the rf potential minimum where rf

27

micromotion is minimal, which in turn minimizes the ion velocities and collisional cross-sections.
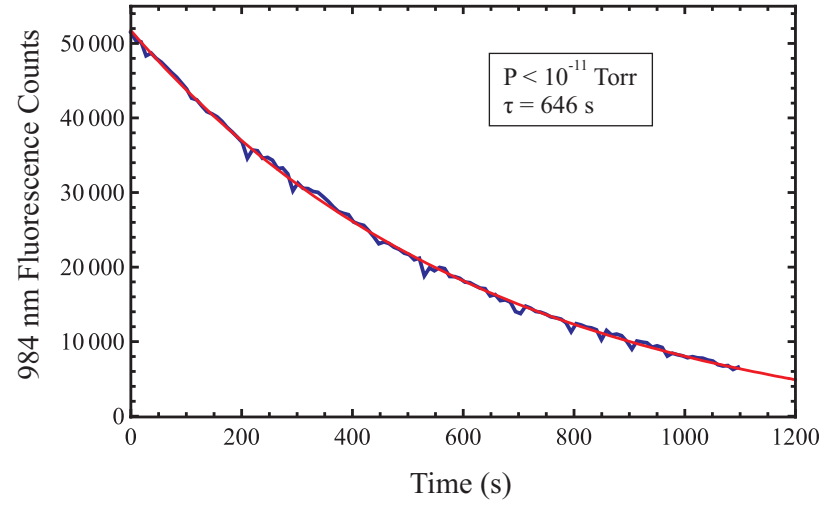
Figure 18: Fluorescence decay from a crystallized sample in the cloverleaf trap. No buffer gas is present.

2.6 Trap Electronics

The circuit generating high voltage rf for ion trapping is shown in Figure 19. This resonant circuit provides two pairs of out-of-phase rf sine waves for running a trap in the balanced mode. Independent dc offsets may be added to the outputs to generate a non-zero *a* as well as to compensate for ambient electric fields, ensuring that the trap minimum corresponds to the rf potential minimum to minimize ion micromotion and heating. A secular excitation signal may also be superposed onto the rf voltage.

The output load of the circuit should have $\lesssim 1000$ pF capacitance to ground and infinite resistance to ground. The inductance *L* of TR3 and the capacitance *C* of the trap rods, vacuum feedthrough, and transmission line from TR3 to the feedthrough dominate the circuit and largely determine the resonant angular frequency Ω. This may be expressed as

$$\Omega = \frac{1}{\sqrt{LC}} \tag{27}$$

while the quality factor *Q* and voltage step-up *S* from TR3 ideally scale as

$$Q \propto \sqrt{\frac{L}{C}} \quad \text{and} \quad S \propto N \tag{28}$$

where *N* is the number of secondary turns on TR3. This suggests that *C* should be kept as low as possible to achieve high voltage and high frequency output. This is done in minimizing the transmission line contribution to *C* by connecting the output ends of the TR3 secondaries directly to the feedthrough pins.

The manufacturer specifications for the iron powder core of TR3 indicate $L = 9.6$ nH/N^2. In the case of the extended trap, capacitance due to the feedthrough and all four trap rods is measured to be ~ 150 pF. Experimental results for this system produce (29 turns, 4.3 MHz), (22 turns, 6.1 MHz), and (17 turns, 8.5 MHz), which agree with expectation. The rf voltage amplitude is limited in these cases to ~ 1500 V due to shorting across secondary wires of TR3.

With smaller *N* used to achieve larger Ω, an increased current draw from the rf amplitude control supply is required to compensate for reduced voltage step-up. This results in

increased heat dissipation at Q1 and Q2 and possibly shortened MOSFET lifetimes. The iron powder core of TR3 may also overheat, shifting the circuit resonant frequency and possibly degrading the magnetic qualities of the core material and therefore the voltage step-up produced. To minimize these effects, a ∼ 30 cubic foot/meter fan sits ∼ 10 mm above the circuit for cooling while Q1 and Q2 are each attached to a ∼ 30 mm square ball grid array heat sink. The average power dissipated is also minimized by ramping the rf voltage to high values only when needed, i.e. when loading and executing low-mass filtration.

Because the circuit operates in the MHz regime, care is taken in board layout, transformer construction, and grounding to minimize the presence of higher harmonics in the output rf spectrum. Various design characteristics reflect this. The section of the circuit to the left of TR2 is as localized as possible on a Twin Industries 8100-45-LF prototyping board to minimize the length of the traces. The number of jumpers used to cross traces is also minimized. A grounding plane on the circuit board is essential to achieve a well defined common ground. TR2 and TR3 are oriented on the circuit board such that their axes of symmetry are orthogonal to each other, reducing the inductive coupling between them. Finally, the four secondaries of TR3 are carefully twisted together and evenly distributed around the core to maximize and equalize their inductive coupling to the primary (Figure 19 inset). Output spectra at 4.3 MHz and 8.5 MHz are shown in Figure 20. The highest noise component for this circuit appears at the third harmonic of the resonant frequency and is observed to be 50 - 60 dB down across the amplitude and frequency ranges used. This level of noise is not expected to be detrimental in this work.

The circuit used for endcap switching, designed with the aid of Scott Centers of the School of Physics Electronics Shop, is shown in Figure 21.
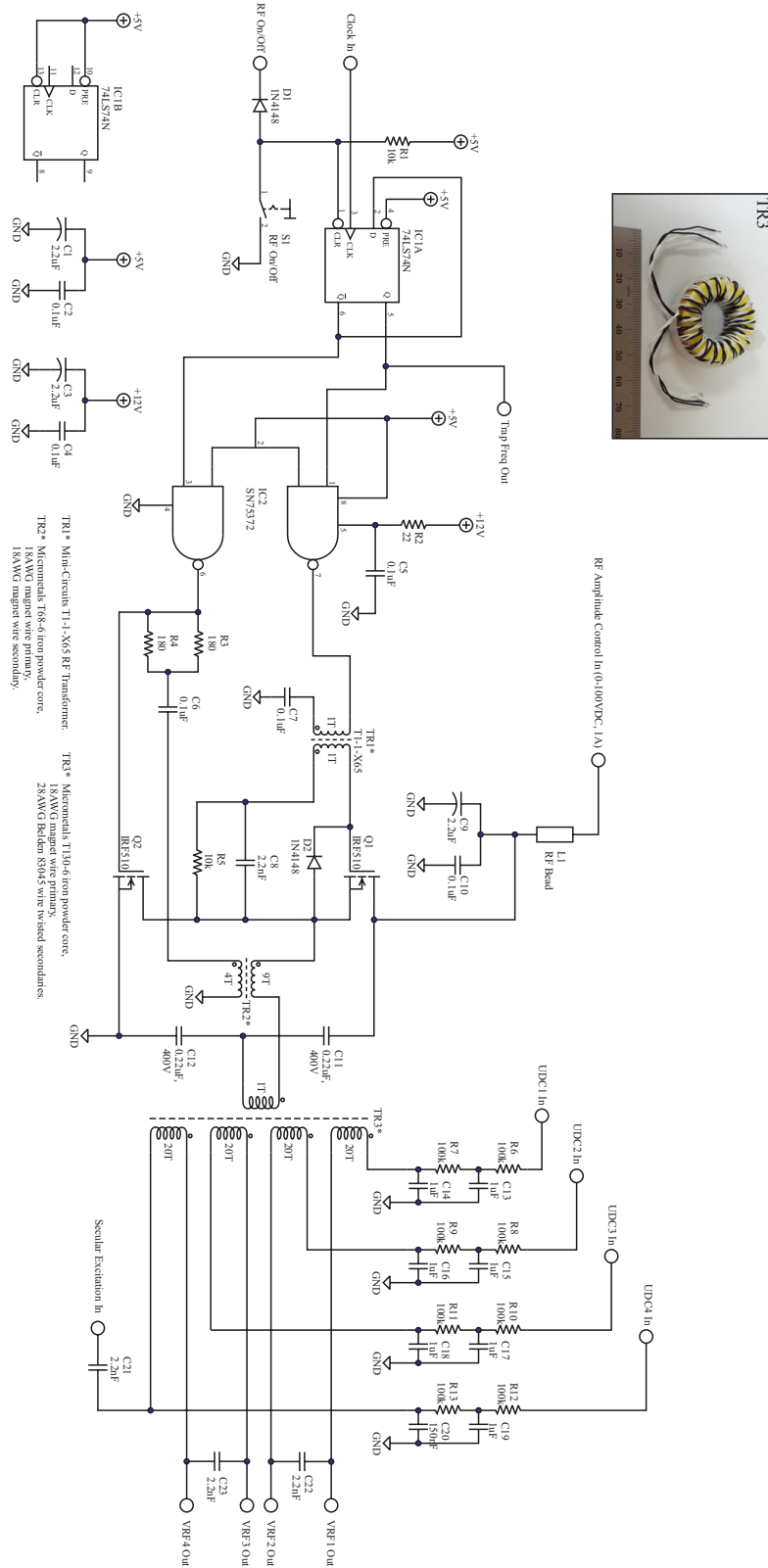
Figure 19: RF circuit used to drive ion traps in the balanced mode. The main design of the circuit is based on that used in the Stanford Research Systems RGA300. Modifications are made to suit the ion trapping, mass spectrometry, and laser cooling experiments done here.

31

a)

CENTER 25.00 MHz   SPAN 50.00 MHz
RES BW 30 kHz   LOG 10 dB/div

b)

CENTER 30.00 MHz   SPAN 60.00 MHz
RES BW 30 kHz   LOG 10 dB/div
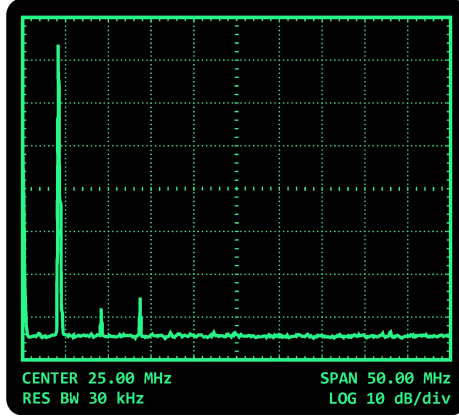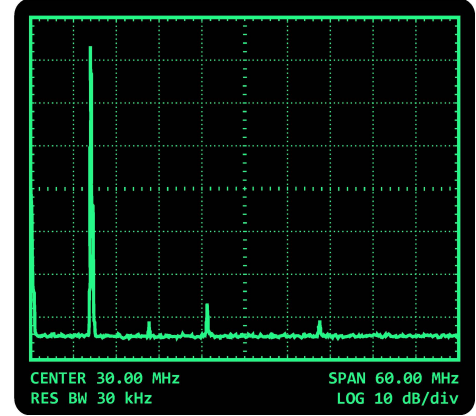
Figure 20: RF spectrum of the rf drive circuit output. The largest noise components are ~ 60 dB down across all resonant frequencies and rf amplitudes used in this work.
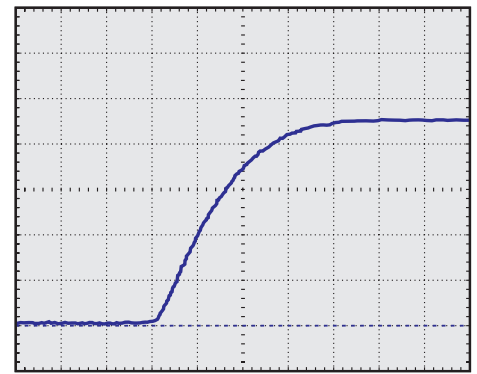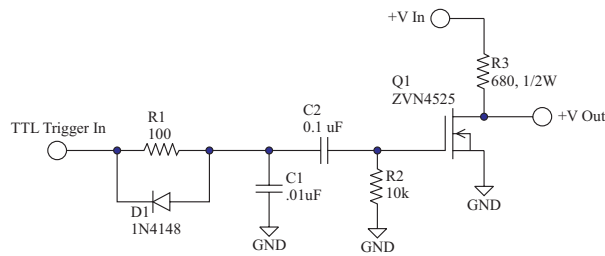
Endcap Voltage 50 V/div   200 ns/div

Figure 21: Endcap switching circuit. The circuit is used to ramp endcap voltages to a few hundred volts in < 1 μs. Ramp times from ground to 300 V have been observed in under 200 ns for small capacitive loads.

CHAPTER III

THORIUM IV LASER COOLING

3.1 *Laser Cooling of Weakly Bound Atoms*

For a sufficient discussion of laser cooling, a brief review of relevant atom-light interaction relations is necessary. For simplicity, consider a two-level atom at rest with ground state $|g\rangle$, excited state $|e\rangle$, electric dipole moment $\mu = e \langle e| z |g\rangle$, and eigenstate energy splitting $\hbar\omega_0$. The excited state decay rate γ may be defined by [25]

$$\gamma = \frac{\omega_0^3 \mu^2}{3\pi\epsilon_0 \hbar c^3}. \tag{29}$$

If the atom is illuminated with a laser field of electric field amplitude E_0, polarization along $\hat{z}$, and frequency ω near ω_0, the resonant Rabi frequency Ω is written as

$$\Omega = \frac{\mu E_0}{\hbar}. \tag{30}$$

and the average excited state population ρ in the steady state takes the form

$$\rho = \frac{\Omega^2}{\gamma^2 + 2\Omega^2 + 4\delta^2}. \tag{31}$$

Here, $\delta = (\omega - \omega_0)$ is the laser detuning from atomic resonance. This absorption profile is a Lorentzian lineshape with a full width at half maximum of

$$\gamma' = \gamma \sqrt{1 + \frac{2\Omega^2}{\gamma^2}} \tag{32}$$

At low laser intensities ($\Omega \ll \gamma$), $\gamma' \approx \gamma$ whereas at high laser intensities ($\Omega \gg \gamma$), $\gamma' \approx \sqrt{2}\Omega$. The broadening effect of the absorption profile due to increased laser intensity is known as power broadening. Between these two laser intensity regimes, saturation of the transition is said to occur when $\Omega = \gamma/\sqrt{2}$. From the average excited state population and

the excited state decay rate, the steady-state photon scatter rate from the atom is expressed as

$$\gamma_p = \rho \, \gamma. \tag{33}$$

Equations (31) and (33) will be used in conjunction with the relativistic Doppler shift in the following discussion of laser cooling.

The relativistic Doppler shift is the discrepancy in electromagnetic radiation frequency among two observers which are traveling at different velocities. In the system relevant here, a laser at rest in the lab frame emits radiation of frequency ω_l and k-vector $\vec{k}_l = (\omega_l/c) \, \hat{k}_l$ while an atom moves with velocity $\vec{v}$ with respect to the lab. From Einstein's Theory of Special Relativity, the frequency of the laser light in the reference frame of the atom is [26]

$$
\begin{aligned}
\omega_a &= \left(\omega_l - \vec{k}_l \cdot \vec{v}\right) \sqrt{1 - \beta^2} \\
&= \left(\omega_l - \vec{k}_l \cdot \vec{v}\right) \left[1 - \frac{\beta^2}{2} - \frac{\beta^4}{8} - \frac{\beta^6}{16} - \cdots \right]
\end{aligned}
\tag{34}
$$

where $\beta = |v|/c$. The frequency shift in the reference frame of the atom can be written

$$\delta\omega_a = -\vec{k}_l \cdot \vec{v} - \frac{\omega_l \, v^2}{2c^2} + \cdots \tag{35}$$

The first term in Equation (35) is the first-order Doppler shift which has directional dependence and is at the heart of Doppler laser cooling. The second term, the second-order Doppler or time dilation shift, is only dependent upon the amplitude of velocity and, therefore, only shifts the frequency to the red. All higher orders in β are neglected.

In expressing the transition absorption profile of the two-level atom above, zero velocity is assumed. If the atom is in motion,

$$\rho \rightarrow \rho_D = \frac{\Omega^2}{\gamma^2 + 2\Omega^2 + 4\left(\delta - \vec{k}_l \cdot \vec{v}\right)^2} \tag{36}$$

where the time dilation shift is neglected. The Doppler shift acts simply to translate the absorption profile along the frequency axis. For an atom at thermal equilibrium with its environment, it assumes a Maxwell-Boltzmann velocity distribution. Along a given direction,

this normalized distribution is

$$P(v_i) = \sqrt{m/2\pi k_B T} \, e^{-\left(mv_i^2/2k_B T\right)} \tag{37}$$

where m is the mass of the atom and k_B is Boltzmann's constant. In the case where $k_l v_{rms} \gg \gamma'$, which is commonly achievable at 300 K, ρ may be thought of as being probabilistically distributed throughout frequency space according to $P(v_i)$. The average excited state population then takes a Gaussian form and may be approximated as

$$\rho_D \approx \sqrt{\frac{\ln 2}{\pi}} \, \frac{\gamma'}{\gamma_D} \, e^{-\left(4\ln 2\,\delta^2/\gamma_D^2\right)} \tag{38}$$

where $\gamma_D = 2\omega_0 \sqrt{2k_B T \ln 2/mc^2}$ is the full width at half maximum of the Doppler broadened lineshape.

With the spectral shift of ρ due to the atomic velocity in mind, laser cooling is treated in a manner similar to that of Itano *et al.* [59]. Consider a photon scattered from the two-level atom which has velocity $\vec{v}$. While illuminated with a nearly resonant laser beam, it absorbs a photon of momentum $\vec{k}_l$ and spontaneously emits a photon of momentum $\vec{k}_{em}$ within a time of order $1/\gamma$. This leaves the atom with a new velocity $\vec{v}\,'$. To first order in β, conservation of momentum and energy lead to a change in atomic kinetic energy per scattering event of

$$\Delta E_i = \frac{\hbar^2 (k_{l,i} - k_{em,i})^2}{2m} + \hbar(k_{l,i} - k_{em,i})v_i \quad (i = x, y, z). \tag{39}$$

This result assumes the atom to be in free motion during the scattering event. It is also valid, however, for an atom confined within a three-dimensional harmonic potential when the trap oscillation frequencies ω_x, ω_y, $\omega_z \ll \gamma$. In this case, the excited state decay process occurs on a much shorter time scale than does motional change of the atom due to the trapping potential. This is known as the weak binding limit and will be used here. At this point, we assume for the sake of simplicity that the spontaneous emission from scattering events is isotropic in space, though this assumption is commonly violated in realistic atoms. We will

also assume that $|k_l| = |k_{em}|$. In averaging over 4π steradians of spontaneous emission,

$$\langle \Delta E_i \rangle = \left(\cos^2 \theta_i + \tfrac{1}{3} \right) R + \hbar k_l v_i \cos \theta_i \tag{40}$$

where $v_i = v_{0i} \cos(\omega_i t)$, $R = (\hbar^2 \omega_0^2)/(2mc^2)$ is the atomic recoil energy, and θ_i is the angle between $\vec{k}_l$ and the ith Cartesian component in the trap basis. The time rate-of-change of the atomic kinetic energy may be expressed as

$$\frac{\mathrm{d}E_i}{\mathrm{d}t} = \gamma \rho_D \langle \Delta E_i \rangle \tag{41}$$

For $\delta < R/\hbar \cong 0$, ρ_D is larger for negative velocities than for positive velocities until very low temperatures are achieved. This net reduction in atomic kinetic energy is the process referred to as Doppler laser cooling.

In the case where an atom has undergone considerable laser cooling such that its Doppler broadening is much less than its natural linewidth ($k_l v_{rms} \ll \gamma$), Equation (41) may be expressed as

$$\frac{\mathrm{d}E_i}{\mathrm{d}t} = \gamma \left(\frac{\Omega^2}{\gamma^2 + 2\Omega^2 + 4(\delta - k_l v_i \cos \theta_i)^2} \right) \langle \Delta E_i \rangle \tag{42}$$

where it is assumed that $R \ll \hbar \gamma$, δ. Expanding ρ_D in terms of $k_l v_i$ and integrating the ion motion over one oscillation in the trap, Equation (42) may be expressed as

$$\frac{\mathrm{d}E_i}{\mathrm{d}t} \approx \gamma \rho \left[\left(\cos^2 \theta_i + \tfrac{1}{3} \right) R + \frac{4 \delta \hbar (k_l v_{0i})^2 \cos^2 \theta_i}{\gamma^2 + 2\Omega^2 + 4\delta^2} \right] \tag{43}$$

The steady-state (minimum) motional oscillation amplitude may be solved by setting $\mathrm{d}E_i/\mathrm{d}t$ to zero (result not shown). The minimum kinetic energy in the ith direction is then $E_{Ki} = \tfrac{1}{2} m v_{rms\,i}^2 = \tfrac{1}{4} m v_{0i}^2$. By setting $\mathrm{d}E_{Ki}/\mathrm{d}\delta$ equal to zero and solving for δ, the laser detuning at which the minimum temperature occurs is

$$\delta_{min} = -\frac{\gamma}{2} \sqrt{1 + \frac{2\Omega^2}{\gamma^2}} = -\frac{\gamma'}{2} \tag{44}$$

For $\Omega \ll \gamma$, $\delta_{min} = -\gamma/2$ and E_{Ki} may be expressed as

$$E_{Ki} = \left(\frac{1 + 3 \cos^2 \theta_i}{24 \cos^2 \theta_i} \right) \hbar \gamma. \tag{45}$$

36

It is clear from this result that if the cooling laser has no component along the ith axis, the atom is not directly laser cooled. In fact, it is heated in that dimension without bound. This is due to the isotropic recoil heating from spontaneous emission of the scattered photons combined with the lack of any thermalization mechanisms within the trap. When considering the total kinetic energy $E_K = E_{Kx} + E_{Ky} + E_{Kz}$, a minimum value is reached when $\vec{k}_l$ is oriented along the vector $\hat{x} + \hat{y} + \hat{z}$. In this case,

$$E_{Kx,y,z} = E_D = \frac{\hbar\gamma}{4} \quad \text{and} \quad E_K = \frac{3\hbar\gamma}{4}. \tag{46}$$

The value $E_D = \hbar\gamma/4$ is known as the Doppler cooling limit and is recognized as the minimum kinetic energy achievable with the Doppler cooling process. This one-dimensional energy (quadratic in velocity) has a corresponding temperature of $T_D = \dfrac{2E_D}{k_B} = \dfrac{\hbar\gamma}{2k_B}$, known as the Doppler temperature. It is interesting to note that with a single cooling beam oriented purely along the ith trap axis, $E_{Ki} = \hbar\gamma/6 < E_D$. This is due to the partial dissipation of recoil heating along the two transverse directions of motion which, as previously mentioned, are not cooled at all.

Because heating occurs without bound for any uncooled dimensions, it is critical to have a cooling beam component along all three trap axes. It is also critical that $\omega_x \neq \omega_y \neq \omega_z \neq \omega_x$. Otherwise, a degeneracy in any two trap frequencies produces a rotationally invariant system and, therefore, motion transverse to the cooling beam is decoupled from the cooling laser.

In the case where many atoms are trapped, i.e. hundreds or thousands, collisions between them act to randomly distribute kinetic energy along all three dimensions. For an average atomic collision rate which is much greater than γ, ideal themalization may be assumed. This approximation is made here. In this case, the total kinetic energy of the system is equally distributed among all three spatial dimensions. This results in a rotationally invariant system when considering laser cooling and leaves the net recoil heating transverse to $\vec{k}_l$ equal to zero. There is no net exchange of energy among spatial dimensions. From

these arguments, Equation (40) becomes, for motion along $\vec{k}_l$,

$$\langle \Delta E_l \rangle = 2R + \hbar k_l v_l. \tag{47}$$

Using the same treatment here as that used for the single atom case, the minimum attainable kinetic energy along the dimension of laser cooling is $E_{Kl} = E_D = \hbar\gamma/4$. Again, because thermalization is assumed to be ideal, both dimensions transverse to $\vec{k}_l$ have kinetic energies equal to that of E_{Kl}, and so $E_K = 3\hbar\gamma/4$.

For a collection of bound ions which are cooled to such low temperatures, phase transitions may occur which transform the ion sample from a gaseous state to a liquid or solid crystalline state. A brief review of the literature on this topic is useful in order to anticipate ion dynamics during laser cooling of Th^{3+}. The thermodynamic state of this type of system is governed by a single parameter, the plasma-coupling parameter Γ [28], which is the ratio of Coulomb energy to motional energy and is expressed as

$$\Gamma = \frac{Q^2}{4\pi\epsilon_0 a_{WS} k_B T} \tag{48}$$

where $a_{WS} = \left(\frac{3}{4\pi n_0}\right)^{1/3}$ is the Wigner-Seitz radius, $n_0 = \frac{4\epsilon_0 (\kappa_r V_0)^2}{m r_0^4 \Omega^2}$ is the zero-temperature ion density, and ϵ_0 is the vacuum permittivity. Molecular dynamics simulations [29] and experimental observations [28] have determined that in large ion samples, an abrupt transition from a gas to a liquid state occurs for $\Gamma \sim 2$. In this case, the radial ion density shifts from a Gaussian-like distribution towards a step function distribution, bringing the ion density to nearly its maximum value. As Γ is increased, radial shells begin to form while diffusion is still present in the transverse directions. Well defined shells are observed to be fully formed for $140 \lesssim \Gamma \lesssim 300$. Beyond $\Gamma \sim 300$, fully crystalline structures slowly begin to form and are clearly observable at $\Gamma \sim 400$.

Applying these results to the traps in this work, order of magnitude estimates may be made for the temperatures at which laser cooled Th^{3+} is expected to transition as well as how these temperatures compare with the Doppler limit of the 1088 nm cooling transition.

Considering the extended trap where $r_0 = 3.31$ mm, $V_0 = 120$ V, $\kappa_r = 0.933$, and $\Omega = 2\pi \times 6$ MHz,

$$T(\Gamma = 2) = 6.5 \times 10^5 \, \gamma_D = 2.3 \, \text{K}$$

$$T(\Gamma = 140) = 9.3 \times 10^3 \, \gamma_D = 33 \, \text{mK}$$

$$T(\Gamma = 400) = 3.2 \times 10^3 \, \gamma_D = 11 \, \text{mK}$$

$$T(\Gamma = 1\,300\,000) = 1 \, \gamma_D = 3.5 \, \mu\text{K}$$

From these estimates, it is clear that phase transitions should be observed when laser cooling Th^{3+} near the Doppler limit. In fact, the demonstration of fully crystallized thorium stands as an important benchmark in progressing toward precision laser spectroscopy in $^{229}Th^{3+}$.

In this section, we have reviewed the basics of Doppler laser cooling of bound two-level atoms in the weak binding regime and the temperature limits of the technique. In the next section, this technique will be extended to cooling real multi-level atoms, particularly $^{232}Th^{3+}$ ions confined in an rf trap. This real system in much more complicated, though many simplifying approximations can and will be made.

3.2   *Laser Cooling Trapped* $^{232}Th^{3+}$

The treatment of laser cooling in the previous section was applied to a fictitious two-level atom in an ideal harmonic trap. This toy model is useful in illustrating the basic ideas and results of laser cooling, though various other realistic complications must not be ignored when performing experiments in the lab. The realistic system used in this work is composed of a single or large number of Th^{3+} ions confined in an rf trap. Initial work in laser cooling $^{232}Th^{3+}$ is discussed here.

Because $^{232}Th^{3+}$ has only one valence electron, its electronic structure is relatively simple. The four lowest fine structure energy levels are shown in Figure 22 along with the
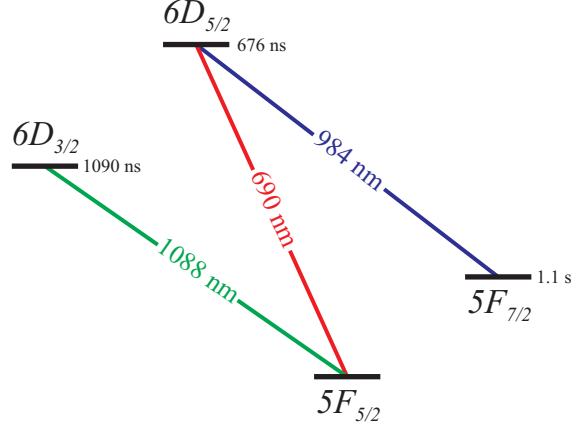
Figure 22: Four lowest-lying fine structure levels of Th^{3+} with associated electric dipole transitions used for laser cooling and ion imaging. The excited state lifetimes are theoretical calculations taken from [30].

allowed electric dipole transitions [22]. All four levels are used for laser cooling and imaging of Th^{3+} ions. The nucleus of the 232 isotope has no nuclear spin, resulting in a purely Coulomb interaction with the orbiting electrons. Consequently, there is no hyperfine structure to modify the levels shown. Each fine structure level is, however, composed of $2J + 1$ Zeeman sub-levels. The magnetic moment of the orbiting valence electron interacts with an external magnetic field $\vec{\mathcal{B}}$, resulting in a spatial orientation dependence of the ion energy. For small magnetic fields oriented along $\hat{z}$ (quantization axis), the otherwise degenerate Zeeman sub-levels are shifted by an amount [31]

$$\Delta E_Z = \mu_B\, g_J\, m_J\, \mathcal{B} \tag{49}$$

where $\mu_B = \dfrac{e\,\hbar}{2\,m_e}$ is the Bohr magneton and m_e is the electron mass, g_J is the Landé g-factor specific to each fine-structure level of the atom, and m_J is the magnetic quantum number which may take on a value in the range $(-J, -J + 1, \ldots, J - 1, J)$. Figure 23 illustrates such level splitting for the 1088 nm transition in the low field regime. The differential linear Zeeman shift for π-transitions on the 1088 nm line is ≈ 80 kHz/G.

40
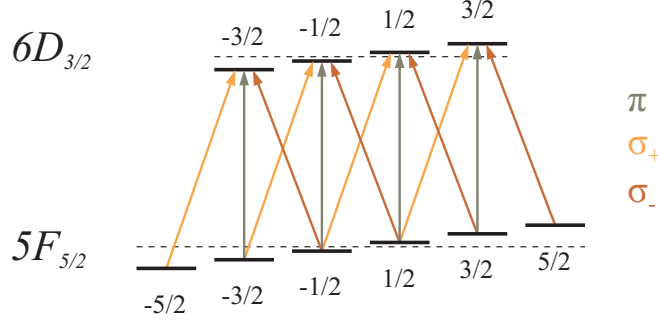
Figure 23: Zeeman structure of the fine structure levels composing the semi-closed 1088 nm electric dipole transition.

Because there is orientation dependence of the system, the polarization $\hat{e}$ of the cooling/excitation laser field is important. For three dimensions of space, there are three polarizations of light with respect to $\hat{z}$, $\vec{\mathcal{B}}$. The standard polarization basis is

$$\hat{e}_0 = \hat{z} \quad \text{and} \quad \hat{e}_{\pm 1} = \mp \frac{1}{\sqrt{2}} (\hat{x} \pm i\hat{y}) \tag{50}$$

where $\hat{e}_0$ is referred to as π-polarization and $\hat{e}_{\pm 1}$ is referred to as $\sigma_{\pm}$-polarization for atoms quantized with respect to the z-axis. This basis is convenient because the three polarizations correspond to purely $\Delta m_J = 0, \pm 1$. Hence, as a thorium ion is excited with a particular polarization, the orientation of it with respect to the quantization axis may change. This change in angular momentum orientation is shown in Figure 23 for π and σ transitions at 1088 nm.

If the magnetic field is zero and the polarization of the light is static, Figure 23 also illustrates that for the 1088 nm transition in particular, the use of either π, σ_+, or σ_- light leaves two states dark [32]. A dark state is defined as a state in which the electric dipole transition matrix element $\langle e|\vec{r} \cdot \hat{e}|g\rangle$ vanishes. It turns out that any superposition of π, σ_+, and σ_- light also leaves two states dark. This is clear if one recognizes that a dark state may also be a superposition of eigenstates. Because the total angular momentum J of the excited D orbitals in Figure 22 is less than or equal to that of the lower F orbitals, dark states are a concern for all three transitions. If not removed, these dark states are eventually populated via spontaneous decay from excited states and prohibit the ion from scattering

large numbers of photons. This eliminates the laser cooling and fluorescence imaging processes.

Removal of dark states is done in this work by using pairs of counter-propagating lasers with different polarizations and a non-zero magnetic field. The counter-propagating beam configuration creates a spatially varying polarization with a period of half an optical wavelength (neglecting acoustic noise on the retroreflecting mirrors). Ions in the gas and pseudo-liquid phases traverse this lattice sufficiently fast to perceive a randomly fluctuating polarization. This serves to sufficiently destabilize all dark states. At very low temperatures, when ions are fully crystallized, particularly in the linear chain configuration, the decreased ion oscillation amplitude and velocity degrade the utility of the spatially varying light polarization. In this case, the applied magnetic field serves to destroy dark state coherences [32] with the field amplitude and direction in space empirically found by maximizing ion fluorescence at low temperatures. This field (< 1 G) is expected to correspond to Zeeman splittings of not more than several natural linewidths.

With these techniques, the complications of Zeeman structure are reduced to an acceptable level and the ions are assumed to be unpolarized. When dealing with an unpolarized sample and varying optical polarization, it is convenient when speaking of a Rabi frequency to simply average over all transitions from all lower Zeeman sub-levels. Unless stated otherwise, this averaging is used for calculated Rabi frequencies of Th^{3+} in this work. The expression for such calculations is found in [31] and reduced dipole matrix elements are taken from [30].

It is instructive to apply these simplifications to a discussion of laser cooling $^{232}Th^{3+}$. Consider a large number of ions confined in the weak binding limit being laser cooled on the 1088 nm transition. Due to the strong Coulomb coupling between the ions, the sample is assumed to be ideally thermalized. Here, $\gamma = (1090 \text{ ns})^{-1} = 2\pi \times 146$ kHz, $\omega_0 = 2\pi \times 275.5$ THz, and $m = 3.87 \times 10^{-25}$ kg. Expressing the kinetic energy change per scattering event in terms of temperature via the relation $\Delta E_{kin} = \frac{3}{2} k_B \Delta T$, Equation (47) suggests that

$\Delta T \cong 5$ mK at T = 300 K. From this, one sees that $\sim 10^5$ scattering events are required to realize significant cooling.

Of practical importance is the time required to induce sufficient scattering to cool from room temperature. At 300 K, $\gamma_D \approx 2\pi \times 220$ MHz. To reduce the ion temperature to near the Doppler limit, it was previously shown that both Ω and δ should not be much greater than γ in absolute value. For $\Omega = 2\gamma$ and $\delta = -2\gamma$, Equation (38) gives an average excited state population of 0.0009, leading to a cooling time of $\sim 10^5/(0.0009\gamma) = 120$ s. This result may be compared to that for a more traditional ion which is commonly laser cooled, e.g. $^{40}Ca^+$. In that case, the main cooling transition is at 397 nm, $\gamma = (7.1 \text{ ns})^{-1} = 2\pi \times 22$ MHz, $m = 6.68 \times 10^{-26}$ kg and at 300 K, $\gamma_D \sim 2\pi \times 1.5$ GHz. For $\Omega = 2\gamma$ and $\delta = -2\gamma$, the average excited state population is ~ 0.02, leading to a cooling time of ~ 30 ms. When considering rf heating and ion loss rate from the trap, the long cooling time estimate of Th^{3+} suggests that alternative techniques may be required to realize laser cooling.

A straight forward solution to reducing the cooling time of Th^{3+} is to power broaden the transition and detune the cooling laser such that its interaction with the thermal cloud is comparable to that of the Ca^+ example. Considering the 1088 nm transition at room temperature with $\Omega = 300\gamma$ and $\delta = -300\gamma$, the excited state population is ~ 0.12 and the cooling time, ~ 1 s. This result appears much more promising for bring room temperature ions down to tens of Kelvin. The large detuning and Rabi frequency, however, preclude cooling to ultra-low temperatures. Because the reduced temperature decreases $\gamma_D/2\pi$ to tens of MHz, a second cooling field with smaller Rabi frequency and detuning may then be used to achieve ultra-cold temperatures on short timescales. This technique of dual-stage cooling is a convenient alternative to sweeping a single cooling laser frequency and amplitude to efficiently access the temperature ranges of interest.

In addition to increasing the cooling rate of the ions, minimization of external heating is an important task to accomplish when attempting to laser cool Th^{3+}. The dominant heating source of ions stored in rf traps is rf micromotion. Equation (26) suggests that minimal

rf heating occurs for single-ion and many-ion samples with low q and zero electric field offsets. For cooling ^{232}Th^{3+}, sufficiently low q values are found by simply observing a dramatic Doppler narrowing as the rf voltage is lowered. Zeroing ambient fields is more difficult.

Ambient electric field compensation is done in this work by applying dc voltages to the trap rods. Determination of optimal dc compensation voltages is commonly done via the cross-correlation technique [17] where the Doppler shift of an ion due to micromotion is minimized by monitoring and minimizing fluorescence modulation at the trap drive frequency. This method has been employed here, though the low scatter rate of Th^{3+} and long integration times makes this technique too time consuming to be practically useful. Micromotion is minimized for Th^{3+} more conveniently by monitoring ion displacement at different trap depths. In one limiting cases, at very large radial trap depths, an external dc field negligibly shifts the trap minimum. Ions trapped in this regime are located, to a good approximation, at the rf potential minimum. In the opposite limiting case, at very small radial trap depths, an external dc electric field may shift the location of trapped ions by an easily observable amount and even remove them from the trap all together. In minimizing this position shift via dc compensation voltages, excess rf micromotion may be reduced to an acceptable level for laser cooling. Because this process is commonly required in order to laser cool, a Th^{3+} sample cooled via helium buffer may initially be used.

Changes in ion position within the trap are monitored with a low-noise CCD camera which collects fluorescence transverse to the trap axis. Motion within the focal plane of the imaging system is monitored with resolution of one effective pixel size ($\lesssim 10 \ \mu$m) while longitudinal motion is monitored by utilizing the short focal depth of the imaging system, which is $\lesssim 100 \ \mu$m. The spatial resolution in this dimension is substantially less than for the other two, though it is sufficient for this work.

Typical radial trap frequencies used when minimizing micromotion are ~10 kHz and ~200 kHz. Compensation voltages are applied anti-symmetrically with respect to ground

to opposing trap rods so as to leave the electric potential along the trap axis unchanged. In the cloverleaf trap, the compensation voltages are no more than ±30 mV and estimated to change by no more than a few % from day to day. Because the endcap in the extended trap does not behave as an ablation skimmer, ablated material is able to coat the trap rods, generating contact potentials which vary from ablation shot to shot. As a result, the optimal dc compensation voltages might vary from load to load within the range ±50 mV.

As previously mentioned, helium buffer gas may be used to initially minimize micromotion. The buffer gas also serves to enhance ion loading and bring the ions from tens of thousands of Kelvin to about room temperature. This Doppler narrowing is useful for initial laser cooling, particularly when optical power broadening is insufficiently low due to limited laser power. Once the ions are loaded and micromotion has been minimized, the buffer gas is pumped out and laser cooling brings the ions below room temperature. Without removing the helium, collisions overwhelm the laser cooling process and maintain the ion sample at room temperature. Depending on the vacuum chamber geometry, the vacuum pressure falls from $\sim 10^{-5}$ Torr to $< 10^{-11}$ Torr within a few minutes after closing the helium leak valve.

After loading the ions and before laser cooling takes place, a sample purification protocol is executed. V_0 is initially ramped upward such that q approaches the low-mass cut off for Th^{3+}, removing most smaller m/Q's without significantly reducing the population of Th^{3+}. V_0 is then ramped downward such that the radial trap frequencies for Th^{3+} approach zero, removing most larger m/Q's without substantially reducing the population of Th^{3+}. For large trap drive frequencies, $V_{0(max)}$ may not be sufficiently large to remove lighter pollutants. In this case, a secular excitation signal is applied in a manner similar to that used for thorium mass spectrometry. A volt is sufficient here for fast clean ejection. These q-ramp and secular excitation processes work quickly and efficiently for removing m/Q's which are different from Th^{3+} by more than an estimated $\pm$ 20 amu/e. Ultimately, this range covers all observed pollutants such that samples of trapped Th^{3+} may be purified

to 100%.

With simple and robust solutions in place for dark state destabilization, micromotion minimization, and sample purification, $^{232}\text{Th}^{3+}$ ions are laser cooled to crystallization. Laser cooling of thorium was first realized in the cloverleaf trap. This was also the first demonstration of laser cooling of a multiply charged ion. Figure 24 shows the experimental setup for this work. High power 1088 nm beams enter the trap transversely for initial cooling and low power 690 nm and 984 nm fields propagate along the trap axis for low temperature cooling. Utilization of the Λ-system for low temperature cooling is dictated by the limited fluorescence detection options. High quantum efficiency, low-noise single photon counters and cameras are available in the visible and NIR range, but cut off before reaching 1088 nm. Because fluorescence detection is more effective with the Λ-transitions and the low optical power requirements for low-temperature laser cooling are favorable for ion detection signal-to-noise, low temperature cooling is done via 690 nm and 984 nm light.

The low temperature cooling beams are oriented along the trap axis to minimize scatter into the imaging system and to minimize the observed first-order Doppler shift due to rf micromotion. This motion is largely transverse to the trap axis and an absorption spectrum, when probed along this motion, is severely modulated at the trap drive frequency. For a laser tuned near resonance, substantially reduced interaction between the ion and laser field may occur for ions with large modulation depths. The high-intensity fields which broaden transitions to greater than the drive frequency, however, are less impacted by this effect and may be oriented with a significant transverse component.

Within the cloverleaf trap, four 1088 nm beams with elliptical polarization cool the ions from room temperature. These beams propagate in a common plane and at 30° angles to the trap axis. Each beam has a 1 mm × 4 mm cross section and 4 mW of optical power. Combined, these beams correspond to an average Rabi frequency of $\sim 40\ \gamma \approx 2\pi \times 6$ MHz. With a Rabi frequency in this range, the 1088 nm frequency is swept from -250
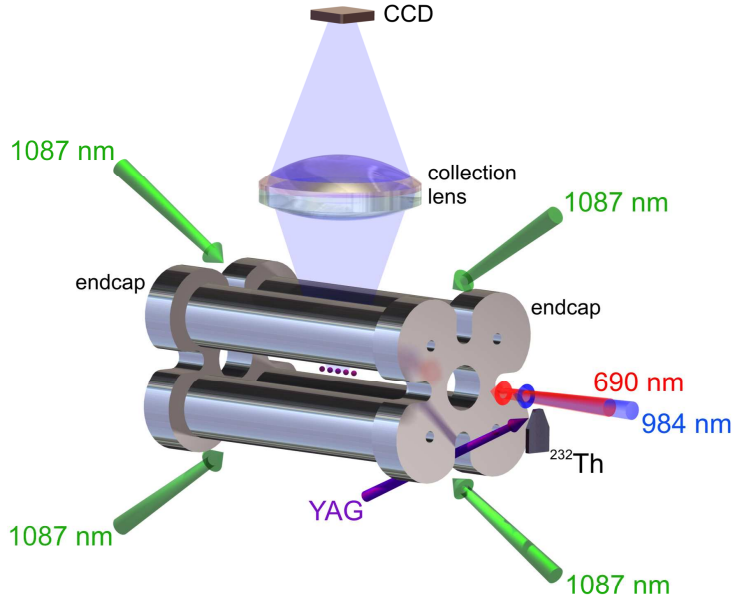
Figure 24: Experimental setup using the cloverleaf trap.

MHz to -25 MHz in ∼ 15 s. This process substantially reduces the ion sample temperature. With a reduced Doppler width, the low-power Λ-system beams (Λ-beams) interact more efficiently with the ions and continue to cool them to crystallization. Each of the Λ-beams is of diameter 1 mm and power corresponding to an average Rabi frequency of ∼ 1 MHz. The 690 nm field is resonant and the 984 nm field is detuned ∼ 1 MHz to the red of resonance. The axial beams are not retro-reflected in this configuration due to increased scatter into the imaging system. An applied magnetic field of ∼ 1 G is used to destabilize dark states.
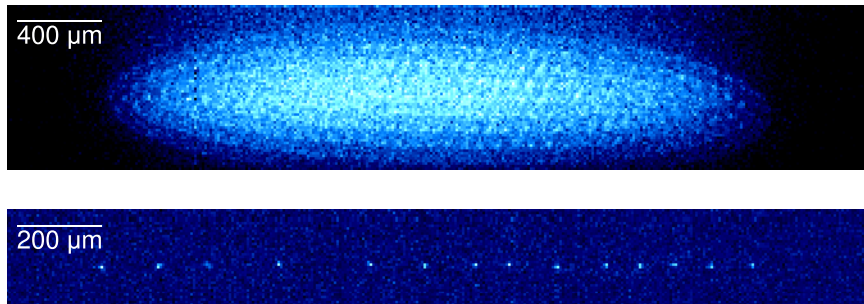
Figure 25: First observed Th^{3+} crystals (cloverleaf trap). The top image is a crystallized sample of ∼1700 ions while the bottom image is a linear chain of 14 ions. The integration time for each image is 6 s.

Figure 25 shows examples of some of the first thorium crystals observed in the clover-leaf trap. It was found empirically that crystallization was most rapidly achieved and consistently held in this trap for $0.03 \lesssim q \lesssim 0.06$ and $0 \lesssim a \lesssim 0.001$. The lower limit of q is dictated by the negative value of Δa, deriving from the radial defocussing near trap center due to the positive dc endcap voltages. The small non-zero a is used to break the degeneracy of the radial trap frequencies. At the upper limit of q, three dimensional crystals are observed to critically heat and rapidly dissipate for $q \gtrsim 0.07$ while for linear chains this occurs at $q \gtrsim 0.15$. This increased maximum q is due to the fact that ions of a linear chain all have only small displacements from the rf minimum, and therefore reduced rf heating.

Laser cooling ^{232}Th^{3+} is also done in the extended trap with a very similar optical and imaging setup (Figure 26). Here, the 1088 nm beams are circular in cross-section with 2 mm diameters, are oriented at 45° angles to the trap axis, and each contain 20 mW of power. Both pairs of counter-propagating beams consist of counter-propagating orthogonal linear polarizations. After the loading and purification protocols are performed, the 1088 nm laser cools the sample in $\sim$ 15 s while maintaining a fixed detuning in the range -100 MHz to -50 MHz. At this point, the axial 690 nm and 984 nm beams cool the ions to crystallization. The Λ-beams have 2 mm diameters and powers which broaden the transitions to 1-2 MHz. They both have fixed detunings of 1-2 MHz below resonance. The fields are retroreflected with orthogonal linear polarizations, similar to that done for the 1088 nm fields.

The laser cooling process from ablation to crystallization without the aid of buffer gas is shown in Figure 27. The extended trap is driven at 8.2 MHz with tube biases of 8.0 V. With V_0 = 1.2 kV, U_{ec} = 0 V, and δ_{1088} = -70 MHz, a single YAG pulse ablates thorium from the ^{232}Th metal target. After a delay of 10.0 μs, U_{ec} is ramped in 130 ns to 250 V, blocking most of the ions moving slower than Th^{3+} from entering the trap. A $\sim$ 1 V, 550 kHz ac signal is then applied to one trap rod while V_0 is ramped down to 100 V in 8 s. This process resonantly ejects all lighter pollutant ions from the trap, leaving a pure Th^{3+} sample. V_0 = 100 V is empirically found to be low enough so that 1088 nm laser cooling
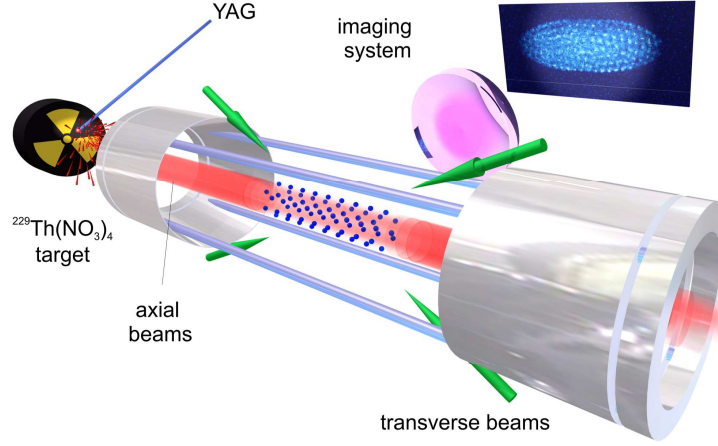
Figure 26: Experimental setup using the extended trap.

removes kinetic energy faster than rf heating introduces it. The ions are then cooled until γ_D is roughly limited by δ_{1088}. The axial Λ-beams then cool the sample into the ultra-cold regime, creating a pseudo-liquid phase. After ambient dc offsets are compensated to minimize rf heating, a full crystal forms and the 1088 nm field is detuned to - 200 MHz, increasing 984 nm scatter and cooling. The far-detuned 1088 nm laser serves to re-cool ions which are rapidly heated by collisions with background molecules.

The most useful crystal configuration to be demonstrated in this work is that of the linear chain. To create such a crystal, the trap frequency $\omega_z \ll \omega_{x,y}$, allowing the ions to lie purely along the rf potential minimum. This placement minimizes rf heating while maximizing ion localization and position control. Figure 28 shows ions in this configuration produced in the extended trap. The axial trap frequency is reduced here to $\sim$ 15 kHz by lowering U_{tb} to 3 V. The suppressed rf heating in the chains relative to 3-dimensional crystals is deduced from the $\sim 3\times$ increase in the maximum q at which the crystals are stable.

With sufficient control in producing, loading, purifying, and laser cooling from the ^{232}Th metal source, a transition is made to performing the same tasks with ^{232}Th^{3+} from the nitrate source. This transition is relatively straight forward if one keeps in mind the change in ablation source bulk composition and its possible impact on ion loading. Specifically, the
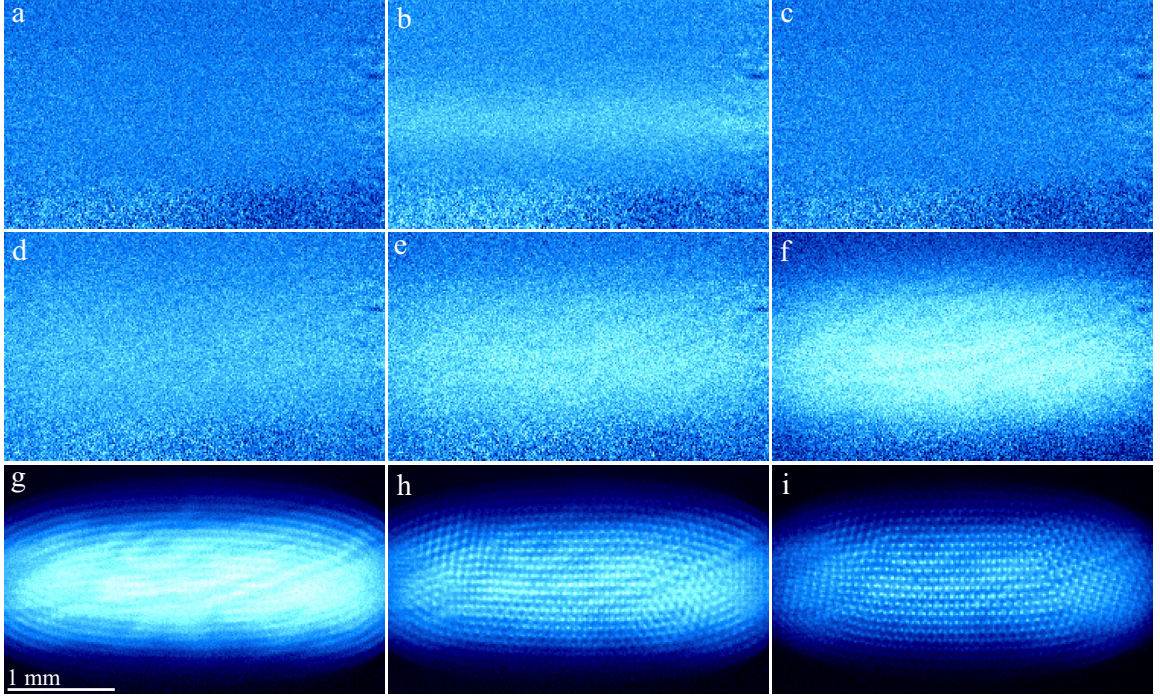
Figure 27: Laser cooling process of ^{232}Th^{3+}. a) t = 0 s. An image immediately before ion ablation. b) t = 4 s. A hot, polluted cloud immediately after ion loading. c) t = 7 s. As V_0 is lowered for micromotion reduction and sample purification, decreased trap frequencies allow the cloud to spread, becoming too dim and diffuse to detect. d) t = 10 s. As V_0 is reduced so that laser cooling overcomes rf heating, the cloud begins to cool with increasing fluorescence. e) t = 13 s. The 1088 nm fields further cool the ions. f) t = 16 s. The 1088 nm fields further cooling the sample, reducing the Doppler width and increasing the efficiency of the Λ-beam interactions with the ions. g) t = 19 s. The ions are efficiently cooled by the Λ-beams, inducing a transition into the pseudo-liquid phase. Here the temperature limit is dictated by excess rf heating. h) t = 25 s. After compensation of ambient electric fields, a complete crystal is formed from ~ 16,000 ions. i) t = 120 s. The 1088 nm laser detuning is - 200 MHz for increased 984 nm fluorescence and cooling. The integration time for each image is 3 s.
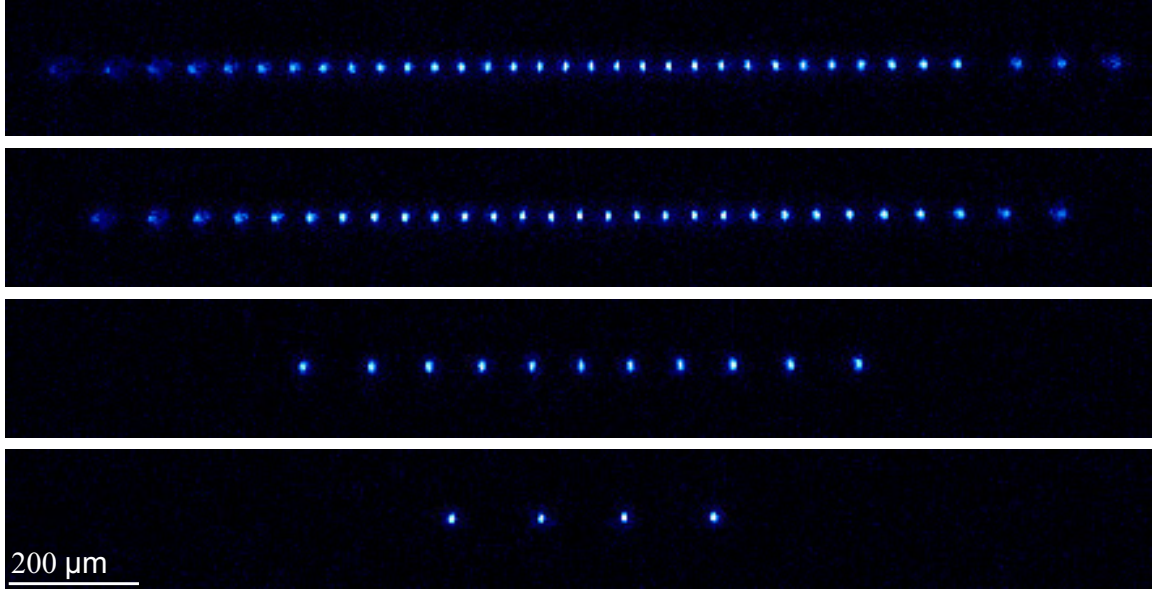
Figure 28: Linear ion chains of ^{232}Th^{3+} in the extended trap driven at 8.5 MHz. The ions near the left and right edges of the frames lie outside of the imaging system field of view, which appears to be $\sim 900\,\mu$m. Ions in this configuration survive in the extended trap for a large fraction of an hour. The integration time for each image is 3 s.

bulk material m/Q should be much smaller than that of Th^{3+} and should be of high purity due to the relatively low yield of triple ionization during the ablation process. Additionally, it is observed that the bulk m/Q must be strictly unstable during loading ($q_{bulk} > 0.908$) to observe Th^{3+} loading. Due to rf voltage limitations, the extended trap is run at $2\pi\times$ 4.3 MHz to fulfill this requirement for the aluminum substrate of the thorium nitrate samples. Figure 29 shows a sample crystal using the nitrate source and reduced drive frequency. In order to increase the drive frequency in future work, one may reduce the trap radius, increasing q for a given V_0. One may also change to a substrate metal which is lighter than aluminum, perhaps a high-purity lithium foil ($m/Q = 7$ amu/e, 3.5 amu/e, 2.33 amu/e, etc.). With realization of ^{232}Th^{3+} crystals produced from the thorium nitrate source, a transition to laser spectroscopy and cooling of ^{229}Th^{3+} is made.
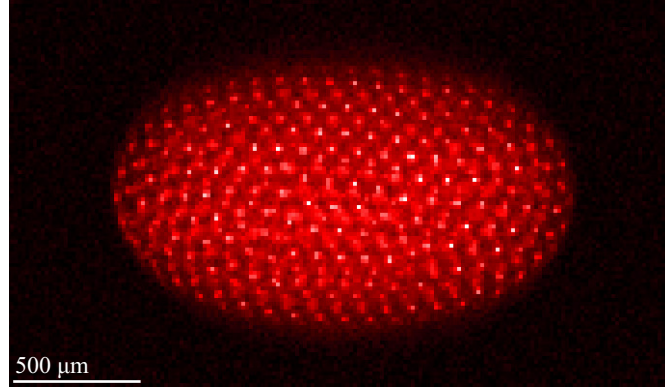
Figure 29: Prolate ellipsoidal ion crystal created in the extended trap from the ^{232}Th(NO$_3$)$_4$ source. The integration time is 2 s.

3.3   Laser Cooling Trapped ^{229}Th^{3+}

Laser cooling the 229 isotope of thorium requires a more complicated optical setup than does the 232 isotope. The deformation of the nucleus from spherical symmetry creates higher order multipole moments which interact with the valence electron. This interaction induces splitting of the fine structure levels into either $(2I + 1)$ or $(2J + 1)$ hyperfine levels with splittings on the 100 MHz scale. Multiple optical transitions must therefore be accessed with the laser light in order to avoid creating dark states. One must also ensure that a frequency component which is red-detuned and cooling on one transition is not blue-detuned and inducing strong Doppler heating on another transition.

To relax the requirement of having multiple finely tuned optical frequencies for low-temperature cooling, and to ensure significant unwanted heating does not occur due to inadvertent blue detuning, the closed $|5F_{5/2}, F = 0\rangle$, $|6D_{5/2}, F = 1\rangle$, $|5F_{7/2}, F = 0\rangle$ Λ-system is utilized (Figure 30). This system is closed due to angular momentum selection rules which forbid decay from the $|6D_{5/2}, F = 1\rangle$ level to levels other than $|6D_{5/2}, F = 1\rangle$ and $|5F_{7/2}, F = 0\rangle$. Utilization of this system allows for most of the 1088 nm and 984 nm fields to be only weakly interacting with the ions. These fields occasionally repump ions that are lost from the closed Λ-system due to off-resonant excitation to the $|6D_{5/2}, F = 1\rangle$ level. Consequently, the intensities and detuning of these fields are not critical.

To laser cool from high temperatures and pump ions into the closed Λ-system at low temperatures, the 1088 nm fields are detuned 20 - 80 MHz below relevant transition frequencies. The variation in detunings avoids inadvertent heating on nearby red-detuned transitions. While the ions are at sufficiently high temperatures to require 1088 nm cooling, Doppler broadening conveniently suppresses interaction of the 690 nm field with the ions. With this suppression, ions continue to interact with and be cooled by the 1088 nm fields. When cooled enough such that 690 nm interactions are significant, the ions are pumped to the Λ-system where they are cooled to crystallization.
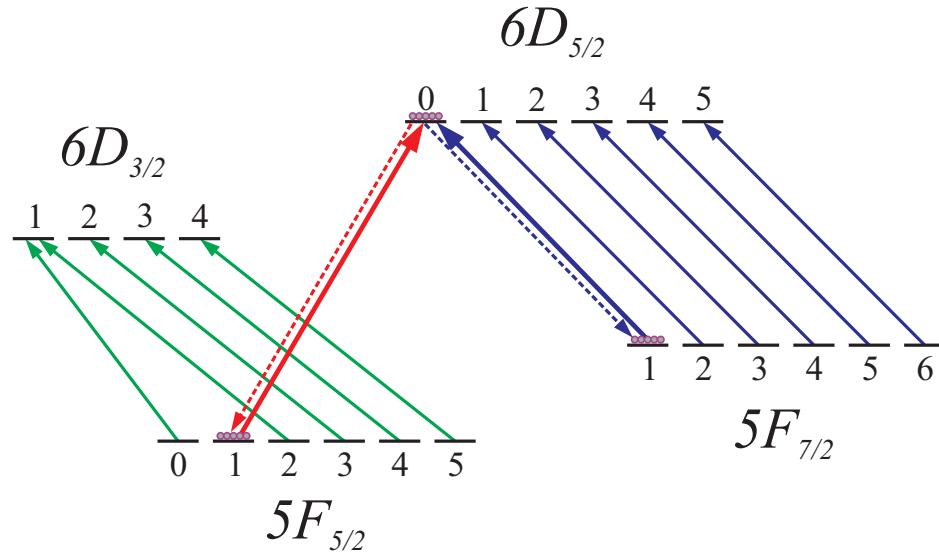
Figure 30: The four lowest-lying fine structure levels of ^{229}Th^{3+} including hyperfine structure. The cooling scheme utilizes the closed Λ-system indicated with bold arrows.

Because the ^{229}Th source is composed of 76% ^{229}Th and 24% ^{232}Th, the 232 isotope is also cooled during this process. The various optical fields for both isotopes are produced via phase modulation of the laser carriers while a separate unmodulated laser is used for the ^{232}Th 1088 nm transition. This additional laser provides increased optical power for high-temperature cooling. An example spectrum of the 984 nm light is shown in Figure 31. Similar signals are obtained for all wavelengths by directing a small fraction of the modulated laser light through a 19 GHz free spectral range optical cavity where the cavity length is scanned with a ring PZT (see Section 3.4 for details). The light is then spatially filtered

by injecting it into a single mode fiber where only the TEM00 spatial mode is transmitted to a photodetector. The individual spectral components used for each isotope are identified.

^{229}Th^{3+} ^{232}Th^{3+}

— 984 nm Cavity PZT Voltage   13 GHz Span
— 984 nm Cavity Transmission
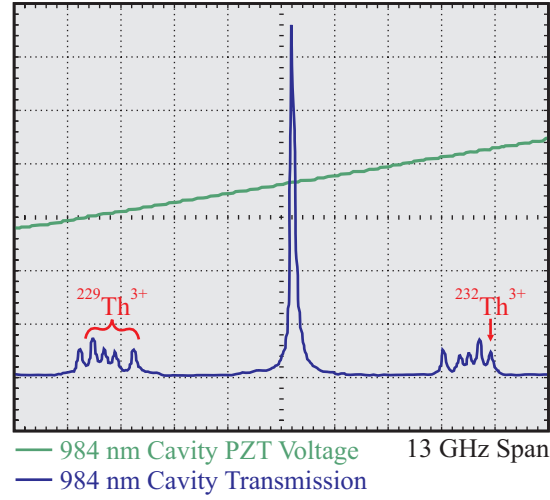
Figure 31: Spectral analysis cavity signal for the 984 nm laser cooling spectrum. Each spectral component contains 3-5% of the total optical power. The cavity free spectral range is 19 GHz.

The beam orientations, polarizations, and cross-sectional sizes for dual-isotope cooling are the same as those for ^{232}Th^{3+} cooling. Because the Λ-system transitions require only small spectral densities, each relevant ^{229}Th^{3+} transition is easily power broadened to 1-2 MHz, similar to that done for the ^{232}Th^{3+} case. With optical injection losses at the fiber-based phase modulators and distribution of optical power among various sidebands, the individual 1088 nm spectral components exciting the 229 isotope contain only 1 mW of power per beam, as opposed to 20 mW per beam for the 232 isotope.

Fluorescence at 984 nm and low-temperature cooling are modulated for each isotope by varying the power in the two 690 nm modulation frequencies. By removing one frequency, the 690 nm light no longer repopulates the $5F_{7/2}$ level for a given isotope and eliminates 984 nm fluorescence. Figure 32 shows such figures with the 690 nm fields modulated for each isotope. Sympathetic cooling is evident as the dark ions maintain an ultra-cold phase when direct low-temperature laser cooling is removed. The thorium source purity is reflected in the ratio of ^{229}Th to ^{232}Th ions within the crystals.
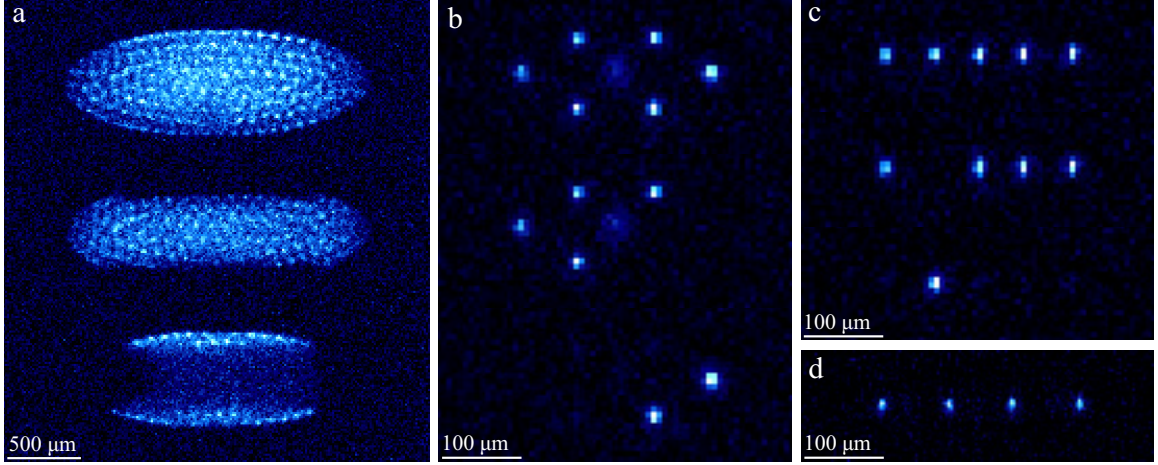
Figure 32: Trapped ^{229}Th^{3+} and ^{232}Th^{3+} ions, laser cooled to crystallization. (a) Three successive images were taken of about 200 crystallized Th^{3+} ions. The top image was taken with both ^{229}Th and ^{232}Th 690 nm fields present. The ^{232}Th 690 nm field was then removed for the middle image. The ^{232}Th 690 nm field was then reintroduced and the ^{229}Th 690 nm field simultaneously removed for the bottom image. The larger mass-to-charge ratio of ^{232}Th^{3+} causes its radial accumulation in the outer shells of the crystal. The short focal depth of the imaging system is apparent as most of the ^{232}Th^{3+} shell is out of focus. The integration time is 1 s for all three images. (b), (c) The same imaging protocol used in (a) is used on smaller samples. The integration time is 2 s for all images. (d) A linear chain of four ^{229}Th^{3+} ions is shown. The integration time is 3 s. The scale bar in (a) is 500 μm and in (b)-(d) are 100 μm.

With the realization of ultra cold ^{229}Th, an efficient search protocol may be employed to locate and populate the nuclear isomer level.

3.4   Laser and Imaging Systems

3.4.1   Laser Systems

The task of the lasers in this work is to address the low-lying electric dipole transitions in ^{232}Th^{3+} and ^{229}Th^{3+}. These transitions have natural widths of only a couple hundred kilohertz and the hyperfine splittings in the 229 isotope require multiple optical frequencies at each wavelength. The laser light must then be stabilized at a level that is better than commonly needed for Doppler cooling, yet, no convenient atomic references exist near the relevant wavelengths. Stabilization is done using an optical transfer cavity and a 780 nm laser which is frequency stabilized to an atomic transition in ^{87}Rb. The optical cavity is

length stabilized to the 780 nm field and the thorium lasers are then locked to this stabilized and periodic frequency reference. Multiple frequency components are produced from the stabilized carriers via 10 GHz bandwidth fiber-based electro-optic phase modulators.

To understand sufficiently the workings of this laser stabilization technique, a few important optical cavity relations are presented [33]. Here, we assume a TEM00 laser mode aligned with an optical cavity made with high-reflectivity concave dielectric mirrors. Transmission of the laser light through the cavity is maximized when the laser frequency $\nu = m \, FSR$ where m is an integer of order 10^6, $FSR = \dfrac{n \, c}{2 \, l}$ is the cavity free spectral range, n is the intracavity refractive index, c is the speed of light, and l is the cavity length. The optical transmission lineshape in this case is Lorentzian with full-width at half-maximum γ_c which is related to the free spectral range by the cavity finesse $\mathcal{F} = \dfrac{FSR}{\gamma_c}$. The finesse is dependent upon the round trip optical losses of the cavity and increases with increased mirror reflectivity. From these relations, it is clear that if the cavity length and intracavity refractive index are fixed, a sufficiently high finesse leads to a comb of narrow, stable transmission peaks with periodicity FSR in frequency space. These peaks may be used as lock points for a laser, effectively transferring the stability of the cavity length into stability of the laser frequency.

With a well stabilized laser carrier, rf sidebands are introduced to distribute the laser spectral density to other regions. By modulating the phase of the light such that

$$\cos\left[\omega_l t + \phi_l\right] \rightarrow \cos\left[\omega_l t + \phi_l(t)\right] = \cos\left[\omega_l t + \beta \sin\left(\omega_{rf} t\right)\right], \tag{51}$$

components of the laser power are placed at $\omega_l \pm \omega_{rf}$, $\omega_l \pm 2\omega_{rf}$, $\omega_l \pm 3\omega_{rf}$, etc. Here, β is the maximum angular phase shift and is known as the modulation index. The fraction of laser power in each of the $\pm i^{th}$ sidebands is $\left[J_i(\beta)\right]^2$, where $J_i(x)$ is the ith order Bessel function of the first kind. Figure 33 shows the effect on the spectral distribution of coherent light due to phase modulation. Here, the modulation frequency is 10γ with various values of the modulation index. This effect is used to distribute optical power throughout the spectrum with a single or multiple rf frequencies.
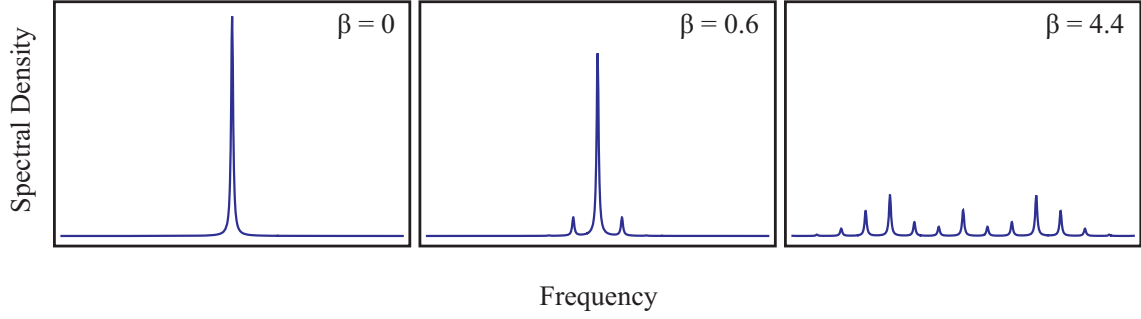
Figure 33: Illustration of spectral modification from phase modulation. This type of modification is utilized to engineer spectra for laser cooling and spectroscopy.

The lasers used in this work are all home built extended cavity diode lasers operating in the Littrow configuration. The laser diode mount is thermally stabilized and mounted on an independently thermally stabilized aluminum block. A diecast aluminum cover placed over the laser and wrapped in insulation tape reduces acoustic and thermal fluctuations at the laser diode. The lasers are all driven with home built low-noise current sources which follow the design of [34]. A PZT is used for fine adjustment of the feedback grating angle while gross adjustment is done with the high pitch screws of the laser diode mount.

The laser locking system is based on standard proportional and integral feedback loops with return routes being the laser current and diffraction grating PZT voltage. The laser light is modulated at 10 MHz ($\beta \approx 0.6$) with a free-space phase modulator for this purpose and is detected with a 10 MHz bandwidth photodetector. The total feedback bandwidth is estimated to be a few hundred kHz.

To reduce the work load of the active feedback system, the laser housing is designed to minimize frequency perturbations from acoustics. The 690 nm, 984 nm, and 1088 nm lasers are all mounted on a common breadboard which floats on vibrational absorption pads on an optical table. This mechanically and electrically decouples the laser systems from the optical table. The breadboard is covered with an acoustic isolation box which itself sits on the optical table to avoid mechanical coupling between the box and breadboard. The box is constructed from 1/8" thick aluminum plating which is covered inside and out with acoustic suppression foam. Laser light is transmitted from the box in single-mode

optical fibers. The 780 nm laser and the transfer cavity sit in a separate, nearly identical breadboard/acoustic isolation box structure.

A fraction of the light from the 780 nm laser is transfered to the thorium laser box via a single mode fibers. This field is combined with light from the three thorium lasers via dichroic mirrors. This collection of light is transfered to the reference cavity box via a single mode fiber. There, the multicolor beam passes through the free-space phase modulator where each color acquires rf sidebands at 10 MHz ($\beta \approx 0.6$) for locking to the transfer cavity. The laser light is then aligned with the transfer cavity. Transmitted light is split via dichroic mirrors and directed to photodetectors dedicated to individual wavelengths. Bandpass filters are placed in front of the detectors to further suppress pollution of unwanted laser light. In total, $\lesssim 10^{-7}$ fractional transmittance of other wavelengths produces unobservable cross-talk of locking signals in this setup.

The 780 nm light which is not used for cavity locking is used for locking the laser to an atomic transition in ^{87}Rb via saturated absorption spectroscopy in a Rb vapor cell. With the 780 nm light stabilized, an integral feedback loop monitoring the transmission of 780 nm light through the cavity corrects for cavity length changes by varying the cavity PZT voltage. Due to the nature of optical cavity construction and the acoustic isolation of this cavity from environmental perturbations, mechanical and electrical noise are observed to be sufficiently small for this work. Thermal drifts are the dominant source of fluctuations which need to be locked out. For this reason, the bandwidth of the feedback loop is ~ 0.5 Hz, producing an averaging effect of 780 nm laser noise while still correcting for cavity length drift on time scales greater than a couple seconds. An estimate of the fractional instability of the cavity FSR in this case is

$$\frac{\delta FSR}{FSR} \approx \frac{\gamma_c}{\nu} \times 1\% = \frac{FSR}{\mathcal{F}\nu} \times 1\% = \frac{527\,\mathrm{MHz}}{250 \times 384\,\mathrm{THz}} \times 1\% \approx 5 \times 10^{-11}$$

where it is estimated that the location of the m_0^{th} 780 nm fringe in frequency space is stabilized to 1% of γ_c. This stability transfers directly to the fractional instability of the lock points for all wavelengths. The result corresponds to tens of kHz in absolute frequency,

which is much less than the transition linewidths of interest in Th^{3+}. It should be noted that even with access to precise knowledge of the cavity length for the 780 nm light, extraction of the absolute frequencies of other lasers locked to the cavity is inaccessible due to the significant and unknown change in cavity length vs. optical wavelength. This comes from the nature of the multiple dielectric layers composing the cavity mirrors. This dispersion may in principle be measured but is not of sufficient relevance for the work done here.

A critical step in ensuring repeatable frequency stability of the lasers which are stabilized to the cavity is consistent fringe selection for locking. Identification of the correct locking fringe for the thorium lasers is done using a wavemeter of accuracy ~ 60 MHz. This is much smaller than the cavity FSR, hence fringe identification is unambiguous. The more challenging fringe selection process is that performed when locking the cavity to the 780 nm field. If, for instance, the mode number $m_0 + \Delta m$ is selected for cavity stabilization as opposed to m_0, the resulting frequency shift of a locked laser due to this error is

$$\delta \nu = \Delta m \, FSR \left(\frac{\lambda - 780 \, \text{nm}}{\lambda} \right) \tag{52}$$

where λ is the wavelength of the locked laser. For the thorium lasers, $\Delta m = \pm 1$ corresponds to shifts up to ± 150 MHz. This level of error is clearly intolerable and time consuming to identify when using only the wavemeter. To circumvent this problem, a different approach is employed.

In order to consistently select the m_0^{th} 780 nm fringe for cavity stabilization, a second absolute frequency reference at 795 nm is used. A 795 nm diode laser configured for saturated absorption spectroscopy in a Rb cell is also coupled to the transfer cavity via the same optical fiber carrying the multicolor field. As the frequency of this laser is scanned, transmission signals through the transfer cavity and Rb vapor cell are simultaneously monitored on an oscilloscope. A convenient D1 transition in ^{87}Rb is chosen as the reference peak ($5S_{1/2}, F = 1 \leftrightarrow 5P_{1/2}, F = 2$ in this case) and an AOM shifts the relative position of the cavity peak and reference peak such that they are aligned. The AOM frequency is then fixed and this peak alignment serves and an indicator of proper cavity locking. From

Equation (52), the relative shift in peak alignment for $\Delta m = \pm 1$ is ± 9.9 MHz, an easily observable effect.

Figure 34 shows an example signal using this technique. The left panel illustrates cavity locking to the target fringe while the right panel illustrates locking with $\Delta m = 1$. The 9.9 MHz shift is clearly observable between the 4 MHz wide cavity signal and the 15 MHz wide atomic signal. Oscilloscope averaging is the cause for peak broadening here and is used here due to acoustic fluctuations on the 795 nm light.

a)   b)

— ^{87}Rb $5S_{1/2}$ F=1 $\leftrightarrow$ $5P_{1/2}$ F=2 Doppler-Free Absorption Peak
— 795 nm Transfer Cavity Transmission
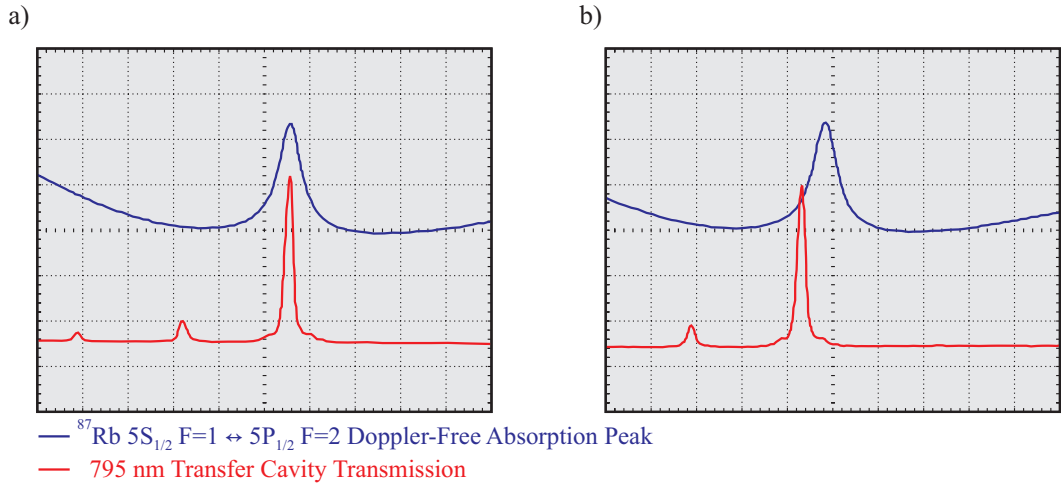
Figure 34: Transmission signals of 795 nm light through a Rb vapor cell and transfer cavity. The relative offset of the peaks indicates an error in cavity locking.

The transfer cavity itself is composed of a pair of concave broadband dielectric mirrors with 50 mm radius of curvature. The mirrors are separated with a 1" diameter ring PZT in series with a 1" diameter, 10.7" long Super Invar rod containing a 1/4" hold drilled coaxially through for optical transmission. The cavity sits on a pair of 1/2" × 1" footprint teflon spacers in a vacuum chamber of pressure $10^{-5} - 10^{-1}$ Torr. The rough vacuum environment is critical for transfer cavity applications in this work. Laser stabilization using a system at atmosphere produces frequency shifts of stabilized lasers on the order of 10 MHz in a 24 hr period. Changes in humidity, barometric pressure, and temperature induce different refractive index shifts for different wavelengths, causing relative changes in the cavity FSR across the optical spectrum. The size of these effects is proportional

to the intracavity pressure, hence, a reduction in pressure from 760 Torr (1 atm) to 10^{-1} Torr is sufficient to suppress these shifts to a negligible level. The cavity vacuum chamber temperature fluctuations are stabilized to $\lesssim 1°$ C, relaxing the need for a large voltage range on the cavity PZT to compensate for thermal expansion/contraction.

Laser stability using this system produces long-term frequency drifts of <100 kHz/-month and short term laser linewidths of $\lesssim 200$ kHz. The laser linewidths are estimated using an independent passively stabilized optical cavity to monitor frequency fluctuations. By tuning the laser frequency to the slope of a stable cavity transmission peak, frequency noise is translated into amplitude noise, an effect easily observed with a sufficiently high bandwidth photodetector. This treatment assumes negligible laser amplitude fluctuations and detector noise, sufficiently accurate approximations for the estimates here. The photodetector voltage corresponding to optical cavity transmission may be written as

$$V(\delta_c) = V_{max} \frac{\gamma_c^2}{\gamma_c^2 + 4\,\delta_c^2} \tag{53}$$

where V_{max} is the peak voltage corresponding to maximum optical transmission and δ_c is the laser detuning from maximum transmission. It is convenient and most accurate to monitor laser frequency noise when $\mathrm{d}^2 V/\mathrm{d}\delta_c^2 = 0$. This occurs at a detuning of $\delta_c = \pm\gamma_c/(2\sqrt{3})$ and voltage $V = \dfrac{3V_{max}}{4}$. At this detuning,

$$\frac{\mathrm{d}V}{\mathrm{d}\delta_c} = \frac{3\sqrt{3}V_{max}}{4\,\gamma_c}, \tag{54}$$

leading to an expression estimating the laser linewidth γ_l to be

$$\gamma_l \sim \frac{V_{pkpk}}{\mathrm{d}V/\mathrm{d}\delta_c} = \frac{4V_{pkpk}\,\gamma_c}{3\sqrt{3}V_{max}} \approx 0.77\frac{V_{pkpk}\,\gamma_c}{V_{max}} \tag{55}$$

where V_{pkpk} is the small peak-to-peak voltage fluctuation on top of the $\dfrac{3V_{max}}{4}$ dc offset. For Equation (55) to produce meaningful results, the detector bandwidth should be larger than γ_l and γ_l should be roughly no larger than $\gamma_c/4$.

To carry out this estimate, the stabilized light to be measured is passed through a phase modulator which generates single-frequency rf sidebands from 100 MHz - 1 GHz ($\beta \approx 1.5$).

This modulated light is coupled to the second cavity and an rf sideband tuned such that it is located on the slope of a transmission peak. This spectral component of the light is assumed to contain the same frequency and amplitude fluctuations as the carrier. With knowledge of γ_c from the finesse and measured FSR of the second cavity, small fluctuations in the otherwise dc signal are integrated for a few seconds and translated via Equation (55) into an estimate for γ_l.

This method, of course, depends on knowledge of the cavity FSR and finesse for each wavelength. The FSR of a given cavity is easily measured to parts in 10^5 with laser light which is significantly phase modulated such that the fraction of power remaining in the carrier is $\ll 1$ ($\beta \gtrsim 2$). With the small carrier tuned to a cavity transmission peak, the phase modulation frequency is scanned. When this frequency is equal to the cavity FSR, all sidebands are spectrally aligned with nearby cavity modes and are, therefore, transmitted, leading to a clear increase in photodetector signal. If the modulation frequency is tuned to some larger integer number of FSR's, the measurement uncertainty is reduced by the inverse of this integer. For example, the transfer cavity FSR was measured using a modulation frequency of 2.6 GHz for both 690 nm and 984 nm light, resulting in $FSR_{690} = 526.951(3)$ MHz and $FSR_{984} = 526.927(3)$ MHz. The discrepancy here is attributed to the increased penetration depth of the 984 nm light with respect to 690 nm light when reflecting from the cavity mirrors. This effect translates to an increase in cavity length of 13 μm.

The cavities used in this work are all constructed using mirrors from a common custom set, thus they are assumed to be identical. The round trip optical losses of the cavities are assumed to come almost completely from the mirrors whether one is using a vacuum or atmosphere intracavity medium. For this reason, the finesse at a given wavelength is assumed to be constant from cavity to cavity. The finesse is estimated here by comparing γ_c of the transfer cavity to the 10 MHz rf sideband spacing introduces for locking. With knowledge of the cavity FSR and an estimate for γ_c, the finesse is easily obtained. Results are shown in Table 1. Note that relative to the mirror properties at 690 nm, the lower finesse

and reflectivity at 984 nm is consistent with the observed increase in reflection penetration depth, a general property of dielectric mirrors.

Table 1: Measured finesse of the transfer cavity at all locking wavelengths. The estimated uncertainty is 10% for all results.

Wavelength (nm)	Finesse
690	290
780	250
984	150
1088	90

3.4.2   Imaging System

Imaging of trapped Th^{3+} poses significant, but surmountable, challenges. Low noise silicon detectors are efficient at 690 nm with quantum efficiencies $> 90\%$, but the 690 nm transition has an effective linewidth of $2\pi \times 28$ kHz due to the $\approx 88\%$ decay on the 984 nm transition. The 984 nm transition has an effective linewidth of $2\pi \times 210$ kHz, but the quantum efficiency of silicon detectors drops to $\sim 20\%$. The 1088 nm transition has a linewidth of $2\pi \times 146$ kHz, but silicon's quantum efficiency here is $\lesssim 1\%$. Other detector materials with high efficiency at 1088 nm are found to be too noisy.

Compared to conventionally laser-cooled ions with linewidths of > 10 MHz, these are all challenging options. However, the best option is to image ions on the 984 nm transition. Imaging was first done in the hyperbolic trap (Figure 35) using an AndOr iDus 401 Series spectroscopic camera. Fluorescence is collected and collimated with a 2" diameter 75 mm focal length achromat. A 2" diameter 150 mm focal length achromat focuses the collimated light onto the camera CCD. This system produces a 2× image magnification for the 26 μm × 26 μm camera pixels. The ~100 μm ion separation in ion crystals is easily observable. A 5 nm bandpass filter at 984 nm sits immediately in from of the CCD to suppress room light and laser light scatter of other wavelengths, particularly that from the high-power 1088 nm fields. This setup was used for all imaging in the hyperbolic and cloverleaf traps.

With the extended trap, a transition was made to an AndOr iKon-M 934 Series imaging camera with improved noise characteristics and faster image readout rates. Fluorescence collection for the iKon camera is done with a 2" diameter 40 mm focal length (NA = 0.55) aspherical lens. A 2" diameter 150 mm focal length achromat focuses the light onto the camera CCD. The large-diameter ashere is designed for diffraction limited performance at 780 nm. This system produces a 2.75× image magnification for the 13 μm × 13 μm camera pixel size. A 5 nm bandpass filter at 984 nm also sits immediately in front of the iKon CCD. Fluorescence collection efficiency for the iKon setup is about 7%.

CHAPTER IV

THORIUM IV ATOMIC LASER SPECTROSCOPY

4.1 Laser Spectroscopy of $^{232}Th^{3+}$

Because the uncertainties of the optical transition frequencies of interest prior to this work were much larger than that required for laser cooling, precision spectroscopy of the transitions was performed [22]. The first stage of this process involves spectroscopy of a thermal cloud of ions cooled by helium buffer gas. In a collaborative effort where gross frequency searches were performed in two separate traps, fluorescence from laser excitation to the $6D_{5/2}$ level was observed in [35] and fluorescent signals from laser excitation to the $6D_{3/2}$ level was observed in the hyperbolic trap. These results reduced the transition frequency uncertainties to much less than the Doppler widths. An image of buffer-gas cooled ions obtained early in this work is shown in Figure 35. The cloud extends well beyond the fluorescing regions with the fluorescence cutoff due to misalignment of the axial fluorescence beams. The storage time of such clouds was ~ 5 s.

1 mm
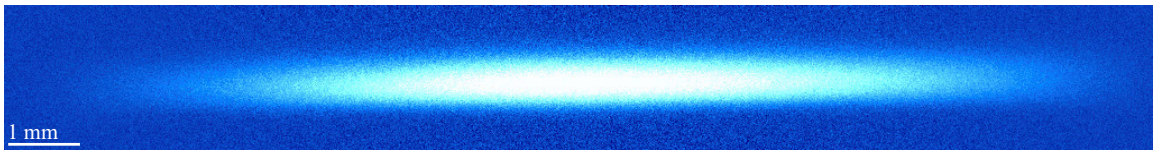
Figure 35: Image of a buffer gas cooled cloud of $^{232}\text{Th}^{3+}$ in the hyperbolic trap.

During higher resolution spectroscopic work, buffer gas cooled Th^{3+} storage times were ~ 10 s. The camera used for fluorescence detection requires ~ 1 s for signal integration and image readout. To scan an absorption profile with sufficient resolution using this detection method would take longer than the ion storage time. This method would, therefore, introduce significant unwanted systematic skewing of the data. To remove this effect, a high bandwidth single photon counter was employed for fluorescence detection. By scanning a

probe laser frequency across the transition with a period much shorter than the ion storage time and much longer than the excited state lifetime of the ions, one may average many scans and avoid systematic shifts in the data due to signal decay. This method also allows one to average over many different ion sample sizes, all with different signal strengths.

Coupling of ion fluorescence to the single photon counter is done by collecting ion fluorescence with a 1" diameter 7 mm focal length lens and directing it through a bandpass filter and into a 63 μm core multimode fiber. The fiber is coupled directly to the photon counter. The probe laser frequency is scanned at ~ 10 Hz using the laser PZT and integration times are as high as several minutes. This scan rate is sufficiently slow that the wavemeter can continuously track the saw-tooth waveform of the probe laser frequency. This allows for continuous gross monitoring of the frequency scan range and graduate student feedback for central frequency stabilization. Scans are done for all three transitions using the same single photon counter for detection and integration times of up to several minutes. A representative data set is shown in Figure 36 for the 690 nm transition. The dominant contributions to uncertainty in this process come from drift of the laser frequency during fluorescence integration and the 20 MHz stated uncertainty of the wavemeter used for laser frequency determination. It should be noted that the laser frequency is assumed to depend linearly on the PZT voltage in this case, a dependence roughly observed with wavemeter signal output but an assumption not rigorously justified.

Once the transitions are located with precision similar to that shown in Figure 36, the lasers are stabilized to a transfer cavity, laser cooling is performed, and higher resolution spectroscopy is achieved. With linear rf traps operating in the weak binding limit, laser spectroscopy is most accurately done along the trap axis where the first-order Doppler shift is minimal. For this reason, probe fields are oriented along the trap axis in this work.

With cold samples of a few hundred ions lasting in the cloverleaf trap for several hundred seconds, efficient photon counting using the imaging camera is done. Signal decay rates are sufficiently slow that signal skewing is negligible. Figure 37 shows a scan of the

66
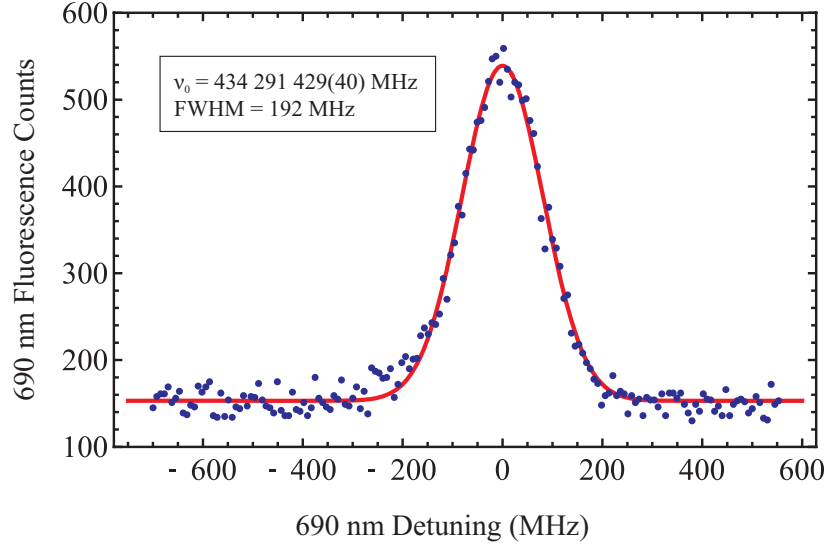
Figure 36: An optical scan of the 690 nm transition in a buffer-gas cooled sample of ^{232}Th^{3+}. 690 nm fluorescence is detected using a single photon counter while the laser frequency is scanned via the laser grating PZT. A Gaussian lineshape is fit to the data.
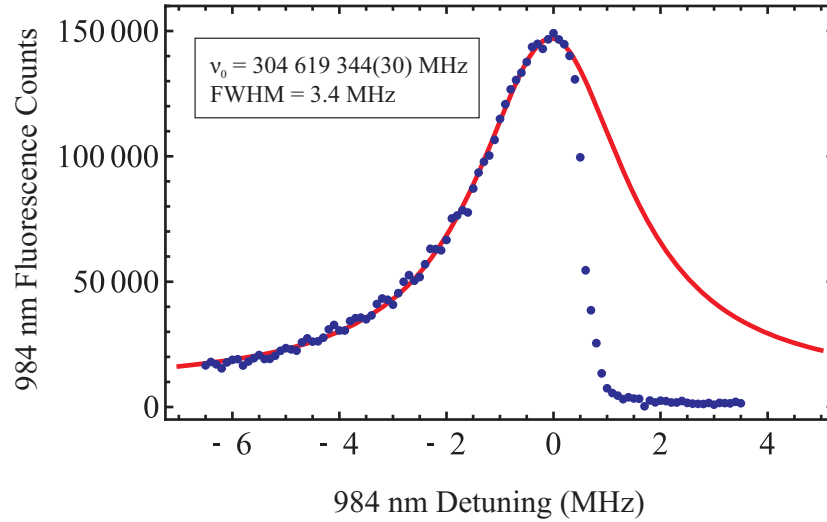
Figure 37: Background subtracted ion fluorescence rate vs. detuning of the 984 nm laser and Lorentzian fit to the red detuned region of the data. Back action from the probe laser is evident as heating occurs on the blue side of resonance. To step the 984 nm frequency, an acousto-optic modulator was used. Sinusoidal intensity oscillations with period ~460 kHz were present in the 984 nm beam, consistent with a $v/2l$ period expected from partial acoustic wave reflection inside the modulator crystal. Here, v is the acoustic wave velocity in the crystal and l is the length of the crystal transverse to the acoustic wave k vector.

984 nm cooling laser across resonance. Here, the 984 nm laser is locked to the transfer cavity and light is passed through an acousto-optic modulator for frequency shifting and

amplitude control. The acousto-optic modulator frequency steps are computer controlled and synchronized with camera integration and image readout. The 1088 nm beams maintain ultra-cold temperatures while the 984 nm field is off resonance. The 690 nm field is fixed on resonance for the duration of the scan. Power broadening is evident and heating of the ions is apparent on the blue side of resonance. When efficiently heated, increased Doppler broadening reduces the fluorescence signal induced by the weak 984 nm cooling beam. After minimizing rf heating, reducing the 1088 nm power broadening and detuning for more efficient low temperature cooling, and reducing the 984 nm power, a narrower feature is observed in Figure 38.
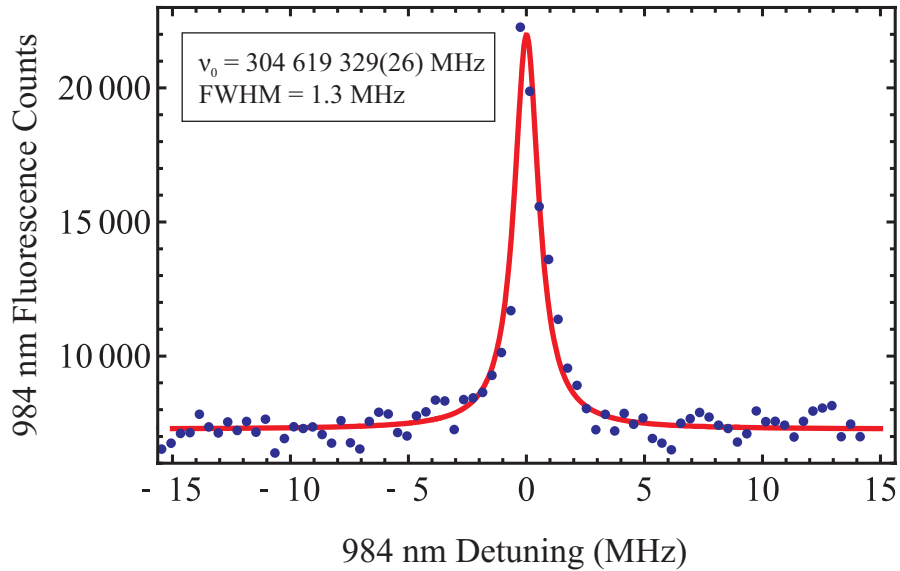
Figure 38: Optical scan of the 984 nm transition and Lorentzian fit using $\lesssim 50$ crystallized ions. Probe laser back action is suppressed with reduced probe power and increased low-temperature cool efficiency of the 1088 nm fields.

The protocol used to measure the 690 nm transition frequency relies on 984 nm fluorescence changes as the 690 nm field frequency is swept across resonance. When off resonance, ions are removed from the Λ-system and cycle only on the 1088 nm transition which is not detected. When resonant, cycling within the Λ-system occurs and fluorescence is detected, providing spectra similar to that of Figure 38.

Resonance on the 1088 nm transition is determined by inducing Doppler heating similar

to that observed in Figure 37. When the 1088 nm field frequency is slightly above resonance, the ions are strongly heated and the resultant Doppler broadening severely reduces 984 nm fluorescence induced by the weak Λ-system fields.

In averaging multiple scans over many days, a common 26 MHz uncertainty is achieved for all three transition frequencies. This uncertainty is composed of the 20 MHz wavemeter uncertainty added linearly [36] to a 6 MHz uncertainty composed of estimated errors introduced by short term wavemeter drift, laser cooling dynamics, Zeeman broadening and optical pumping, and light shifts. The transition frequencies are measured to be 434 291 397 (26) MHz for the $5F_{5/2} \leftrightarrow 6D_{5/2}$ transition, 304 619 344 (26) MHz for the $5F_{7/2} \leftrightarrow 6D_{5/2}$ transition, and 275 606 583 (26) MHz for the $5F_{5/2} \leftrightarrow 6D_{3/2}$ transition.

These results are a significant improvement on the best previous measurements of several hundred MHz precision. The dominant limitation in absolute frequency knowledge at this point comes from the wavemeter, though higher precision measurements are not required for efficient laser cooling and internal state manipulation of ^{232}Th^{3+}. Once locked to the transfer cavity, the thorium laser frequencies have long-term instabilities of < 100 kHz. Therefore, relative to the laser lock points, the atomic transition frequencies may be measured with precision less than the natural linewidths. Once the transitions are found using the values above, it is the absolute laser stability that is of practical importance when considering experimental applications at this level.

4.2 Hyperfine Structure and Isotope Shifts of ^{229}Th^{3+}

The most significant changes in the atomic structure of ^{229}Th^{3+} with respect to that of ^{232}Th^{3+} are due to the change in nuclear angular momentum I. In the case of the ^{232}Th nucleus, $I = 0$, whereas for ^{229}Th, $I = 5/2$. With non-zero angular momentum, the multipole expansion of the nuclear electric and magnetic potentials includes orders higher than $k = 0$, the monopole. Angular momentum selection rules limit the multipolarity, however, to $k \leq 2I$ while parity selection rules further limit the potentials to even-order electric and

odd-order magnetic multipole moments. These multipole moments interact with the orbiting electrons, introducing hyperfine structure splitting of the fine structure levels. These interactions are small compared to the fine structure interaction between the electron orbital and spin angular momenta and may be treated in perturbation theory.

The fine structure of an atomic energy spectrum is due to coupling between the electronic orbital angular momentum L and spin angular momentum S, producing total electronic angular momentum given by $J = L + S$. The coupling of this angular momentum to the total nuclear angular momentum leads to splitting of each fine structure level into a manifold of either $(2I + 1)$ or $(2J + 1)$ hyperfine levels with each new level having an atomic angular momentum of $F = I + J$, where $|J - I| \leq F \leq |J + I|$.

To first order in perturbation theory, the energy shift of these new levels within $^{229}\text{Th}^{3+}$ may be written as [37]

$$\Delta E_{hfs} = \frac{K}{2} A + \frac{\frac{3}{2} K(K + 1) - 2I(I + 1)J(J + 1)}{4I(2I - 1)J(2J - 1)} B \tag{56}$$

where $K = F(F + 1) - I(I + 1) - J(J + 1)$, A is the magnetic dipole hyperfine constant, and B is the electric quadrupole hyperfine constant. The A coefficient represents the interaction strength of the orbiting valence electron with the magnetic dipole moment of the nucleus and may be written as $A = \frac{\mu}{IJ} \langle JJ | \mathcal{T}_0^1 | JJ \rangle$ where μ is the nuclear magnetic dipole moment and $\mathcal{T}_0^1$ is an irreducible spherical tensor operator of rank 1 which operates in the space of electron coordinates and spin. Similarly, the B coefficient represents the interaction strength between the valence electron and the nuclear electric quadrupole moment and may written as $B = 2Q \langle JJ | \mathcal{T}_0^2 | JJ \rangle$, where Q is the nuclear electric quadrupole moment and $\mathcal{T}_0^2$ is an irreducible spherical tensor operator of rank 2 which operates in the space of electron coordinates and spin. In the above notation, $|JJ\rangle = |J, m_J{=}J\rangle$. It should be noted that even if allowed by parity and angular selection rules, hyperfine interactions due to nuclear multipolarity > 2 are neglected in Equation (56) due to their smallness.

Prior to this work, the hyperfine A and B coefficients of $^{229}\text{Th}^{3+}$ had not been measured. It is, therefore, very useful to obtain estimates of these constants for initial spectroscopic

work. The accepted value of the dipole moment is $\mu = 0.46(4)\,\mu_N$ [38] and that of the quadrupole moment is $Q = 4.3(9)$ eb [38]. Values of $\langle JJ|\mathcal{T}_0^2|JJ\rangle$ are obtained for relevant orbitals from theoretical calculations by Berengut *et al.* [39] where resulting inaccuracies are expected to be at the level a few percent. While there are no published calculations of the $\langle JJ|\mathcal{T}_0^1|JJ\rangle$ matrix elements, preliminary estimates [40] indicate that the resulting A coefficients are significantly smaller than the corresponding B coefficients. In total, the accepted nuclear moments and uncertainties combined with the electronic matrix element calculations and uncertainties result in level shift estimates of up to ~2 GHz with uncertainties of several hundred MHz. Though not ideal, this knowledge does produce coarse pictures of the anticipated optical spectra which aid in assessing hardware requirements for performing precision spectroscopy.

In addition to the complicated hyperfine structure, shifts of the fine structure levels on the GHz scale arise when transitioning from ^{232}Th^{3+} to ^{229}Th^{3+}. These relative isotope shifts are due to the finite nuclear mass and its change between isotopes, the mass shift, and the change in nuclear size between isotopes, the field shift. Due to the large nuclear mass and charge of thorium isotopes, the field shift produces the dominant contribution to inter-isotope fine structure level shifting [41]. This contribution is, therefore, of interest for estimating the relative isotope shifts.

When transitioning from one isotope to another, the number of neutrons within the nucleus changes. This alters the charge distribution of the protons, in turn changing the electric potential within the nucleus. This perturbation effects the electrons due to the overlap of their wavefunctions with the nucleus. This produces an energy shift of electronic energy levels (the field shift) and may be expressed as $\Delta E_{iso} = F_{iso}\,\delta\langle r^2\rangle$, where F_{iso} is known as the field shift constant and $\delta\langle r^2\rangle$ is the change in nuclear mean-square radius. F_{iso} has been calculated for various low-lying electronic levels within ^{229}Th^{3+} by Berengut *et al.* [39]. The change in mean-square radius from the 232 isotope to the 229 isotope is estimated from [42] to be $\delta\langle r^2\rangle = \langle r^2\rangle_{229} - \langle r^2\rangle_{232} = -0.334 \pm 0.045$ fm^2. With the

calculations of [39], this leads to relative isotope shift estimates for ^{229}Th fine structure levels of -11(3) GHz for the $5F_{5/2} \leftrightarrow 6D_{3/2}$ transition, -12(3) GHz for the $5F_{5/2} \leftrightarrow 6D_{5/2}$ transition, and -11(3) GHz for the $5F_{7/2} \leftrightarrow 6D_{5/2}$ transition.

4.3   Laser Spectroscopy of $^{229}Th^{3+}$

With the complex hyperfine structure present within each fine structure level, laser spectroscopy and the resulting transition spectra for ^{229}Th^{3+} are significantly more complicated than for ^{232}Th^{3+}. The core difficulty in performing spectroscopy on this system arises due to the large number of ground and metastable levels to which an excited ion may decay. If not excited from these levels, the ion is left dark, being neither laser cooled nor optically detected. Avoiding this problem requires either sufficient knowledge of all optical transition frequencies, which is not initially known, or sufficiently broadband excitation fields to semi-blindly access all stable states.

Fortunately, repumping ions from dark states only requires a small fraction of saturation intensity, so one can afford to broaden laser light and distributed its spectral density across a large range of possible transition frequencies while maintaining sufficient density to destroy dark states. Additionally, Doppler broadening of the trapped ions may be utilized to effectively smear the transitions in frequency space, relaxing the need for a genuinely continuously broadened laser spectrum over the range of interest.

To produce a sufficiently broadband excitation spectrum, laser light is passed through a 10 GHz bandwidth phase modulator where it acquires rf sidebands every 200 MHz out to about ±1200 MHz ($\beta \approx 6$). In conjunction with a room temperature Doppler broadened sample, this type of spectrum is sufficiently continuous across a ~3 GHz bandwidth. After roughly determining the isotope shifts with such spectra, a single laser spectrum can be narrowed to obtain higher resolution scans. Such a scan is shown in Figure 39 where the 984 nm light is broadened to about 250 MHz with 50 MHz phase modulation and scanned via the laser PZT voltage. The 690 nm light is broadened to ~3 GHz with the carrier

frequency fixed at maximum fluorescence. 984 nm fluorescence is collected on the camera with ~2 s of integration per data point while a fraction of the 984 nm excitation field which is not spectrally broadened is sent to the wavemeter for optical frequency measurement. For comparison, the narrow gray lines represent high resolution results obtained later using ultra-cold samples. The peak heights indicate dipole matrix element amplitudes.
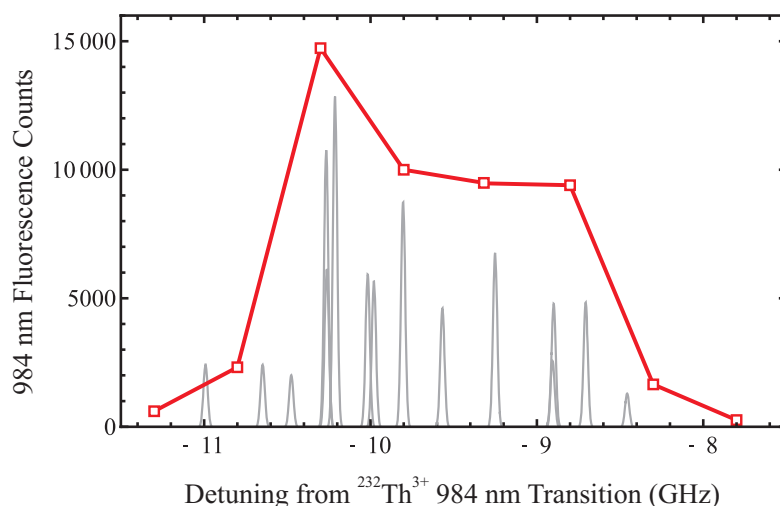
Figure 39: An optical scan of the 984 nm transition in $^{229}Th^{3+}$ with 250 MHz broadened 984 nm probe light. The 690 nm field is broadened to ~ 3 GHz to destroy dark states. The narrow gray lines represent high resolution results obtained later using ultra-cold samples. The peak heights indicate dipole matrix element amplitudes.

Higher resolution spectra are obtained at 690 nm using monochromatic light. With broadened 984 nm and 1088 nm light applied to a room temperature sample, the 690 nm laser is locked to the transfer cavity and a weak first-order rf sideband ($\beta \approx 0.4$) is scanned in 100 MHz steps. Two separate scans are made to avoid interaction of a second-order sideband with the ions at low modulation frequencies. Fluorescence at 984 nm is monitored on the camera with 2 s of integration per frequency step. With an average of 5 scans, very clear structure begins to emerge, as seen in Figure 40. Again, for comparison, the narrow gray lines represent results obtained later in ultra-cold samples with peak heights corresponding to dipole matrix element amplitudes.

With some gross structure of $^{229}Th^{3+}$ becoming visible, preliminary comparisons show
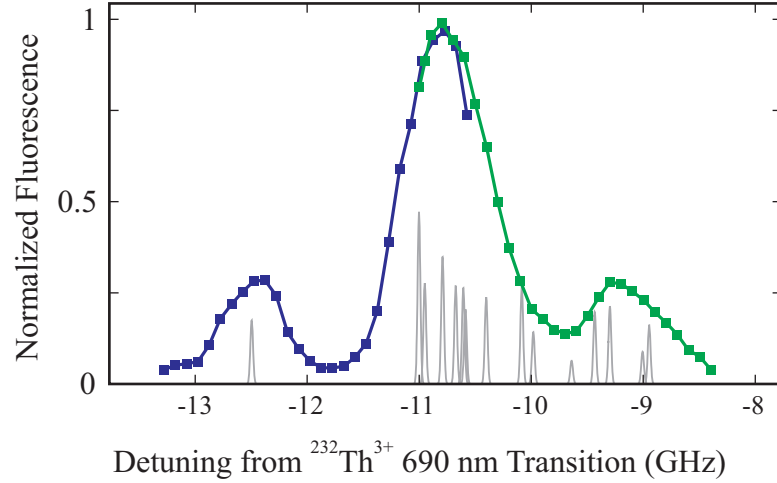
Figure 40: An average of 5 optical scans of the 690 nm transition in ^{229}Th^{3+} with monochromatic 690 nm probe light. The 984 nm and 1088 nm fields are broadened to $\sim$ 3 GHz to destroy dark states. The narrow gray lines represent high resolution results obtained later using ultra-cold samples. The peak heights indicate dipole matrix element amplitudes.

agreement between measurements and expected hyperfine coefficient values and isotope shifts. This motivates the transition to the next stage of spectroscopy where sympathetic cooling of ^{229}Th^{3+} is done with laser cooled ^{232}Th^{3+}.

Because the thorium nitrate source containing the 229 isotope also contains a significant amount of the 232 isotope, loading of dual isotope samples is exploited to bring ^{229}Th^{3+} into the ultra-cold regime without direct laser cooling. Because the Coulomb interaction between the trapped ions serves to efficiently thermalize the sample, laser cooling one component of the sample sympathetically cools the remaining ions. This is effective as long as the laser cooling rate is larger than the heating rate of the entire sample. With optimized dc compensation voltages and a minimal q, the $\sim$1:3 ratio of ^{232}Th to ^{229}Th is sufficiently high for the laser-cooled ^{232}Th^{3+} to bring the Doppler width of ^{229}Th^{3+} transitions to $\lesssim$ 10 MHz. Figure 41 is an image of such a sample. The different masses separate with the heavier 232 isotope accumulating radially toward the outer regions. The dark core region of this prolate ellipsoid is populated by ^{229}Th^{3+} which is maintained in an ultra-cold phase due to Coulomb coupling to the crystallized shell of ^{232}Th^{3+}. This dark region (outlined

74

in white dashes) is monitored for fluorescence when the ^{229}Th^{3+} optical fields are scanned. Such samples used for spectroscopy survive in the trap for several minutes.
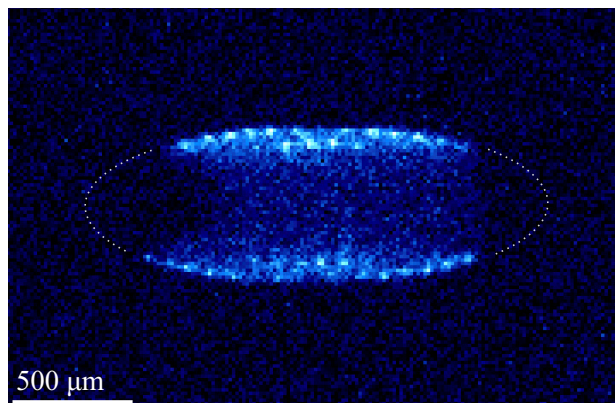
Figure 41: A crystallized shell of ^{232}Th^{3+} ions surrounding a dark core of ^{229}Th^{3+} ions. The white dotted line indicates the projected border of the prolate ellipsoid sample. Coulomb coupling between the two components of the sample maintain the dark ions in an ultra-cold phase for precision spectroscopy.

Due to the relatively low optical power requirements of the Λ-system lasers for spectroscopy and laser cooling, an experimental simplification is made in using only one laser at each wavelength. This is done by producing rf sidebands on the light via 10 GHz bandwidth phase modulators such that sufficient spectral density is appropriately distributed for laser cooling and spectroscopy of both isotopes. This is most conveniently done by locking each of the two lasers roughly between the two isotopes ($|\delta_{690,984}| \sim 5$ GHz) and generating small rf sidebands in the range 3 - 7 GHz. In this setup, $\beta \approx 0.4$ for each rf frequency, placing about 3 - 5% of the total power in each of the $\pm 1^{st}$ order sidebands. The small modulation maintains a sufficiently clean spectrum due to very small higher-order sidebands and cross-modulation. One requirement for successful spectroscopy here is that the rf sideband exactly opposite of that assigned to interaction with isotope A does not interact with isotope B. For example, if a transition in isotope A is + 5000 MHz from the laser lock point, the lock point detuning of a transition in isotope B should not be near - 5000 MHz. Because the optical power requirements of the 1088 nm fields are high, a separate laser is dedicated to each isotope, though phase modulation of the 229 isotope light is still done to

conveniently access any or all 1088 nm transitions within $^{229}\text{Th}^{3+}$.

The most convenient optical transitions for initial interrogation within ultra-cold samples are those between the $5F_{5/2}$ and $6D_{5/2}$ manifolds (690 nm). To observe all 15 lines, 984 nm and 1087 nm fields are sufficiently broadened to access all stable levels, leaving no dark states to be populated (Figure 42). A single rf sideband applied to the 690 nm light is scanned across the $^{229}\text{Th}^{3+}$ spectrum. When a resonance is achieved, a fraction of the ion population is transfered into the $5F_{7/2}$ manifold where the 984 nm light interacts, producing 984 nm fluorescence which is detected by the camera. When maximum fluorescence is achieved, the rf frequency is recorded along with an estimated uncertainty based on signal strength and spectral width.
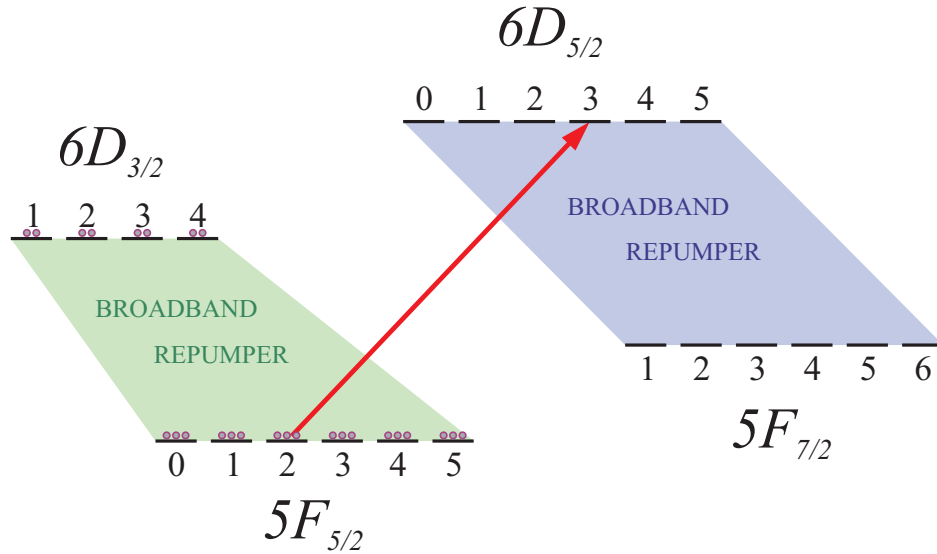
Figure 42: The spectral configuration used for initial high resolution spectroscopy of all 15 transitions at 690 nm.

Because the detuning of the 690 nm laser lock point from the $^{232}\text{Th}^{3+}$ transition is reliably determined to a few hundred kHz due to stable laser locking, $^{229}\text{Th}^{3+}$ transition frequency shifts from this physically relevant reference point may be determined with accuracy much greater than that provided by the wavemeter. With a complete scan, all 15 lines are observed with measurement inaccuracies estimated to be <8 MHz.

Hyperfine coefficients and the relative isotope shift are extracted from the data using a

least squares fit to a model containing terms expressed as

$$\Delta E_{e,g} = \frac{K_e}{2}A_e + \frac{\frac{3}{2}K_e(K_e + 1) - 2I(I + 1)J_e(J_e + 1)}{4I(2I - 1)J_e(2J_e - 1)}B_e \tag{57}$$

$$- \frac{K_g}{2}A_g - \frac{\frac{3}{2}K_g(K_g + 1) - 2I(I + 1)J_g(J_g + 1)}{4I(2I - 1)J_g(2J_g - 1)}B_g + \Delta, \tag{58}$$

where the subscript g(e) indicates the ground (excited) state, $K_i = F_i(F_i+1)-I(I+1)-J_i(J_i+1)$, and Δ represents the relative isotope shift between the two manifolds. All least-squares fitting computations are done with 16 digits of working precision.

In order to properly assign values to F_g and F_e for each of the 15 transitions, a search algorithm which attempts fits for all viable assignment combinations is utilized. The algorithm begins with fitting only 6 of the 15 data points to the 5 fit parameters. This is the minimum number of data points required to produce a meaningful best-fit error estimate. The root-mean-square of the 6 residuals (residual rms) is then calculated and the solution is deemed viable if and only if the $rms < 15$ MHz. All other F assignment combinations are discarded. After all $(15 - 5)! \approx 3.6$ million initial combinations are attempted, the process is repeated using the remaining viable subset in addition to a seventh data point which takes on all possible remaining F assignments. This process is repeated until all 15 data points have been introduced. After requiring that the resulting best-fit value for B be positive, the initial set of $15! \approx 1.3 \times 10^{12}$ possible combinations is reduced to only three viable F assignment combinations. To discern between the real solution and incorrect results, an average confidence level is calculated for each assignment combination. This is done by first estimating the confidence level for each data point by assuming a normal measurement error distribution with standard deviation equal to the estimated statistical measurement error. The confidence level for the ith data point may be expressed as

$$CL_i = 1 - \frac{1}{\sigma_i \sqrt{2\pi}} \int_{-\epsilon_i}^{\epsilon_i} \exp\left[-\frac{x^2}{2\sigma_i^2}\right] dx \tag{59}$$

where σ_i and ϵ_i are the estimated statistical measurement error and fit residual of the ith

77

data point, respectively. An average confidence level is then calculated as

$$\langle CL \rangle = \left(\prod_i^{15} CL_i \right)^{1/15} \tag{60}$$

Figure 43 displays residuals from the three viable F assignment combinations along with *rms* and $\langle CL \rangle$ calculations. With the assumption that the $\langle CL \rangle$ values are indicative of the accuracy of the fit, the solution displayed in the right end panel is assumed correct and used for further work. Later results via spectroscopy of the 1088 nm and 984 nm transitions in conjunction with optical pumping and angular momentum selection rules confirm that this is the correct F-number assignment combination.
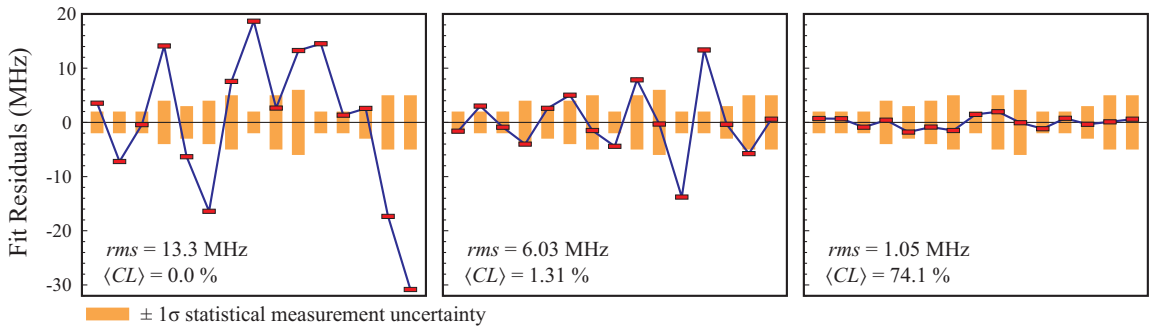
Figure 43: Fit residuals of the three viable F-number assignment combinations for the 15 measured transition frequencies at 690 nm, along with *rms* and $\langle CL \rangle$ calculations.

With relatively precise knowledge of the $5F_{5/2}$ and $6D_{5/2}$ hyperfine structure, the next step is to measure the various 1088 nm transitions, unveiling the structure of the $6D_{3/2}$ manifold. This is done in a straight-forward manner when realizing the protocol illustrated in Figure 44. In this configuration, broadband 984 nm light empties the metastable $5F_{7/2}$ manifold and the 690 nm field leaves one known ground level dark so that it is completely populated. With a 1088 nm probe laser locked to the transfer cavity, its light is first passed through a phase modulator where it is modulated at a single frequency and then sent along the trap axis where it illuminates the ions. By scanning an rf sideband through the entire 1088 nm spectrum, resonances occur and ions are pumped from the dark state and are partially redistributed among certain allowed ground levels due to spontaneous decay. The ions are then transferred to the $5F_{7/2}$ manifold where they scatter light which is detected by

the camera. When maximum fluorescence is observed, the rf frequency is recorded along with an estimated statistical uncertainty dependent upon signal strength and spectral width. In this protocol, the number of observed lines provides information regarding the value of F_g. This comes from the electric dipole selection rule $\Delta F = 0, \pm 1$ for $\Delta J \neq 0$. For example, if three transitions are observed during a complete scan, F_g must equal 2 or 3. This serves as a consistency check for the F-number assignments of the 690 nm transitions.
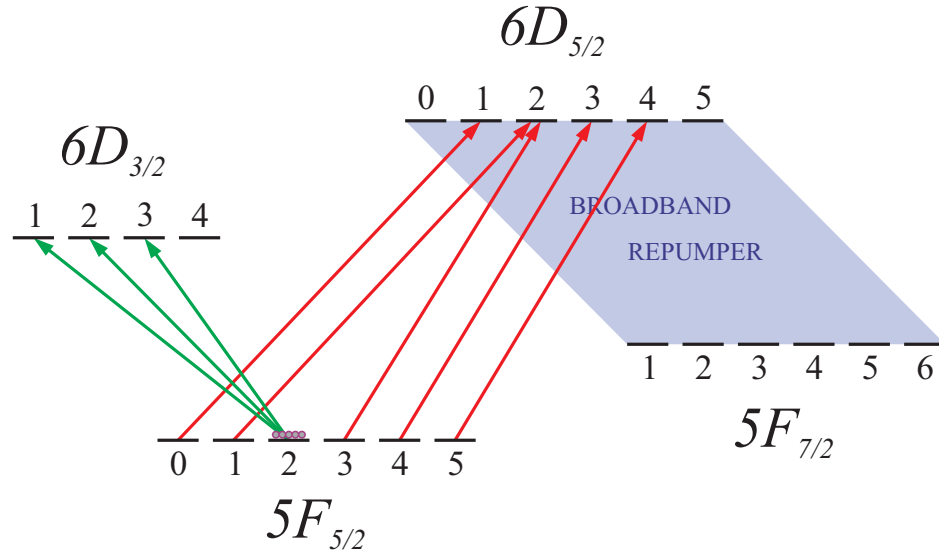
Figure 44: Spectral configuration used for high resolution spectroscopy of the $6D_{3/2}$ manifold hyperfine structure.

With knowledge from the 690 nm dataset and fit, F-number assignments are straight forward for the 1088 nm lines. The resulting 1088 nm data is then combined with the 690 nm data to perform a semi-global least squares fit. The high quality of this fit ($\langle CL \rangle \approx 80\%$) confirms the correctness of the F-number assignments for all 1088 nm and 690 nm data points. To be certain of the F assignment correctness, a search protocol similar to that used for the 690 nm data points is employed, resulting in only one viable solution.

The final set of transitions to be measured (984 nm) is done in an iterative fashion with the first step illustrated in Figure 45. A 984 nm broadband repumper initially empties the $5F_{7/2}$ manifold while a select set of 1088 nm fields optically pump the ions into the $|5F_{5/2}, F = 1\rangle$ ground level. A single 690 nm spectral component then excites the ions

into the $|6D_{5/2}, F = 0\rangle$ level where, due to electric dipole selection rules, the ions may only decay to either the $|5F_{5/2}, F = 1\rangle$ or $|5F_{7/2}, F = 1\rangle$ level. A narrowband spectral component is added to the broadband 984 nm repumping field and scanned across the entire 984 nm spectrum. When this field is resonant with the $|5F_{7/2}, F = 1\rangle \leftrightarrow |6D_{5/2}, F = 0\rangle$ transition, the low ion fluorescence level from the repumper field is dramatically increased due to the increased excitation efficiency. When maximal fluorescence is observed, the rf frequency and estimated error are recorded.

Because the $6D_{5/2}$ hyperfine structure is already known from the 690 nm measurements, an extension to measuring the $|5F_{7/2}, F = 2\rangle \leftrightarrow |6D_{5/2}, F = 1\rangle$ transition is easily made. This process is then extended to excitation from all $5F_{7/2}$ levels. This dataset provides complete information of all hyperfine splittings of the manifold.
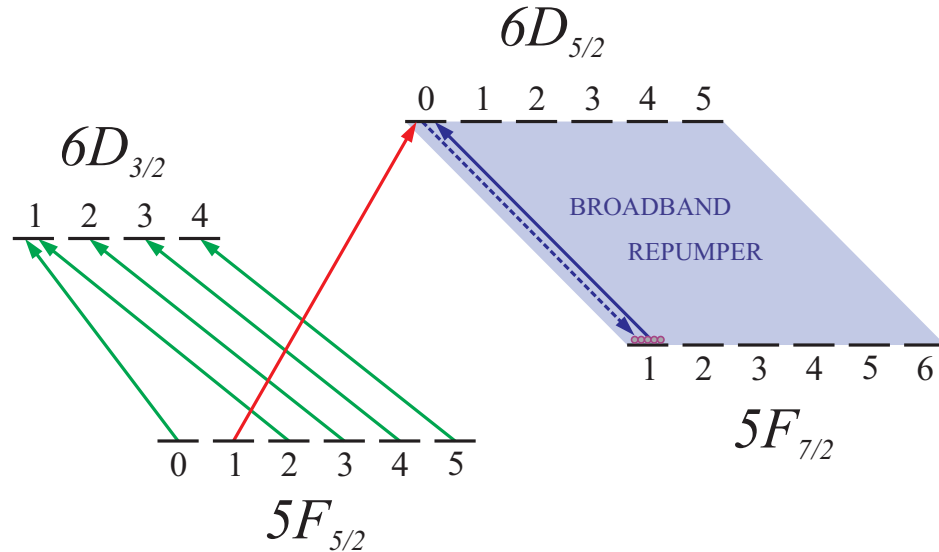
Figure 45: Spectral configuration for high resolution spectroscopy of the $|5F_{7/2}, F = 1\rangle \leftrightarrow |6D_{5/2}, F = 0\rangle$ transition.

With a total of 29 frequency measurements, a global least-squares fit is made to the data. To test the quality of the fit and correctness of the F-number assignments, the *rms* and $\langle CL \rangle$ are calculated from the best-fit residuals. Figure 46 shows the residuals from this fit along with the *rms* and $\langle CL \rangle$.

In order to estimate the uncertainties in the 11 global fit parameters (4 *A*'s, 4 *B*'s, and
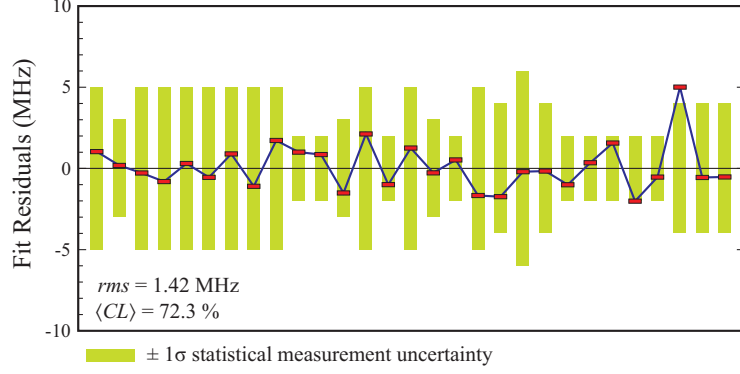
Figure 46: Residuals of a global least-squares fit of all 29 measured transitions and calculated *rms* and $\langle CL \rangle$.

3 Δ's), a Monte Carlo simulation is performed. By adding a set of small, uncorrelated, random perturbations to all of the 29 input data points, slightly different best-fit values are obtained for the fit parameters. If this process is done many times with the distribution of the data set perturbations representative of the statistical uncertainties combined with possible systematic uncertainties, a set of values may be acquired for each fit parameter. From each data set, an average best-fit value and a best-fit standard deviation are calculated. This standard deviation of the best-fit data set represents an estimate of the best-fit uncertainty for that fit parameter.

To carry out this estimate, one must decide upon appropriate distribution widths of the data point fluctuations. Because the deviation of combined statistical and systematic uncertainties is relatively small for the input data set, the simulation assumes identical data fluctuation distributions for each input data point. The average combined statistical and light-shift uncertainty from all 29 data points is 4 MHz. To account for additional uncertainties in laser-cooling dynamics and Zeeman splitting combined with optical pumping effects, a 4 MHz contribution is added linearly to this, resulting in an 8 MHz standard deviation for the estimated error distribution of each of the input data points. For the simulation, a normal distribution of data fluctuations is used, though the final results of interest are not sensitive to the particular shape of the function, only its standard deviation. The

Central Limit Theorem and the sufficiently large number of input data points used, 29, ensure this [36]. As confirmation, the simulation is also done with a top hat distribution of standard deviation 8 MHz. To obtain an 8 MHz standard deviation, the half width of the top hat must be $\sqrt{3} \times 8$ MHz ≈ 14 MHz.
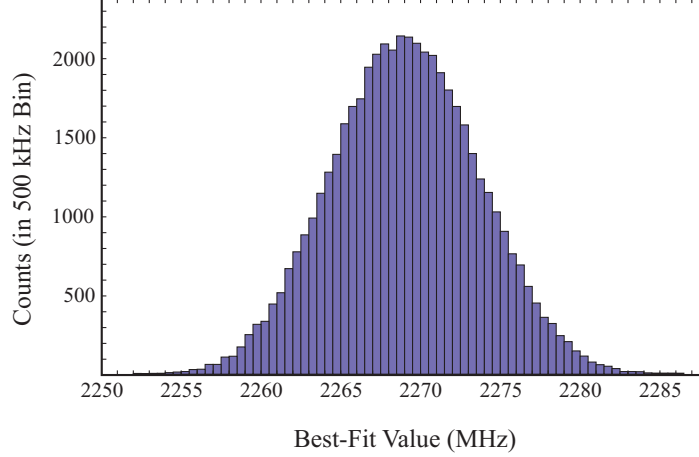
Figure 47: Histogram of 50,000 best-fit values of the $5F_{5/2}$ orbital B coefficient generated from global least-squared fits to fluctuating input data points. The bin widths are 500 kHz.

With a set of distributed random fluctuations of standard deviation 8 MHz added to the 29 input data points, a set of slightly perturbed parameter best-fit values are obtained. This process is repeated 50,000 times to acquire sufficient statistics. A representative histogram of a best-fit data set is shown in Figure 47. Here, the hyperfine B coefficient of the $5F_{5/2}$ valence orbital has a mean value of 2269 MHz and a standard deviation of 6 MHz. As expected, the mean agrees with the unperturbed fit results. The standard deviation of this and the other 10 data sets is the same for both the normal and top hat fluctuation models. The resulting 6 MHz is taken to be the estimated uncertainty of B. When considering the isotope shifts, an additional shift of 6 MHz is added linearly to the best-fit uncertainties to account for possible correlated errors among the measured data points. A complete set of parameter best-fit values and uncertainties are shown in Table 2.

With precise measurements of multiple B constants and access to high precision atomic structure calculations of the $\langle JJ|\mathcal{T}_0^2|JJ\rangle$ matrix elements for these same valence orbitals

Table 2: Measured ^{229}Th^{3+} hyperfine constants and relative isotope shifts from ^{232}Th^{3+}. Labels A and B signify magnetic dipole and electric quadrupole hyperfine constants, respectively. All units are MHz and all uncertainties are 1 σ.

Valence Orbital	A	B	Transition	Isotope Shift
$5F_{5/2}$	82.2(6)	2269(6)	$5F_{5/2} \leftrightarrow 6D_{3/2}$	-9856(10)
$5F_{7/2}$	31.4(7)	2550(12)	$5F_{5/2} \leftrightarrow 6D_{5/2}$	-10509(7)
$6D_{3/2}$	155.3(12)	2265(9)	$5F_{7/2} \leftrightarrow 6D_{5/2}$	-9890(9)
$6D_{5/2}$	-12.6(7)	2694(7)		

[39], extraction of the ^{229}Th nuclear quadrupole moment is possible. Considering the ith orbital, Q may be estimated as $Q_i = \dfrac{B_i}{2\,_i\langle JJ|\mathcal{T}_0^2|JJ\rangle_i}$ with an uncertainty determined by the combined uncertainty of the measurement of B_i and the calculation of $_i\langle JJ|\mathcal{T}_0^2|JJ\rangle_i$. Including the entire set of four valence orbitals measured here, the unweighted average value for Q is $\langle Q \rangle = 3.11$ eb. The maximum residual is 5.5% with a residual standard deviation of 4.3%. Because these values are much larger than the measurement uncertainties ($<0.5\%$), theoretical calculations are identified as the major source of error. The residuals of the data set are within expectation of calculation inaccuracies and the uncertainty in $\langle Q \rangle$ is assigned the value 5% [43]. The data set standard error of 2.1% composes only a fraction of the total uncertainty due to the likely presence of unobservable correlated errors among the four calculations. In conclusion, a new value for the ^{229}Th nuclear ground state electric quadrupole moment of $Q = 3.11(16)$ eb is deduced.

This result may be compared to the accepted value of $Q = 4.3(9)$ eb which was obtained using spectroscopy and atomic structure calculations of ^{229}Th$^+$ [38], a significantly more complicated system which has three valence electrons. Comparison may also be made to an infrequently cited result utilizing Coulomb excitation of the nucleus [44]. There, $Q = 3.149 \pm 0.032$ eb, in good agreement with the result here.

6D_{3/2}

$6D_{3/2}$

($\tau = 1090$ ns)

$g_J = 4/5$
(1.12 MHz/G-m$_J$)

9856(10) MHz

$g_F = 3/10$ **F = 4**
(0.42 MHz/G-m$_F$)

$g_F = -3/5$ **F = 1**
(-0.84 MHz/G-m$_F$)

1148.5(5.0) MHz

769.8(8.9) MHz

2432.9(8.7) MHz

1501.0(7.6) MHz

731.2(4.0) MHz

1284.3(5.0) MHz

$g_F = 1/15$ **F = 2**
(0.09 MHz/G-m$_F$)

553.1(5.4) MHz

$g_F = 7/30$ **F = 3**
(0.33 MHz/G-m$_F$)

Th-232
1 087.755 07(10) nm
275.606 583(26) THz
9 193.246 05(87) cm^{-1}
1.139 817 14(11) eV

Th-229
1 087.793 97(12) nm
275.596 727(31) THz
9 192.917 3(10) cm^{-1}
1.139 776 38(13) eV

$g_F = 3/7$ **F = 5**
(0.60 MHz/G-m$_F$)

F = 0

1081.1(4.0) MHz   462.4(1.6) MHz

868.9(6.7) MHz

$g_F = 3/7$ **F = 1**
(0.60 MHz/G-m$_F$)

406.6(5.4) MHz

1772.5(4.7) MHz

313.9(3.5) MHz

720.5(2.6) MHz

691.4(2.2) MHz

$g_F = 3/7$ **F = 2**
(0.60 MHz/G-m$_F$)

884.1(2.4) MHz

570.2(2.8) MHz

$g_F = 3/7$ **F = 4**
(0.60 MHz/G-m$_F$)

192.7(2.4) MHz

$g_F = 3/7$ **F = 3**
(0.60 MHz/G-m$_F$)

$g_J = 6/7$
(1.20 MHz/G-m$_J$)

5F_{5/2}

$5F_{5/2}$

Figure 48: Frequencies measured in this work among the $5F_{5/2}$ and $6D_{3/2}$ orbitals in ^{232}Th^{3+} and ^{229}Th^{3+}. Excited state lifetimes are taken from Safronova *et al.* [30] and *g*-factors are calculated from [31].
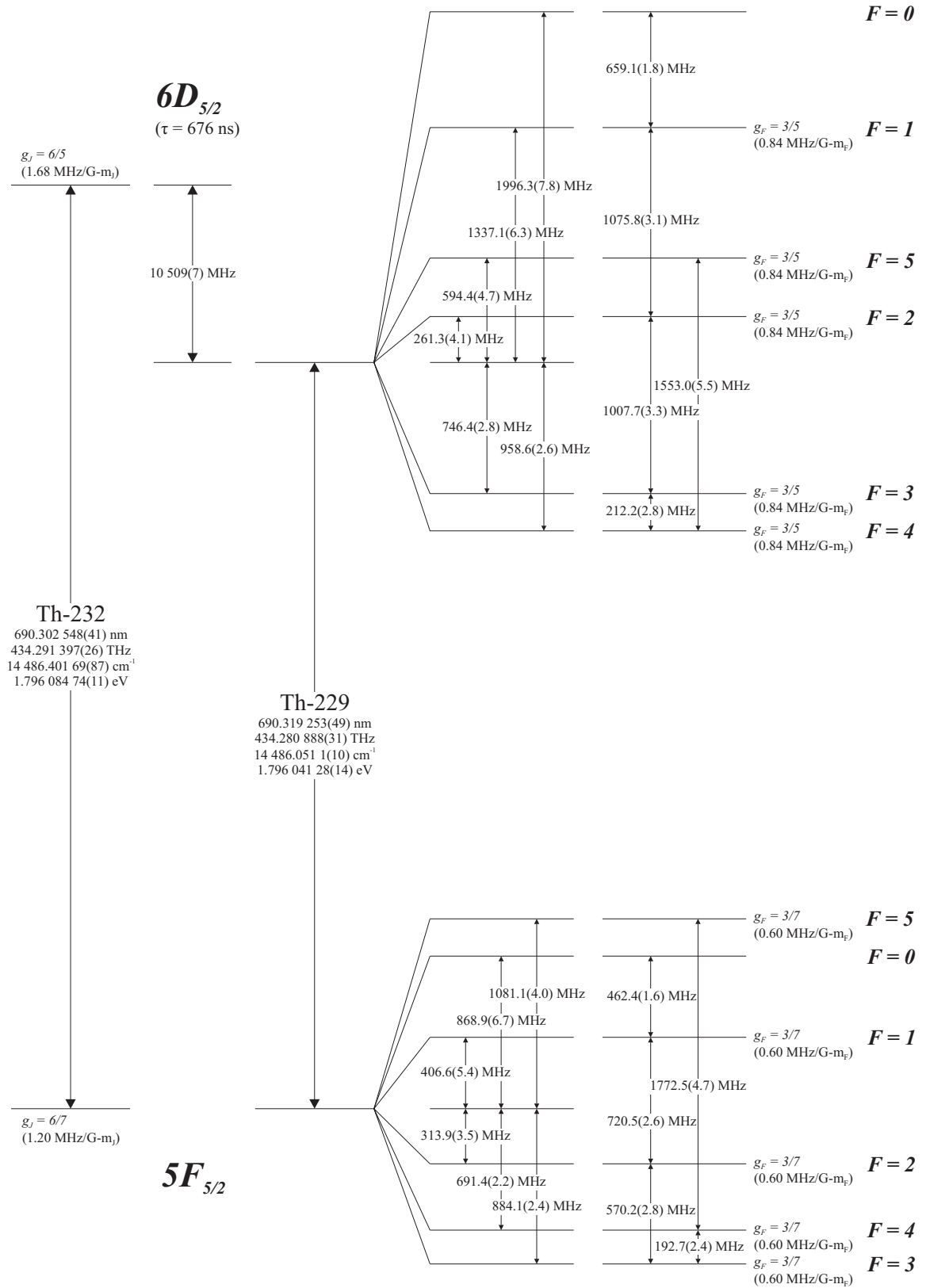
Figure 49: Frequencies measured in this work among the $5F_{5/2}$ and $6D_{5/2}$ orbitals in ^{232}Th^{3+} and ^{229}Th^{3+}. Excited state lifetimes are taken from Safronova *et al.* [30] and *g*-factors are calculated from [31].

85
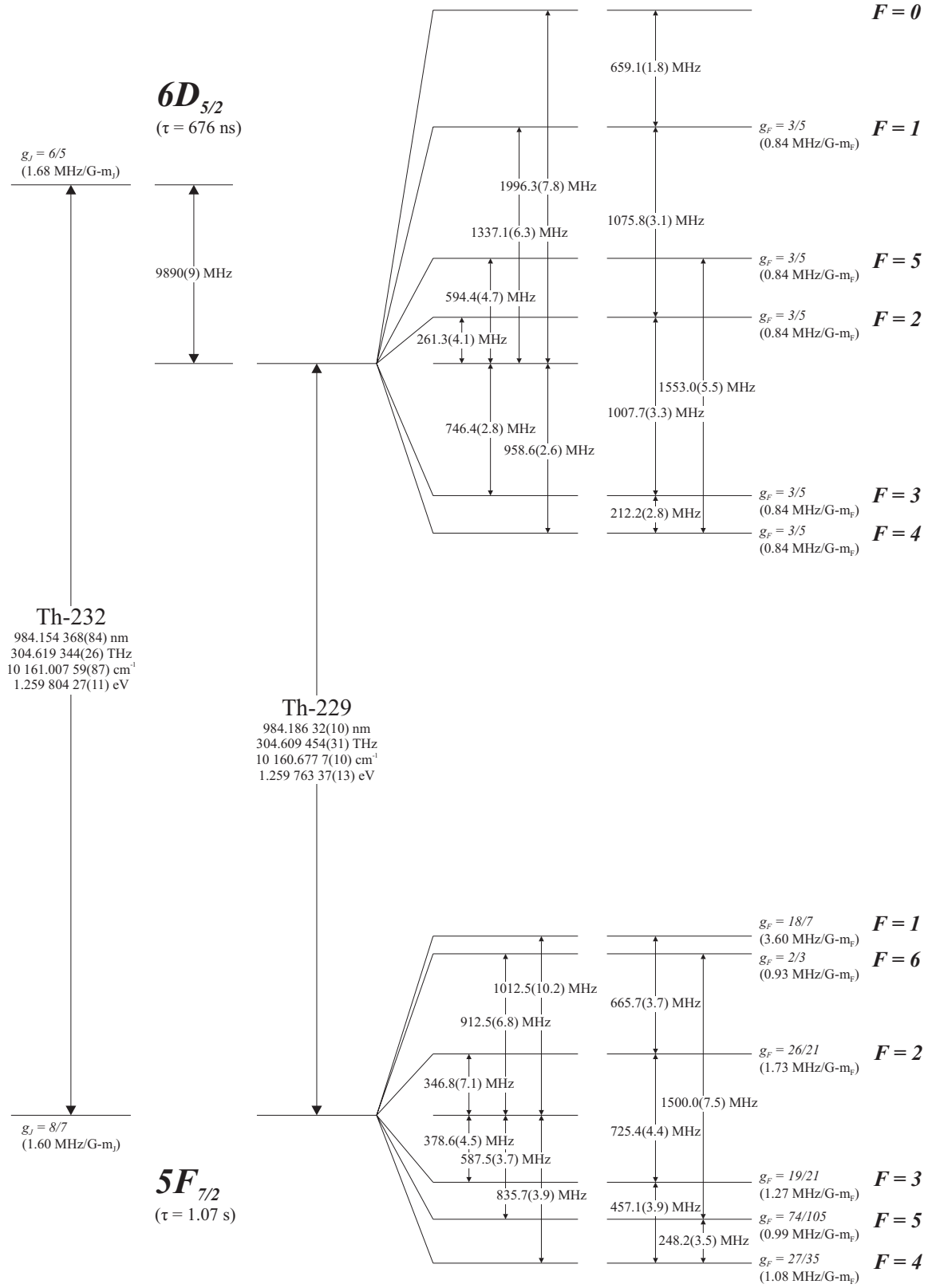
Figure 50: Frequencies measured in this work among the $5F_{7/2}$ and $6D_{5/2}$ orbitals in ^{232}Th^{3+} and ^{229}Th^{3+}. Excited state lifetimes are taken from Safronova *et al.* [30] and *g*-factors are calculated from [31].

CHAPTER V

NUCLEAR LASER SPECTROSCOPY OF THORIUM-229

5.1 Nuclear Isomer Excitation

The nuclear isomer state in $^{229}\text{Th}^{3+}$ is expected to exist 7.6(5) eV above the nuclear ground state. In searching for this transition, one should consider $\pm 3\sigma$ as the entire search range. This suggests the spectral region 130 nm - 200 nm. Directly covering this range in search of a forbidden transition would be prohibitively expensive if not impossible, considering current laser technology. An alternative protocol is necessary.

Instead of direct magnetic dipole excitation, the electron bridge process may be utilized [45]. In this case, hyperfine-induced mixing of the ground and the isomer nuclear manifolds opens electric-dipole transitions between the two. The mixing is expected to be the strongest for the S-electronic states, as the electron probability density at the nucleus is highest. For example, considering only the $7S_{1/2}$ and $8S_{1/2}$ electronic orbitals in first-order perturbation theory,

$$\overline{|7S_{1/2}, m\rangle} \approx |7S_{1/2}, m\rangle + \frac{\langle 8S_{1/2}, g|H_{hyp}|7S_{1/2}, m\rangle}{E_{7S,m} - E_{8S,g}}|8S_{1/2}, g\rangle \tag{61}$$

where H_{hyp} is the hyperfine interaction Hamiltonian and $g(m)$ indicates the nuclear ground (isomer) state. The $|8S_{1/2}, g\rangle$ admixture, with expected amplitude of order 10^{-5} [10], couples to the $|7P_{1/2}, g\rangle$ level via electric-dipole radiation of frequency $(E_{7S,m} - E_{7P_{1/2},g})/\hbar$ (see Figure 51). This shifts the spectral interrogation region from the challenging 130-200 nm range to the manageable 250 - 800 nm range where high-power coherent light sources are available. Alternatively, $|7S_{1/2}, g\rangle \leftrightarrow |7S_{1/2}, m\rangle$ two-photon excitation through the $|7P_{1/2}, g\rangle$ level may be a suitable approach for the search. In this case, the spectral search range is 260 nm - 400 nm. It should be noted that because the hyperfine Hamiltonian is a scalar product of electronic and nuclear irreducible spherical tensor operators,

mixing of eigenstates preserves the total angular momentum F and orientation m_F [37].
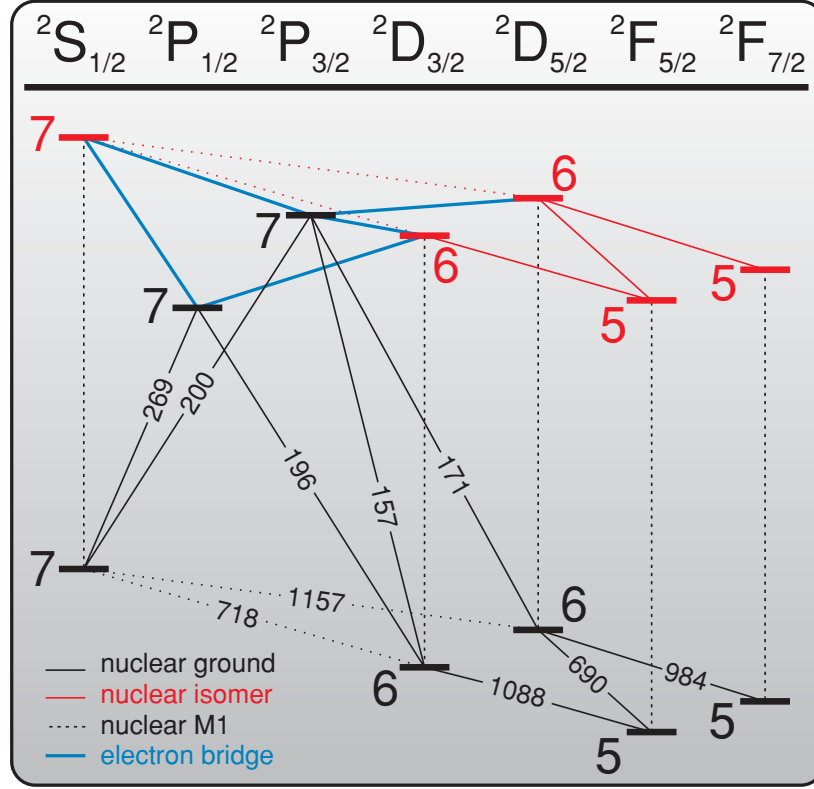
Figure 51: A diagram of electronic energy levels and electric dipole transitions including both nuclear ground and excited isomeric manifolds. Direct nuclear magnetic dipole (M1) decay channels and electron bridge pathways suitable for the isomer search are shown. Optical transition wavelengths are in nm and the integers near atomic levels indicate principle quantum numbers.

In general, the optical search time required to find the isomer transition energy can be estimated as $T \sim \Delta\omega/\Omega^2$, where Ω is the optical excitation Rabi frequency and $\hbar\,\Delta\omega$ is the energy range over which the search is conducted. For discussion, we define the indexes $\{1, 2, 3\}$ to correspond to levels $\{|7S_{1/2}, g\rangle, |7P_{1/2}, g\rangle, |7S_{1/2}, m\rangle\}$. To induce a resonant one-photon transition from level $|2\rangle$ to level $|3\rangle$, a single $^{229}\mathrm{Th}^{3+}$ ion may be placed at the center of a Gaussian light beam of power P and waist r_0 so that the squared Rabi frequency is

$$\Omega_{R1}^2 = \frac{4\,P\,d_{23}^{\ 2}}{\pi\,\epsilon_0 c\,r_0^{\ 2}\hbar^2} \tag{62}$$

where d_{23} is the effective electric dipole moment between levels $|2\rangle$ and $|3\rangle$.

To a good approximation, only the $|7P_{1/2}\rangle$ level contributes to the non-resonant two-photon process. Additionally, we assume the the laser detuning from the $|7P_{1/2}\rangle$ level is much larger than both resonant one-photon Rabi frequencies. In this case, to induce a non-resonant two-photon transition from $|1\rangle$ to $|3\rangle$, the squared Rabi frequency is written as

$$\Omega_{NR2}^2 = \left(\frac{2\,P}{\pi\,\epsilon_0\,c\,r_0^2\,\hbar^2} \right)^2 \left(\frac{d_{12}\,d_{23}}{\Delta} \right)^2 \tag{63}$$

where Δ is the laser detuning from level $|2\rangle$. Because the squared Rabi frequency here depends upon the square of the optical power, instantaneous optical power information is important, not simply the time-averaged power P_{avg}. P_{avg} is the relevant parameter for single-photon excitation. Specifically, for a pulse train with pulse repetition rate R and pulse duration τ, the squared Rabi frequency is equal to the continuous-wave squared Rabi frequency times the pulse compression ratio $1/R\tau$. Equation (63) is then augmented for pulsed light to be

$$\Omega_{NR2}^2 = \frac{1}{R\,\tau} \left(\frac{2\,P_{avg}}{\pi\,\epsilon_0\,c\,r_0^2\,\hbar^2} \right)^2 \left(\frac{d_{12}\,d_{23}}{\Delta} \right)^2 . \tag{64}$$

This indicates that two-photon excitation of the isomer is most efficiently done with very short pulses and low pulse repetition rates for a given average optical power. To calculate search times, the dipole moment $d_{12} = 2.4\,ea_0$ is taken from [30] and the electron bridge effective dipole moment $d_{23} = 5 \times 10^{-5}\,ea_0$ is extracted from [10]. Here, e is the electron charge and a_0 is the Bohr radius.

To excite the isomer, a convenient light source might be a fs oscillator or amplifier. Regarding technical aspects, high-energy ultra-short pulses from a fs Ti:Sapp laser are easily frequency-doubled and tripled to produce light in the spectral regions of interest. In this case, we assume $r_0 = 5\,\mu$m, $P_{avg} = 30$ mW, $R = 80$ MHz, and $\tau = 6$ fs, resulting in search times of $T_{R1} \sim 0.2$ hrs and $T_{NR2} \sim 10$ hrs. The largest peak resonant one-photon Rabi frequency for these parameters is about an order of magnitude smaller than the expected two-photon laser detuning.

It is stressed that these times represent ion illumination time estimates under the assumption of unit population in the lower level and do not consider experimental setup and re-alignment times. The experimental contributions to the actual search times serves to neutralize an extremely efficient excitation scheme due to laser tuning and re-alignment processes while spanning the entire search range.

5.2   Nuclear Optical Clock

A promising application of the low-lying nuclear transition is in ultra-precise timekeeping. The state-of-the-art trapped ion frequency standard utilizes a narrow optical transition between valence electron orbitals within a single ion confined in an rf trap. These clocks are currently limited to fractional inaccuracies of $\sim 10^{-17}$ [46, 47] due, in general, to second-order Doppler (time dilation) shifts from non-zero ion motion within the trap, the quadratic Stark effect via atomic collisions, laser light, trapping fields, and blackbody radiation, the Zeeman effect operational magnetic fields and those created by rf current withing trap electrodes, and in some cases the quadrupole shift which arises if one of the valence orbitals contains a quadrupole moment which interacts with external electric field gradients.

Implementing a nuclear transition would allow for the clock to be composed of two levels of identical electronic quantum numbers [11]. This feature would transfer external-field clock shift mechanisms from the valence electron to coupling with the nucleus, where the electric and magnetic interactions with external fields are significantly smaller. The features that a nuclear transition might bring to the science of precision time keeping could relax and simplify technological requirements while simultaneously allowing for superb performance.

In this section, a $^{229}\text{Th}^{3+}$ ion clock is assumed to operate using previously demonstrated single ion clock technology and lab environment conditions. Discussion is limited to relevant frequency shift mechanisms and nuclear clock performance is compared with that of leading single ion clocks.

5.2.1 Time Dilation Shifts

A ^{229}Th^{3+} clock ion might be confined in a linear rf trap with $r_0 \sim 500\,\mu m$, $\Omega \sim 2\pi \times$ 35 MHz, and radial trap frequencies of $\sim$3.5 MHz. Though a realistic trap would have sufficiently different trap frequencies for efficient laser cooling, the following calculations assume $\omega_{x,y} = 3.5$ MHz for simplicity. The axial trap frequency is set to 20 kHz. When considering the 1088 nm cooling transition ($\gamma/2\pi = 146$ kHz), the quantized energy levels of the transverse harmonic potential are well resolved. Their energies are

$$E_i = \left(n_i + \tfrac{1}{2}\right)\hbar\omega_i \quad n_i = 0,\ 1,\ 2,\ \ldots, \tag{65}$$

Within this strong binding limit, a weak cooling laser tuned to the -1 order motional sideband at $\omega_l - \omega_i$ may cool the ion down to a mean vibrational occupation number [48]

$$\langle n_i \rangle \approx \frac{5}{16}\left(\frac{\gamma}{\omega_i}\right)^2 . \tag{66}$$

This corresponds to a minimum average occupation number of 0.0005 for the ^{229}Th^{3+} ion cooled on the 1088 nm transition. Along the z-axis, the ion is in the weak binding limit where quantized vibrational levels are not resolved and so the classical Doppler limit is achieved. Recalling Equation (24), the total kinetic energy due to secular motion (including minimal micromotion) of the ion in this state is

$$E_K \approx 2\left(\langle n_x \rangle + \tfrac{1}{2}\right)\hbar\omega_x + 2\left(\langle n_y \rangle + \tfrac{1}{2}\right)\hbar\omega_y + \frac{\hbar\gamma}{4} \tag{67}$$

Using Equation (35), the time dilation shift due to secular motion is

$$\frac{\Delta\nu}{\nu} = -\frac{v^2}{2c^2} = -\frac{E_K}{mc^2} = -1 \times 10^{-19} .$$

Current ion clocks using tight traps can restrict stray electric fields to $\pm$ 10 V/m [46]. For a 10 V/m electric field along one of the radial trap axes of the ^{229}Th^{3+} clock, Equation (26) suggests an additional time dilation frequency shift of -2 $\times$ 10^{-18}. This is significantly larger than the thermal motion shift and turns out to be, by far, the largest systematic shift

expected in a ^{229}Th^{3+} nuclear clock. Taking a conservative stance, the estimated time dilation shifts are themselves assumed as the error in frequency measurement of the ^{229}Th^{3+} clock transition.

These results may be compared with corresponding errors in leading single ion clocks. In the ^{199}Hg$^+$ case [46], laser cooling is done on the 194 nm $S_{1/2} \leftrightarrow P_{1/2}$ transition where $\gamma = 2\pi \times 70$ MHz. This broad linewidth precludes direct sideband cooling, limiting the thermal time dilation shift to -3 $\times 10^{-18}$. In a recent error budget of the ^{199}Hg$^+$ clock performance, time dilation due to excess micromotion is -4$\times 10^{-18}$. In the ^{27}Al$^+$ clock, cooling and motional dynamics are more complex due to the use of quantum logic spectroscopy [49] and sympathetic cooling. In this system, the two trapped ions create 6 motional modes to be cooled while also allowing for ion position exchange. This exchange places the spectroscopy ion in a non-ideal electric field, introducing additional uncertainties in the time dilation estimates. Recent reports of time dilation errors in this system are 5×10^{-18} and 6×10^{-18} for thermal and micromotion, respectively [47]. Ultimately, when applying state-of-the-art trapping and field compensation protocols to all three clocks, the relative simplicity and high performance of the ^{229}Th^{3+} system is highlighted due to the narrow laser cooling transitions and large mass.

It is interesting to project future performance regarding time dilation shifts. If external electric fields are maintained at a level of ±1 V/m as opposed to the currently assumed range of ±10 V/m, which is technically very achievable, a lower radial trap frequency may be employed, e.g. 2 MHz, and both thermal and excess time-dilation shifts in a ^{229}Th^{3+} clock may be reduced to -6×10^{-20}.

5.2.2 Stark Shifts

For clock operation, the $|7S_{1/2}; g\rangle \leftrightarrow |7S_{1/2}; m\rangle$ transition is particularly appealing due to its angular momentum properties. The $|7S_{1/2}\rangle$ levels have predicted lifetimes of 0.59 s and predominantly decay via electric quadrupole coupling to their respective $6D$ orbitals

(Figure 51) [30]. Each level has a total electronic angular momentum $J = 1/2$, therefore, there is no electric quadrupole moment and the scalar and tensor polarizabilities for the two levels are identical to second order in perturbation theory. Clock shifts due to electric fields only begin to arise from the third-order Stark effect, an effect traditionally relevant only in microwave frequency standards [11].

Because Stark shifts in ion clocks arise mostly from trapping fields, collisions, and blackbody radiation, the static component of the third-order Stark effect is considered. Field oscillation frequencies from blackbody radiation at 300 K have a peak amplitude around 30 THz (10 μm) and ion trapping fields range from dc to tens of MHz. These sources have oscillation frequencies significantly smaller than the optical frequencies corresponding to dipole transitions within the clock ion. Electric fields from collisions have broad spectra and these shifts are also characterized by the static interaction. Collisional shifts may be extrapolated by comparing the ^{229}Th^{3+} blackbody shift to current ion clock collisional and blackbody shifts.

The hyperfine Stark effect arises in third order of perturbation theory, twice in the electric field and once in the hyperfine interaction [50]. In addition to the traditional hyperfine interaction, there exists the isomer field shift which is different for each nuclear state. This perturbation may simply be thought of as an electric monopole term of the hyperfine Hamiltonian but will be treated separately. This term is completely unique to the ^{229}Th atomic/nuclear system.

Though a complete treatment of level shifts in this regime is difficult and beyond the scope of this work, an order-of-magnitude estimate of the $|7S_{1/2}; g\rangle \leftrightarrow |7S_{1/2}; m\rangle$ transition sensitivity to electric fields may be made by extrapolating from previous high accuracy calculations [50]. Specifically, we choose the $|7S_{1/2}, F = 3; g\rangle \leftrightarrow |7S_{1/2}, F = 2; m\rangle$ transition ($F_{g,m} = I_{g,m} + 1/2$) for clock operation. The shift of the clock levels due to the hyperfine Stark effect may be written as

$$\Delta E_i^{(3)} = -\frac{1}{2}\left(\alpha_i^{(3)S} + \frac{3m_F^2 - F(F+1)}{F(2F-1)}\alpha_i^{(3)T}\right)\mathcal{E}^2 \tag{68}$$

93

where i indicates the $7S$ orbital of the nuclear ground or isomer state, $\alpha_i^{(3)S}$ and $\alpha_i^{(3)T}$ are respectively the scalar and tensor components of the third-order polarizability of the ith state, and $\mathcal{E}$ is the external electric field. Though $nS_{1/2}$ orbitals do experience both scalar and tensor hyperfine Stark shifts, the tensor components are, in general, much smaller than the scalar component [50, 51]. The significantly smaller tensor component involving the magnetic dipole hyperfine interaction is neglected in this estimate. The tensor component involving the electric quadrupole hyperfine interaction is also smaller, but due to the large magnitude of this interaction in ^{229}Th^{3+}, it is examined here. The scalar component does not involve the electric quadrupole hyperfine interaction.

The third-order scalar polarizability of a $|nS_{1/2}, F = I + 1/2\rangle$ level may be written as $\alpha^{(3)S} = \mu \mathcal{M}$, where μ is the nuclear magnetic dipole moment and $\mathcal{M}$ is a function of reduced electric dipole matrix elements and reduced electronic matrix elements $\langle\beta'\|\mathcal{T}^1\|\beta\rangle$ of the magnetic dipole hyperfine interaction [50,52]. Similarly, the component of the third-order tensor polarizability involving the electric quadrupole hyperfine interaction may be written as $\alpha_Q^{(3)T} = Q\mathcal{R}$, where Q is the nuclear electric quadrupole moment and $\mathcal{R}$ is a function of reduced electric dipole matrix elements and reduced electronic matrix elements $\langle\beta'\|\mathcal{T}^2\|\beta\rangle$ of the electric quadrupole hyperfine interaction. Calculations of $\mathcal{M}$ and $\mathcal{R}$ for various atomic systems are listed in Table 3 [50]. The calculation inaccuracies are at the level of a few percent for $\mathcal{M}$'s and about 30% for $\mathcal{R}$'s.

Table 3: Calculated electronic component of scalar and tensor third-order polarizability for S orbitals of various atomic species from Dzuba *et al.* [50]. Calculation uncertainties are expected to be a few percent for $\mathcal{M}$'s and about 30% for $\mathcal{R}$'s. Units are [10^{-10} Hz/(V/m)^2/μ_N] for $\mathcal{M}$ and [10^{-10} Hz/(V/m)^2/eb] for $\mathcal{R}$.

Z	Atom	$\mathcal{M}$	$\mathcal{R}$
37	Rb	0.340	-0.026
55	Cs	0.766	-0.05
70	Yb$^+$	0.171	-0.014
80	Hg$^+$	0.0535	-0.0018
87	Fr	1.74	-0.099

In thorium, $Z = 90$, which is similar to that for francium. This makes the calculation for francium particularly relevant. To extrapolate a value of $\mathcal{M}$ for the $|7S_{1/2}, F = I + 1/2\rangle$ states of $^{229}\text{Th}^{3+}$, a useful approximation may be made. Considering a ground $nS_{1/2}$ orbital (or lowest lying S orbital in the case of Th^{3+}), a substantial contribution to $\mathcal{M}$ ($\sim 1/2$) is derived from only two terms, those diagonal in the hyperfine interaction and second order in the electric dipole interaction connecting the nS and nP orbitals [52, 53]. We define $\mathcal{N}$ to represent $\mathcal{M}$ at this level of approximation, which is then expressed as [50]

$$\mathcal{N} = \frac{1}{3\sqrt{6}} \langle nS \|\mathcal{T}^1\| nS \rangle \left[\frac{\left|\langle nP_{1/2}\|d\|nS\rangle\right|^2}{\left(E_{nP_{1/2}} - E_{nS}\right)^2} + \frac{\left|\langle nP_{3/2}\|d\|nS\rangle\right|^2}{\left(E_{nP_{3/2}} - E_{nS}\right)^2} \right] \sim \mathcal{M} \qquad (69)$$

where d is the electric dipole operator. Because $\mathcal{N}$ recovers such a significant fraction of $\mathcal{M}$, one may make the approximation $\dfrac{\mathcal{N}_a}{\mathcal{N}_b} \approx \dfrac{\mathcal{M}_a}{\mathcal{M}_b}$ for similar atomic species a and b. This approximation is not likely to introduce inaccuracies greater than a factor of 2.

This approximation is made when extrapolating from the accurate Fr result in Table 3 to the Th^{3+} system. The matrix element $\langle 7S \|\mathcal{T}^1\| 7S \rangle_{\text{Th}} = 42$ GHz/μ_{N} is calculated for Th^{3+} using fully relativistic Dirac-Fock orbitals generated in the V_{DF}^{N-1} frozen-core potential [54]. This calculation performed for Cs and Fr yields inaccuracies no worse than a factor of 2 [55], which is the assumed error for the calculation here. Note that the Dirac-Fock calculation error is separate from that introduced by the $\dfrac{\mathcal{N}_a}{\mathcal{N}_b} \approx \dfrac{\mathcal{M}_a}{\mathcal{M}_b}$ approximation. With a measured value of the hyperfine A coefficient for the $7S$ level of Fr ($\langle 7S \|\mathcal{T}^1\| 7S \rangle_{\text{Fr}} = 12$ GHz/μ_N) [56] and the calculated reduced electric dipole matrix elements from [57],

$$\frac{\mathcal{N}_{\text{Th}}}{\mathcal{N}_{\text{Fr}}} \sim 3.5 \times 0.029 \approx 0.10$$

where the first factor on the right hand side represents the ratio of reduced dipole hyperfine matrix elements and the second, significantly smaller factor represents electric dipole transition strengths and energy splittings. Its small magnitude is due to the smaller dipole matrix elements and the relatively large energy splittings of the S and P orbitals in Th^{3+}

(269 nm and 200 nm) as compared to those in Fr (817 nm and 718 nm).

With the ratio $\dfrac{\mathcal{N}_{\mathrm{Th}}}{\mathcal{N}_{\mathrm{Fr}}}$, one estimates $\mathcal{M}_{\mathrm{Th}}$ to be

$$\mathcal{M}_{\mathrm{Th}} \sim \frac{\mathcal{N}_{\mathrm{Th}}}{\mathcal{N}_{\mathrm{Fr}}} \mathcal{M}_{\mathrm{Fr}} \sim 0.10 \times 1.74 \times 10^{-10}\,\mathrm{Hz/(V/m)}^2/\mu_{\mathrm{N}}$$

$$\sim 0.18 \times 10^{-10}\,\mathrm{Hz/(V/m)}^2/\mu_{\mathrm{N}}\,.$$

To test the validity of the $\dfrac{\mathcal{N}_{\mathrm{Th}}}{\mathcal{N}_{\mathrm{Fr}}} \approx \dfrac{\mathcal{M}_{\mathrm{Th}}}{\mathcal{M}_{\mathrm{Fr}}}$ approximation, a test extrapolation is done from the accurately calculated Cs results to the accurately calculated Fr results. The extrapolation estimate of $\mathcal{M}_{\mathrm{Fr}}$ differs from the high accuracy result by 10%, while an extrapolation from Cs to Rb produces an error of 2%. This suggests that the assumed inaccuracy of a factor of 2 for the extension from Fr to Th^{3+} is not likely to be too low.

To obtain an estimate of $\mathcal{R}$ for calculating the tensor polarizability due to the electric quadrupole hyperfine interaction, the same extrapolation method used for the scalar interaction is employed. A significant contribution to $\mathcal{R}$ comes from only one term, that of the $nP_{3/2}$ orbital, where the quadrupole hyperfine interaction first appears. An estimate of $\mathcal{R}$ may be expressed as [50]

$$\mathcal{S} = -\frac{1}{4\sqrt{15}} \langle nP_{3/2} \| \mathcal{T}^2 \| nP_{3/2} \rangle \left[\frac{\left| \langle nP_{3/2} \| d \| nS \rangle \right|^2}{\left(E_{nP_{3/2}} - E_{nS} \right)^2} \right] \sim \mathcal{R}. \tag{70}$$

Test extrapolations among the accurately considered cases in [50] produce errors similar to those for the scalar extrapolations. With a high accuracy calculation of $\langle 7P_{3/2} \| \mathcal{T}^2 \| 7P_{3/2} \rangle_{\mathrm{Th}}$ from [39] and the experimentally measured hyperfine B coefficient for the $7P_{3/2}$ orbital of ^{211}Fr [56], one arrives at $\mathcal{R}_{\mathrm{Th}} \sim$ -0.016 $\times 10^{-10}\,\mathrm{Hz/(V/m)}^2/\mathrm{eb}$.

With estimates of $\mathcal{M}_{\mathrm{Th}}$ and $\mathcal{R}_{\mathrm{Th}}$, one may calculate the scalar shift and electric quadrupole tensor shift of the nuclear clock transition. Specifically, we choose the $|7S_{1/2}, F = 3, m_F = \pm 3; g\rangle \leftrightarrow |7S_{1/2}, F = 2, m_F = \pm 2; m\rangle$ transitions for future convenience. The tensor shift is also largest for these stretched states.

Taking the measured nuclear ground dipole moment $\mu_g = 0.46(4)\,\mu_N$ [38] and the estimated nuclear isomer dipole moment $\mu_m = -0.076\,\mu_N$ [9], the scalar response for the

nuclear clock transition is estimated as

$$-\tfrac{1}{2}\left(\alpha_m^{(3)S} - \alpha_g^{(3)S}\right) \sim -\tfrac{1}{2}\,\mathcal{M}_{\mathrm{Th}}\left(\mu_m - \mu_g\right)$$

$$\sim 0.05 \times 10^{-10}\,\mathrm{Hz/(V/m)^2}\,.$$

Using the nuclear ground quadrupole moment $Q_g = 3.11(16)$ eb from this work and the estimated nuclear isomer quadrupole moment $Q_m = 1.8$ eb [58], the electric quadrupole tensor response for the nuclear clock transition is estimated as

$$-\tfrac{1}{2}\left(\alpha_{Qm}^{(3)T} - \alpha_{Qg}^{(3)T}\right) \sim -\tfrac{1}{2}\,\mathcal{R}_{\mathrm{Th}}\left(Q_m - Q_g\right)$$

$$\sim -0.01 \times 10^{-10}\,\mathrm{Hz/(V/m)^2}\,.$$

The quadrupole tensor shift is about five times smaller in magnitude than the scalar shift and is opposite in sign. For order-of-magnitude Stark shift comparison of the nuclear clock to current leading clocks, the tensor component will be omitted.

With an estimate of the traditional hyperfine Stark response, the "isomer Stark shift" may easily be included. We recall the general expression for third-order perturbation theory,

$$E_n^{(3)} = \sum_{k \neq n}\sum_{m \neq n} \frac{\langle n^{(0)}|V|m^{(0)}\rangle\langle m^{(0)}|V|k^{(0)}\rangle\langle k^{(0)}|V|n^{(0)}\rangle}{\left(E_m^{(0)} - E_n^{(0)}\right)\left(E_k^{(0)} - E_n^{(0)}\right)} - \langle n^{(0)}|V|n^{(0)}\rangle\sum_{m \neq n}\frac{\left|\langle n^{(0)}|V|m^{(0)}\rangle\right|^2}{\left(E_m^{(0)} - E_n^{(0)}\right)^2} \quad (71)$$

where $V = H_{hyp} + H_{iso} - \vec{d}\cdot\vec{\mathcal{E}}$ and H_{iso} is the nuclear field shift Hamiltonian. Recongnizing that the second term in Equation (71) contains the dominant contribution to the third-order shift, one can see that by taking the ratio

$$\frac{\langle 7S_{1/2}, F = 2; m|H_{iso}|7S_{1/2}, F = 2; m\rangle - \langle 7S_{1/2}, F = 3; g|H_{iso}|7S_{1/2}, F = 3; g\rangle}{\langle 7S_{1/2}, F = 2; m|H_{hyp}|7S_{1/2}, F = 2; m\rangle - \langle 7S_{1/2}, F = 3; g|H_{hyp}|7S_{1/2}, F = 3; g\rangle},$$

an estimate for the size of the isomer Stark response relative to the hyperfine Stark response may be obtained. The differential isomer field shift of the $7S_{1/2}$ orbitals is estimated from [39] and the differential hyperfine shift is estimated using the Dirac-Fock calculation of the hyperfine A coefficient. Numerically, the ratio is $\dfrac{\sim 10\,\mathrm{GHz}}{\sim 15\,\mathrm{GHz}} \lesssim 1$. From

this, one may conservatively double the hyperfine Stark response to obtain an estimate of the total third-order Stark response. One may again double the total response to account for the various estimation uncertainties. This results in a total third-order Stark response of $\sim 0.2 \times 10^{-10}$ Hz/(V/m)^2. It should be noted that not even the sign of the differential isomer field shift is known with certainty. The sign is chosen here to maximize the total third-order Stark shift in order to estimate its upper-bound.

For comparison to leading ion clocks, a useful figure of merit is the blackbody radiation shift. The blackbody radiation spectrum at 300 K is dominated by frequencies sufficiently low that a dc approximation may be made for the alkalies and certainly for Th^{3+}. Blackbody radiation is then equivalent to applying an 830 V/m electric field [59]. This leads to a shift of only 14 μHz for the nuclear clock transition. Assuming a 7.6 eV (1.84 PHz) isomer transition energy, this corresponds to a fractional blackbody shift of 8×10^{-21}. This may be compared with that of the ^{27}Al$^+$ clock where the blackbody shift is -9×10^{-18} [47], the smallest blackbody shift of clocks currently in operation (neglecting the cryogenically cooled ^{199}Hg$^+$ clock system) [60]. Analysis of a recent error budget of a ^{27}Al$^+$ clock [47] indicates that blackbody radiation introduces an error of 3 parts in 10^{18} while the clock laser and collisions contribute 0.2 and 0.5 parts in 10^{18}, respectively. For similar experimental conditions, it is reasonable to assume that trapping fields, collisions, and light shifts due to the clock laser would have negligible impact on the ^{229}Th^{3+} nuclear clock transition, particularly when compared to excess micromotion time dilation shifts and statistical uncertainty. This characteristic of the ^{229}Th^{3+} clock would remove significant experimental overhead involving any type of electric field shift reduction/calibration.

5.2.3 Zeeman Shifts

The final dominant source of systematic errors in current single ion clocks is due to the Zeeman effect. Conventionally, states which are insensitive to magnetic fields in first order

perturbation theory are chosen for clock operation. These correspond to the magnetic quantum number $m_F = 0$. Shifts arising from the clock's operating magnetic field (~ 0.1 mT) are of order 10^{-15}. When striving for 10^{-18} clock inaccuracy, strict field calibration requirements are then imposed. This is particularly challenging because the shift is quadratic in the magnetic field, similar to the time dilation shift, which limits knowledge of the absolute error to several parts in 10^{18} for the best clocks [46]. This can be seen from the expression $\langle B^2 \rangle = \langle B_{dc} \rangle^2 + \langle B_{ac}^2 \rangle$. Averaging provides precise knowledge of the mean magnetic field, but field fluctuations which are averaged out and not observed using the linear Zeeman shift, also contribute to the quadratic shift.

With introduction of the virtual clock state [49], second-order Zeeman errors are suppressed to $< 10^{-18}$ in the ^{27}Al$^+$ clock, though they are still present and require careful calibration. A virtual clock state is made by alternately interrogating transitions between extended Zeeman sub-levels where $m_F = \pm F$. In this case, the linear Zeeman shift of the stretched states allows for averaging over magnetic field fluctuations as well as precise calibration of the field magnitude. This calibration is reflected in reduced quadratic Zeeman error while the symmetry of the linear Zeeman shifts completely eliminates linear Zeeman shift errors.

In the ^{229}Th^{3+} clock, a virtual clock state may be composed of the $|7S_{1/2}, F = 3, m_F = \pm 3; g\rangle \leftrightarrow |7S_{1/2}, F = 2, m_F = \pm 2; m\rangle$ transitions. The properties of these transitions offer distinct advantages over those in the ^{27}Al$^+$ clocks. The linear splitting response of the stretched transitions is about 10 times smaller that in Al$^+$ and the quadratic Zeeman shift vanishes, completely removing all systematic Zeeman shift errors .

The linear and quadratic Zeeman shifts within a monovalent $nS_{1/2}$ orbital ($J = 1/2$) are described by the Breit-Rabi formula [31]. For the particular case when $m_F = \pm(I + 1/2)$,

$$\Delta E_Z = \pm \left(\tfrac{1}{2} g_J \mu_B + I g_I \mu_N \right) \mathcal{B} \tag{72}$$

where g_J and g_I are the Landé and nuclear g-factors, respectively, μ_B and μ_N are the Bohr and nuclear magnetons, respectively, I is the nuclear spin, and $\mathcal{B}$ is the external magnetic

field. Of importance here is the lack of a term quadratic in $\mathcal{B}$ and the fact that g_J is the same for both nuclear ground and isomer levels. To understand the linearity of these energy shifts with $\mathcal{B}$, it is helpful to consider that the interaction Hamiltonian

$$H_{int} = -\vec{\mu} \cdot \vec{\mathcal{B}} = -\left(\vec{\mu}_J + \vec{\mu}_I\right) \cdot \vec{\mathcal{B}} \tag{73}$$

is diagonal in the uncoupled basis, $|J, m_J; I, m_I\rangle$, but not diagonal in the coupled basis, $|F, m_F\rangle$. However, the maximally extended states $|F = I + J, m_F = \pm F\rangle = |J, \pm J; I, \pm I\rangle$ are eigenstates in both bases and the energies can be read immediately. There are no off-diagonal terms when solving for the eigenvalues of the sub-matrices in the coupled basis, hence, no terms arise in the secular equation which would produce non-linear shifts. The Landé g-factor only depends upon the electronic make-up to a very good approximation [61]. For the $|7S_{1/2}, F = 3, m_F = \pm 3; g\rangle \leftrightarrow |7S_{1/2}, F = 2, m_F = \pm 2; m\rangle$ transitions, the response for each stretched transition is

$$\pm \left(\mu_m - \mu_g\right) \approx \mp 4.1 \text{ kHz/mT}$$

where the nuclear magnetic dipole moment $\mu = I g_I \mu_N$ [54] and the nuclear magneton $\mu_N = 7.62$ kHz/mT. This corresponds to a total transition splitting response of 8.2 kHz/mT. This may be compared to the virtual clock state splitting in $^{27}\text{Al}^+$ of 80 kHz/mT. With 10 times less linear Zeeman response to field fluctuations, field stability requirements to suppress transition broadening are significantly relaxed. In conclusion, utilization of the maximally stretched states to compose a virtual clock transition trades in all magnetic field uncertainties for a simple $\sqrt{2}$ inflation of the Allan deviation, a highly valuable exchange.

5.2.4 Statistical Uncertainty Limits

The excited state lifetime of the $|7S_{1/2}\rangle$ clock levels is calculated to be 0.59 s [30]. Because both states predominantly decay to their respective $6D$ orbitals, a maximum clock interrogation time may be estimated as 590 ms / 2 $\approx$ 300 ms. Laser stability which allows for such long interrogation times of such narrow features has only recently been achieved. In the

^{27}Al$^+$ clock, 300 ms continuous wave interrogation pulses were used to observe a Fourier limited full-width at half-maximum signal of 2.7 Hz [62]. The natural width of that clock transition is 8 mHz.

After laser interrogation of the ^{229}Th^{3+} clock transition, the $|7S_{1/2}\rangle$, $|7P_{1/2}\rangle$, $|6D_{3/2}\rangle$ Λ-systems may be used for rapid state detection due to the $\sim$ 1 ns lifetime of the $|7P_{1/2}\rangle$ levels [30]. Hyperfine splitting and the isomer shifts of one set of electronic transitions with respect to the other should allow for unambiguous nuclear state detection. It should be noted that because all electron bridge and nuclear magnetic dipole decay channels from the isomer manifold to the ground manifold are likely to be much slower than the electric quadrupole decay from the $|7S_{1/2}\rangle$ levels [10], nuclear de-excitation might also be used in clock interrogation, avoiding additional overhead of returning the nucleus to the ground state before re-interrogating.

When dealing with frequency standards, one usually expresses the statistical measurement error with the Allan deviation. For a single ion system where all instrument fluctuations are presumed negligible and state detection and re-cooling occur much faster than clock interrogation, quantum projection noise and either clock state lifetimes or laser stability limit the statistical uncertainty. In this case, the Allan deviation is expressed as [63]

$$\sigma_y(\tau) \approx \frac{1}{2\pi\nu_0} \sqrt{\frac{1}{\tau_{probe}\,\tau}} \tag{74}$$

where ν_0 is the clock transition frequency, τ_{probe} is the clock interrogation time, and τ is the total integration time. For ν_0 = 1.84 PHz and τ_{probe} = 300 ms, one is lead to a quantum fluctuation limited Allan deviation of $\sigma_y(\tau) \approx 1.6 \times 10^{-16}\,\tau^{-1/2}$. In measuring two stretched transitions which compose the virtual clock transition, statistical uncertainty may be reduced to $\approx 5 \times 10^{-19}$ in 2 days of continuous integration. For minimal excess micromotion, e.g. ±1 V/m stray electric field at the ion, this level of statistical error clearly dominates all Stark and time dilation shifts. In fact, about 60 days of integration would be required to obtain a statistical uncertainty of 1×10^{-19}. It is interesting to note that a vertical displacement of the clock ion by 0.9 mm would induce a time dilation shift of 1×10^{-19} via

the gravitational potential shift.

With future reduction in laser instability providing access to longer clock interrogation times, electronic ground states may possibly be used in $^{229}\text{Th}^{4+}$ for clock operation via quantum logic spectroscopy. This would reduce the clock transition width to that of the nuclear M1 natural width, $\lesssim 1$ mHz. The completely closed and spherical electronic shell would further suppress electric and magnetic field shifts and errors by removing H_{hyp} and quadratic Zeeman shifts for all states. Additionally, all excited electronic levels would lie $\gtrsim 20$ eV above the ground level [64–66], further suppressing Stark shifts due to the large energy separations.

Though laser instability and quantum projection noise serve to some degree as equalizers among single-ion clocks having systematic inaccuracies of $\lesssim 10^{-17}$, the nuclear clock brings additional value by reducing experimental overhead in achieving sufficiently small systematic errors. With sub-MHz electric dipole transitions from the electronic ground levels, ground state cooling is easily accessible for time dilation minimization. The estimate here predicting an extremely small differential polarizability of the clock states may effectively eliminate blackbody, collisional, laser, and trapping field Stark shifts. Because both clock levels are S orbitals, no quadrupole shift exists, eliminating the need for clock interrogation along three orthogonal directions . Finally, implementation of a virtual clock transition with zero quadratic Zeeman response removes the requirement of precise calibration of the operational dc magnetic field and pollutant ac fields, e.g. from trap electrode currents, ac line currents, etc. The extremely low linear Zeeman response also reduces the stability requirements of an external operating magnetic field.

5.3   *Nuclear Transition Sensitivity to α-Variation*

A potentially immense contribution that a ^{229}Th nuclear clock may provide to fundamental physics research is in the search for temporal variation of fundamental constants, particularly the fine structure constant α. The fine structure constant characterizes the electromagnetic interaction strength. A laboratory search for α-variation is done by measuring the ratio of atomic clock frequencies derived from different atomic systems over a long period of time. Because the two different systems would have different sensitivities to α-variation, the two clock frequencies would differentially shift, changing the frequency ratio. The key to a sensitive probe is precise frequency measurement of the clock transitions and largely different sensitivities of the transitions to α-variation.

The dependence of an electron energy level on α arises only within a relativistic theory. For a monovalent electron of a multielectron atom, the relativistic correction to energy is approximately equal to $E_n \dfrac{(Z\alpha)^2}{n_{eff}\,(J + 1/2)}$ where E_n is the non-relativistic orbital energy, Z is the nuclear charge, J is the total electronic angular momentum, and n_{eff} is the effective principal quantum number [67].

The relation between clock frequency shift and α-variation may be expressed in general as

$$\delta \nu = s \frac{\delta \alpha}{\alpha}, \tag{75}$$

where s is the sensitivity factor. The best determination of temporal variation of α to date was done in [46] where the ratio of the ^{27}Al$^+$ and ^{199}Hg$^+$ single ion clock frequencies was measured over the course of a year. With sensitivity factors $s_{Hg+} = -3.1 \times 10^{15}$ Hz [67] and $s_{Al+} = 8.8 \times 10^{12}$ Hz [68], the fractional temporal variation of the fine structure constant was measured to be $\dot{\alpha}/\alpha = (-1.6 \pm 2.3) \times 10^{-17}$/year.

The system of the ^{229}Th nuclear clock is fundamentally different from atomic clock systems. The coincidentally small nuclear transition splitting is due to near cancellation of MeV scale nuclear interactions involving not only the electromagnetic repulsion of the protons, but also the strong interaction among all the nucleons (protons and neutrons) [12].

The change in Coulomb energy from the ground to isomer state dictates the transition sensitivity to α-variation. In this case, the sensitivity factor may be expressed as [69]

$$s_{Th3+} = \frac{\Delta V_C}{h} \tag{76}$$

where ΔV_C is the change in Coulomb energy and h is Planck's constant. The two nuclear states differ primarily in the orbit occupied by the last unpaired neutron. This orbital change alters, via the strong interaction, the polarization of the proton distribution and therefore alters the Coulomb energy [70]. For large nuclei, e.g. ^{229}Th, V_C is of the order 10^9 eV $\sim h \times 10^{23}$ Hz. This energy is 8 orders of magnitude larger than $h \, s_{Hg+}$ and it is clear that even for a very small fractional change in Coulomb energy, a significant enhancement in α-sensitivity may be produced in the nuclear system.

Nuclear models predict widely varying values for ΔV_C within the range $\pm$ several hundred keV for the ground and isomer states of the ^{229}Th nucleus [70]. Hence, the sensitivity in not currently known but is not likely to be small compared to atomic transitions. Fortunately, precision spectroscopy of the electronic structure within the isomer manifold should provide a reliable empirical determination of ΔV_C with little or no dependence on the nuclear model assumed. This may be done by measuring the change in the nuclear electric quadrupole moment and nuclear mean-square radius of the isomer state with respect to the ground state [39]. The isomer manifold hyperfine structure allows access to Q_m while the isomeric field shift (analogous to the isotope field shift), which may be directly measured, provides determination of $\delta \langle r^2 \rangle$.

For concreteness, suppose $\Delta V_C = 100$ keV. This implies that $s_{Th3+} \approx 2 \times 10^{19}$ Hz. If the clock transitions in ^{229}Th^{3+} and ^{27}Al$^+$, for example, are measured at the level of 1×10^{-18} inaccuracy over the course of one year, a temporal variation of α may be detected with a sensitivity of $\dot{\alpha}/\alpha \approx \pm 1 \times 10^{-22}$/year. This result would represent an improvement in sensitivity by more than 5 orders of magnitude over the best current measurement and could be done with no significant advances in atomic clock technology.

CHAPTER VI

CONCLUSION AND OUTLOOK

In this work, laser cooling of a multiply charged ion was achieved for the first time. Particularly, ^{232}Th^{3+} was laser cooled to crystallization. The required techniques developed here, i.e. creation, confinement, long storage times, and laser cooling, were then extended to ^{229}Th^{3+} where creation, trapping, precision spectroscopy, and laser cooling were all achieved for the first time. This result paves the way toward efficient optical excitation of the nuclear isomer.

With appropriate commercial ultra-fast lasers to span the current energy uncertainty of the nuclear transition, a linear chain of ultra-cold ^{229}Th^{3+} ions is a nearly ideal system for initial nuclear excitation. The highly localized ions may be placed at the center of a tightly focused excitation laser beam for an efficient spectral search. The total ion illumination time is expected to be tens of hours.

Once the isomer level is found, a single ion within a linear crystallized chain can been excited to the isomer manifold and its hyperfine structure and isomeric level shifts may be accurately measured. This knowledge would allow both for unambiguous identification of the isomer level and for an empirical determination of the isomer transition sensitivity to α -variation.

Finally, with a single trapped ^{229}Th^{3+} ion cooled to its ground state, estimates here suggest that a nuclear optical clock of unparalleled stability may be implemented. In addition, it is likely that a clock based on the nuclear isomer transition would be tremendously sensitive to α-variation, with a sensitivity enhancement factor possibly reaching a factor of 10^6 over traditional atomic clock transitions.

REFERENCES

[1] L. A. Kroger and C. W. Reich, "Features of low-energy level scheme of Th-229 as observed in alpha-decay of U-233," *Nuclear Physics A* **259**, 29 (1976).

[2] C. W. Reich and R. G. Helmer, "Energy Separation of the Doublet of Instrinsic States at the Ground State of ^{229}Th," *Physical Review Letters* **64**, 271 (1990).

[3] R. G. Helmer and C. W. Reich, "An excited state of ^{229}Th at 3.5 eV," *Physical Review C* **49**, 1845 (1994).

[4] G. M. Irwin and K. H. Kim, "Observation of Electromagnetic Radiation from Deexcitation of the ^{229}Th Isomer," *Physical Review Letters* **79**, 990 (1997).

[5] D. S. Richardson, D. M. Benton, D. E. Evans, J. A. R. Griffith, and G. Tungate, "Ultraviolet Photon Emission Observed in the Search for the Decay of the ^{229}Th Isomer," *Physical Review Letters* **80**, 3206 (1998).

[6] S. B. Utter, P. Beiersdorfer, A. Barnes, R. W. Lougheed, J. R. Crespo Lopex-Urrutia, J. A. Becker, and M. S. Weiss, "Reexamination of the Optical Gamma Ray Decay in ^{229}Th," *Physical Review Letters* **82**, 505 (1999).

[7] R. W. Shaw, J. P. Young, S. P. Cooper, and O. F. Webb, "Spontaneous Ultraviolet Emission from ^{233}Uranium/^{229}Thorium Samples," *Physical Review Letters* **82**, 1109 (1999).

[8] B. R. Beck, J. A. Becker, P. Beiersdorfer, G. V. Brown, K. J. Moody, J. B. Wilhelmy, F. S. Porter, C. A. Kilbourne, and R. L. Kelley, "Energy Splitting of the Ground-State Doublet in the Nucleus ^{229}Th," *Physical Review Letters* **98**, 142501 (2007).

[9] A. M. Dykhne and E. V. Tkalya, "Matrix element of the anomalously low-energy (3.5 ± 0.5 eV) transition in Th-229 and the isomer lifetime," *JETP Letters* **67**, 251 (1998).

[10] S. G. Porsev and V. V. Flambaum, "Effect of atomic electrons on the 7.6-eV nuclear transition in ^{229}Th^{3+}," *Physical Review A* **81**, 032504 (2010).

[11] E. Peik and C. Tamm, "Nuclear laser spectroscopy of the 3.5 eV transition in Th-229," *Europhysics Letters* **61**, 181 (2003).

[12] V. V. Flambaum, "Enhanced Effect of Temporal Variation of the Fine Structure Constant and the Strong Interaction in ^{229}Th," *Physical Review Letters* **97**, 092502 (2006).

[13] D. J. Griffiths, *Introduction to electrodynamics*, 3rd ed. (Prentice Hall, Upper Saddle River, N.J., 1999).

[14] H. Dehmelt, *Advances in Atomic and Molecular Physics, Vol. 3* (Academic Press, New York, New York 1975).

[15] H. Dehmelt, *Advances in Atomic and Molecular Physics, Vol. 5* (Academic Press, New York, New York 1975).

[16] W. Paul and H. Steinwedel, "Ein Neues Massenspektrometer Ohne Magnetfeld," *Zeitschrift Fur Naturforschung Section A* **8**, 448 (1953).

[17] D. J. Berkeland, J. D. Miller, J. C. Bergquist, W. M. Itano, and D. J. Wineland, "Minimization of ion micromotion in a Paul trap," *Journal of Applied Physics* **83**, 5025 (1998).

[18] P. K. Ghosh, *Ion traps* The International series of monographs on physics (Clarendon Press, Oxford University Press, Oxford New York, 1995).

[19] J. Colgan, D. M. Mitnik, and M. S. Pindzola "Electron-impact ionization of multiply charged manganese ions," *Physical Review A* **6301**, 012712 (2001).

[20] L. R. Churchill, *Trapping Triply Ionized Thorium Isotopes*, Ph.D thesis, Georgia Institute of Technology 2008.

[21] F. Caridi, L. Torrisi, D. Margarone, A. Picciotto, A. M. Mezzasalma, and S. Gammino "Energy distributions of particles ejected from laser-generated pulsed plasmas," *Czechoslovak Journal of Physics* **56**, B449 (2006).

[22] P. F. A. Klinkenberg, "Spectral Structure of Trebly Ionized Thorium, Th-IV," *Physica B & C* **151**, 552 (1988).

[23] J. C. Schwartz, M. W. Senko, and J. E. P. Syka, "A two-dimensional quadrupole ion trap mass spectrometer," *Journal of the American Society for Mass Spectrometry* **13**, 659 (2002).

[24] L. R. Churchill, M. V. DePalatis, and M. S. Chapman, "Charge exchange and chemical reactions with trapped Th^{3+}," *Physical Review A* **83**, 012710 (2011).

[25] H. J. Metcalf and P. van der Straten, *Laser Cooling and Trapping* (Springer-Verlag New York, 1999).

[26] J. D. Jackson, *Classical Electrodynamics* Third Edition (John Wiley & Sons New York, 1999).

[27] W. M. Itano and D. J. Wineland, "Laser cooling of ions stored in harmonic and Penning traps," *Physical Review A* **25**, 35 (1982).

[28] L. Hornekaer and M. Drewsen, "Formation process of large ion Coulomb crystals in linear Paul traps," *Physical Review A* **66**, 013412 (2002).

[29] D. H. E. Dubin and T. M. O'Neil, "Computer Simulations of Ion Clouds in a Penning Trap," *Physical Review Letters* **60**, 511 (1988).

[30] U. I. Safronova, W. R. Johnson, and M. S. Safronova, "Excitation energies, polarizabilities, multipole transition rates, and lifetimes in ThIV," *Physical Review A* **74**, 042511 (2006).

[31] D. A. Steck, *Quantum and Atom Optics*, Revision 0.5.10 (available online at `http://steck.us/teaching`, 2011).

[32] D. J. Berkeland and M. G. Boshier, "Destabilization of dark states and optical spectroscopy in Zeeman-degenerate atomic systems," *Physical Review A* **65**, 033413 (2002).

[33] A. E. Siegman, *Lasers* (University Science Books, Sausalito, California 1986).

[34] K. G. Libbrecht and J. L. Hall, "A low-noise high-speed diode-laser current controller," *Review of Scientific Instruments* **64**, 2133 (1993).

[35] A. V. Steele, *Barium Ion Cavity QED and Triply Ionized Thorium Ion Trapping*, Ph.D thesis, Georgia Institute of Technology 2008.

[36] J. R. Taylor, *An Introduction to Error Analysis* (University Science Books, Sausalito, California 1997).

[37] C. Schwartz, "Theory of Hyperfine Structure," *Physical Review* **97**, 380 (1955).

[38] S. Gerstenkorn, P. Luc, J. Verges, D. W. Englekemeir, J. E. Gindler, and F. S. Tomkins, "Structures yperfines du spectre d'etincelle, moment magnetique et quadrupolaire de l'isotope 229 du thorium," *Journal de Physique* **35**, 483 (1974).

[39] J. C. Berengut, V. A. Dzuba, V. V. Flambaum, and S. G. Porsev, "Proposed Experimental Method to Determine α Sensitivity of Splitting between Ground and 7.6 eV Isomeric States in ^{229}Th," *Physical Review Letters* **102**, 210801 (2009).

[40] M. S. Safronova, "Private Communication," 2009.

[41] V. A. Dzuba, W. R. Johnson, and M. S. Safronova, "Calculation of isotope shifts for cesium and francium," *Physical Review A* **72**, 022503 (2005).

[42] I. Angeli, "A consistent set of nuclear rms charge radii: properties of the radius surface R(N,Z)," *Atomic Data and Nuclear Data Tables* **87**, 185 (2004).

[43] J. C. Berengut, "Personal Communication," 2011.

[44] C. E. Bemis, Jr., F. K. McGowan, J. L. C. Ford, Jr., W. T. Milner, R. L. Robinson, P. H. Stelson, G. A. Leander, and C. W. Reich, "Coulomb Excitation of States in ^{229}Th," *Physica Scripta* **38**, 657 (1988).

[45] C. J. Campbell, A. V. Steele, L. R. Churchill, M. V. DePalatis, D. E. Naylor, D. N. Matsukevich, A. Kuzmich, and M. S. Chapman, "Multiply Charged Thorium Crystals for Nuclear Laser Spectroscopy," *Physical Review Letters* **102**, 233004 (2009).

[46] T. Rosenband, D. B. Hume, P. O. Schmidt, C. W. Chou, A. Brusch, L. Lorini, W. H. Oskay, R. E. Drullinger, T. M. Fortier, J. E. Stalnaker, S. A. Diddams, W. C. Swann, N. R. Newbury, W. M. Itano, D. J. Wineland, and J. C. Bergquist, "Frequency ratio of Al$^+$ and Hg$^+$ single-ion optical clocks; Metrology at the 17th decimal place," *Science* **319**, 1808 (2008).

[47] C. W. Chou, D. B. Hume, J. C. J. Koelemeij, D. J. Wineland, and T. Rosenband, "Frequency Comparison of Two High-Accuracty Al$^+$ Optical Clocks," *Physical Review Letters* **104**, 070802 (2010).

[48] D. J. Wineland, W. M. Itano, J. C. Bergquist, and R. G. Hulet, "Laser-cooling limits and single-ion spectroscopy," *Physical Review A* **36**, 2220 (1987).

[49] T. Rosenband, P. O. Schmidt, D. B. Hume, W. M. Itano, T. M. Fortier, J. E. Stalnaker, K. Kim, S. A. Diddams, J. C. J. Koelemeij, J. C. Bergquist, and D. J. Wineland, "Observation of the $^1S_0 \rightarrow {}^3P_0$ Clock Transition in ^{27}Al$^+$," *Physical Review Letters* **98**, 220801 (2007).

[50] V. A. Dzuba, V. V. Flambaum, K. Beloy, and A. Derevianko, "Hyperfine-mediated static polarizabilities of monovalent atoms and ions," *Physical Review A* **82**, 062513 (2010).

[51] A. Hofer, P. Moroshkin, S. Ulzega, and A. Weis, "Calculation of the forbidden electric tensor polarizabilities of free Cs atoms and of Cs atoms trapped in a solid ^{4}He matrix," *Physical Review A* **77**, 012502 (2008).

[52] K. Beloy, U. I. Safronova, and A. Derevianko, "High-Accuracy Calculation of the Blackbody Radiation Shift in the ^{133}Cs Primary Frequency Standard," *Physical Review Letters* **97**, 040801 (2008).

[53] M. S. Safronova, D. Jiang, and U. I. Safronova, "Blackbody radiation shift in the ^{87}Rb frequency standard," *Physical Review A* **82**, 022510 (2010).

[54] W. R. Johnson, *Atomic Structure Theory, Lectures on Atomic Physics* (Springer-Verlag Berlin Heidelberg 2007).

[55] V. A. Dzuba, V. V. Flambaum, and O. P. Sushkov, "Relativistic many-body calculations of the hyperfine-structure intervals in caesium and francium atoms," *Journal of Physics B: Atomic and Molecular Physics* **17**, 1953 (1984).

[56] S. Liberman, J. Pinard, H. T. Duong, P. Juncar, P. Pillet, J. -L. Vialle, P. Jacquinot, F. Touchard, S. Buttgenbach, C. Thibault, M. de Saint-Simon, R. Klapisch, A. Pesnelle, and G. Huber, "Laser optical spectroscopy of francium D$_2$ resonance line," *Physical Review A* **22**, 2732 (1980).

[57] U. I. Safronova, W. R. Johnson, and M. S. Safronova, "Excitation energies, polarizabilities, multipole transition rates, and lifetimes of ions along the francium isoelectronic sequence," *Physical Review A* **76**, 042504 (2007).

[58] E. V. Tkalya, "Proposal for a Nuclear Gamma-Ray Laser of Optical Range," *Physical Review Letters* **106**, 162501 (2011).

[59] W. M. Itano, L. L. Lewis, and D. J. Wineland, "Shift of $^2S_{1/2}$ hyperfine splittings due to blackbody radiation," *Physical Review A* **25**, 1233 (1982).

[60] T. Rosenband, W. M. Itano, P. O. Schmidt, D. B. Hume, J. C. J. Koelemeij, J. C. Bergquist, and D. J. Wineland, "Backbody radiation shift of the ^{27}Al$^+$ $^1S_0 \rightarrow {}^3P_0$ transition," *arXiv:physics/0611125v2* (2006).

[61] E. Arimondo, M. Inguscio, and P. Violino, "Experimental determinations of the hyperfine structure in the alkali atoms," *Review of Modern Physics* **49**, 31 (1977).

[62] C. W. Chou, D. B. Hume, T. Roseband, and D. J. Wineland, "Optical Clocks and Relativity," *Science* **329**, 1630 (2010).

[63] R. J. Rafac, B. C. Young, J. A. Beall, W. M. Itano, D. J. Wineland, and J. C. Bergquist, "Sub-dekahertz Ultraviolet Spectroscopy of ^{199}Hg$^+$," *Physical Review Letters* **85**, 2462 (2000).

[64] A. Redfors and J. Reader, "Spectrum and energy levels of the xenonlike ion Ce V," *Physical Review A* **43**, 2367 (1991).

[65] J. Sugar and V. Kaufman, "Spectra and energy levels of three- and four-times ionized hafnium (Hf IV and Hf V)," *Journal of the Optical Society of America* **64**, 1656 (1974).

[66] J. Sugar and C. Corliss, "Atomic Energy Levels of the Iron-Period Elements: Potassium through Nickel," *Journal of Physical and Chemical Reference Data* **14**, 1 (1985).

[67] V. A. Dzuba, V. V. Flambaum, and J. K. Webb, "Calculations of the relativistic effects in many-electron atoms and space-time variation of fundamental constants," *Physical Review A* **59**, 230 (1999).

[68] E. J. Angstmann, V. A. Dzuba, and V. V. Flambaum, "Relativistic effects in two valence-electron atoms and ions and the search for variation of the fine-structure constant," *Physical Review A* **70**, 014102 (2004).

[69] A. C. Hayes and J. L. Friar, "Sensitivity of nuclear transition frequencies to temporal variation of the fine structure constant or the strong interaction," *Physics Letters B* **650**, 229 (2007).

[70] E. Litvinova, H. Feldmeier, J. Dobaczewski, and V. Flambaum ,"Nuclear structure of lowest ^{229}Th states and time-dependent fundamental constants," *Physical Review C* **79**, 064303 (2009).

VITA

Corey J. Campbell was born in Dayton, Ohio.